

SEARCH FOR THE RARE DECAY OF THE MUON
INTO A POSITRON AND A PHOTON

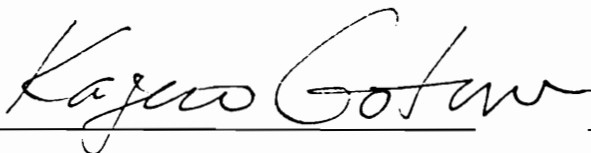
by
Yiding Zhang

Dissertation submitted to the Faculty of the
Virginia Polytechnic Institute and State University
in partial fulfillment of the requirements for the degree of
DOCTOR OF PHILOSOPHY
in
Physics

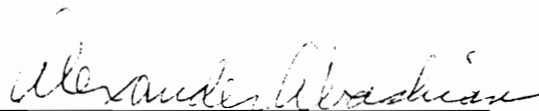
APPROVED:



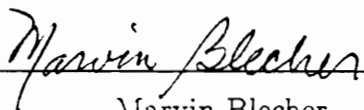
Leo Eric Piilonen, Chairman



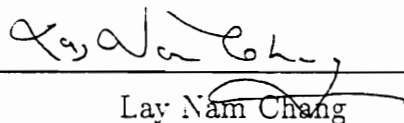
Kazuo Gotow



Alexander Abashian



Marvin Blecher



Lay Nam Chang

October, 1995
Blacksburg, Virginia

Key Words: Muon, Decay, Symmetry

C.2

LD

5655

V856

1995

Z437

C.2

SEARCH FOR THE RARE DECAY OF THE MUON INTO A POSITRON AND A PHOTON

by
Yiding Zhang

Leo E. Pilonen, Chairman

Department of Physics

(ABSTRACT)

This thesis gives a detailed description of the MEGA experiment as well as a search for the $\mu^+ \rightarrow e^+\gamma$ signal in the 1992 data. The MEGA detector is designed to search for the lepton family number nonconserving decay mode, $\mu^+ \rightarrow e^+\gamma$, with a branching ratio sensitivity of $\mathcal{O}(10^{-13})$.

A two-component detector is located in a 1.5 T solenoidal magnetic field. The positron spectrometer, one component of the MEGA detector, is composed of a set of cylindrical MWPCs and plastic scintillators. It occupies the central space of the magnet to detect positrons. The second component of the MEGA detector is composed of three identical coaxial photon pair spectrometers outside the positron spectrometer. The photon is converted into an e^+e^- pair in one of the pair spectrometers and the photon energy and incident angle are extracted by detection of this pair.

After a discussion of the experimental motivation, the design, construction, and performance of both spectrometers is described. The detector response, extracted from the calibration data collected during the 1992 run, is presented along with a comparison of Monte Carlo simulated results. A null result is obtained from the search for the decay of $\mu \rightarrow e\gamma$ in the 1992 MEGA data, resulting in a branching ratio upper limit of 1.01×10^{-3} (90 % C.L.). This result was obtained from a low-statistics, engineering run with an incomplete detector system, but the 1992 data analysis structure and valuable experience for future searches with this apparatus was established.

DEDICATION

This dissertation is dedicated to my wife, Ping He.

ACKNOWLEDGMENTS

After over four years of hard work, this thesis is finally done. I would like to express my gratitude to my thesis advisor, Dr. Leo E. Piilonen, for his guidance and support during these years. I greatly appreciate his advice, attention and patience. I also wish to thank Mrs. Piilonen who taught me a lot of English and a great deal about American culture.

I would like to thank Dr. Martin D. Cooper, spokesman of the MEGA experiment, and Dr. Richard E. Mischke. They gave me their strong support, and very useful suggestions in the whole process of data taking to data analysis. I also sincerely thank Dr. Gary Hogan for his wonderful reconstruction code (ERC), Dr. Michael A. Kroupa, Dr. Melynda Brooks and Dr. David Whitehouse for their constant help and support.

I would also like to express my debt to all other members of the MEGA collaboration for their dedication and expertise. Specifically, I thank Carl Gagliardi, Shirvel Stanislaus, Robert Manweiler, Xiao-lin Tu, Yikuang Chen and Dan Haim. They provided very valuable suggestions, important analyses and supplied many useful contributions for this dissertation.

I owe many thanks to my fellow graduate students—Dr. Charles J. Jui, Dr. Leo Van Ausdeln, Dr. Mario Dzemidzic, Dr. Fan Liu, Keith Stantz, Dr. Chopin Soo and Fei-sheng Lee—for their assistance here, and for their friendship outside of this research.

Finally, I am grateful to my mother, Xin-Bao Chan, and my wife, Ping He, whose love, encouragement and dedication accompanied me through the long and arduous path to the Ph.D.

Contents

ABSTRACT	ii
DEDICATION	iii
ACKNOWLEDGMENTS	iv
1 Introduction	1
2 Theoretical Background	6
2.1 Overview of the Standard Model	6
2.2 Extensions to the Standard Model and $\mu \rightarrow e\gamma$	11
2.2.1 Massive Neutrino Model	12
2.2.2 Left-right Symmetric Electroweak Interaction Model	14
2.2.3 Grand Unified Theories	15
2.2.4 Supersymmetric Model	16
2.3 Calculation of the Rare Decay $\mu \rightarrow e\gamma$	17
2.3.1 Operator Analysis	18
2.3.2 The Diagrams of $\mu \rightarrow e\gamma$	19
2.3.3 Calculation of Transition Matrix of $\mu \rightarrow e\gamma$	19
2.3.4 Results for the Rare Decay $\mu \rightarrow e\gamma$	25
3 Experimental Design	26
3.1 Overview	26
3.2 Background and Sensitivity	32

3.3	Beam, Target and Magnet	38
3.4	Photon Pair-Spectrometer	41
3.4.1	Converter	46
3.4.2	Photon Spectrometer Scintillators	46
3.4.3	The Photon Spectrometer MWPC	48
3.4.4	Photon Spectrometer Drift Chamber	50
3.5	The Positron Spectrometer	51
3.5.1	The Positron Spectrometer Scintillators	53
3.5.2	Positron Spectrometer MWPCs	55
3.6	Trigger and Data Acquisition Systems	58
3.6.1	MEGA Trigger System	58
3.6.2	Data Acquisition System	61
3.6.3	Online Filter	62
3.7	Analysis Programs	66
3.7.1	REPLAY	66
3.7.2	Histogramming	66
3.7.3	SED	66
3.7.4	Positron Reconstruction Program	68
3.7.5	Photon Reconstruction	72
3.8	Monte Carlo Simulation	81
4	Experimental Detector Response	84
4.1	Overview of 1992 Data Taking	84
4.1.1	Detector Performance	87
4.1.2	Data Collection	90
4.2	Positron Spectrometer Response	92
4.2.1	Channel Mapping and Detector Alignment	92
4.2.2	Spectrometer Detection Efficiency	98
4.2.3	Positron Energy Spectrum	104
4.3	Photon Spectrometer Response	109
4.3.1	Photon Energy Calibration	109

4.4	Target	115
4.4.1	Muon Decay Point Resolution	115
4.4.2	Positron Initial Direction Resolution	126
4.5	Timing	134
4.5.1	Scintillator Timing Calibration	134
4.5.2	Ring Counter Events in the MEGA data	141
4.6	Muon Inner Bremsstrahlung	148
4.6.1	Inner Bremsstrahlung Data Analysis	148
4.6.2	Inner Bremsstrahlung signal in the MEGA data	150
5	The $\mu \rightarrow e\gamma$ Search	155
5.1	Overview of Production Data Analysis	155
5.2	Cut Analysis and $\mu \rightarrow e\gamma$ Search	160
5.2.1	The Positron Energy Cut	163
5.2.2	Photon Energy Cut	165
5.2.3	$e\gamma$ Opening Angle Cut	165
5.2.4	Relative $e\gamma$ Timing Cut	167
5.2.5	$\mu \rightarrow e\gamma$ Search	170
5.3	Normalization	170
5.4	Branching Ratio	173

List of Tables

1	μ decay modes	3
2	Lepton family number assignment and conservation laws.	10
3	Proposed extensions to the Standard Model	11
4	Comparison of goals of MEGA with previous experiments.	37
5	Background and signal levels per muon decay in MEGA	38
6	Evaluation of number of useful muon stops.	39
7	Parameters of the MEGA magnet	42
8	Summary of photon arm geometrical parameters	45
9	Parameters of the photon scintillator system.	49
10	Photon arm MWPC parameters	50
11	Parameters of the photon arm drift chambers.	52
12	Geometric configuration of the positron arm	54
13	The list of triggers available in 1992 Runs.	61
14	Estimation of the <i>design</i> peak raw $\mu \rightarrow e\gamma$ data rate.	63
15	Definition of on-line ARC reconstruction fail codes	65
16	Slanted target ERC reconstruction failures for Michel tracks	74
17	Definition of on-line PAIRs reconstruction failed code	77
18	Comparison of the best vertex selection method for 52.8 MeV photon	80
19	Interactions imposed in EGS4	82
20	The positron MWPC setup	87
21	MEGA detector calibration runs	91
22	Positron MWPCs efficiencies	101
23	Energy endpoint centroid and spread of Michel-decay positrons	109

24	Photon energy resolution	113
25	μ decay point resolution for Michel positrons	123
26	μ decay point resolution from Monte Carlo simulation	123
27	η distribution	128
28	Summary of estimation of IB signal and background in MEGA data .	151
29	1992 MEGA production Run	156
30	The 1992 filter efficiencies	158
31	Energy resolutions of simulated positrons	164
32	Calculated energy resolution for real 52.8 MeV positrons	164
33	Summary of cuts for the $\mu \rightarrow e\gamma$ search	170
34	The summary of the number of useful stopped muons in 1992	173
35	Summary of the solid angle and the efficiency comparison between analysis and design	174

List of Figures

1	Rare muon decay experimental history	2
2	Constituents of the Standard Model	8
3	The Feynman diagrams for $\mu \rightarrow e\gamma$ with massive neutrinos	13
4	The T matrices of the Left-right Symmetric Model.	14
5	$\mu \rightarrow e\gamma$ via slepton mixing.	17
6	The block diagram of $\mu \rightarrow e\gamma$	18
7	The Feynman diagrams of $\mu \rightarrow e\gamma$ under R_ξ gauge.	20
8	Cut away view of MEGA detector.	28
9	End view of MEGA detector.	29
10	Side view of MEGA detector.	30
11	The kinematics of $\mu \rightarrow e\gamma$ decay at rest.	32
12	Integrated energy spectrum of photons	34
13	The comparison of the 90% confidence sensitivity as function of running time for MEGA and the Crystal Box experiment.	36
14	Stopped Muon Beam line at LAMPF	39
15	Field strength vs position.	41
16	Cross sectional view of one layer of a typical photon conversion	43
17	Plot of probability of pair-production (solid), pair <i>survival</i> probability (dotted), and net conversion efficiency (dashed) versus converter thickness, for 52.8 MeV photons	47
18	End view of positron spectrometer, looking upstream.	52
19	Cross section of a positron scintillator, looking upstream	53
20	Schematic drawing of a dwarf chamber	56

21	MEGA data acquisition system	60
22	Graphical output of Single-Event-Display	67
23	ERC Cluster.	69
24	Display of a positron track reconstructed by ERC.	73
25	Photon arm pattern recognition code structure.	75
26	PAIRS fail code distribution for MEGA run 2839	76
27	Anode and Cathode efficiency (relative) vs voltage. The operating voltage was typically set at 2150 V.	86
28	Anode efficiency (relative) vs the discriminator threshold.	86
29	The strobe time vs Anode wire efficiency (relative).	88
30	DC plateau curve	89
31	One example of the positron spectrometer MWPC channel map before and after correction of mapping errors.	93
32	The circle-fit residual distributions of Dwarf 6 anodes before (top) and after (bottom) ϕ alignment.	95
33	The parameters for MWPCs alignment.	96
34	The side-fit residual distributions of Dwarf 6 cathodes before (top) and after (bottom) Z alignment.	97
35	Electron scintillator map	99
36	Dwarf efficiency	100
37	Efficiency of each positron scintillator. Channels with large error bars were poorly illuminated by <i>reconstructed tracks</i> due to chamber ineffi- ciencies.	102
38	Efficiency of all scintillators in z	102
39	The Michel decay positron energy spectrum	103
40	The Michel decay positron momentum vs longitudinal momentum for decays from the slanted MEGA target.	105
41	Michel zero-loop energy spectrum	106
42	Michel one-loop energy spectrum	107
43	Michel high-loop energy spectrum	108
44	1993 π^0 data	110

45	Opening angle between the photons from $\pi^0 \rightarrow \gamma\gamma$ for 1993 data (top) and Monte Carlo events (bottom).	112
46	Monte Carlo for pi data	113
47	55 MeV photon energy peak for inner (top) and outer (bottom) conversion events.	114
48	The projection of the muon decay points on the x-y plane at z=0.	119
49	The z component of the reconstructed muon decay points.	120
50	The μ decay points in the target plane. $u(w)$ is along the semi-major (semi-minor) axis of the target ellipse.	121
51	The projection of the μ decay points on w axis	122
52	The μ reconstructed decay points on the target plane for simulated events.	124
53	The w projected distribution for simulated events.	125
54	The η distribution for real data (top) and Monte Carlo simulation (bottom)	129
55	The positron MWPC usage frequency in the track reconstruction for the data (top) and simulation (bottom)	130
56	The Dwarf 1 anodes hit frequency for the data (top) and simulation (bottom)	131
57	The λ distribution, before the cut on η (top) and after the cut (bottom).	132
58	The η vs λ distribution	133
59	The timing flow chart of a typical $\mu \rightarrow e\gamma$ signal	135
60	The location of the downstream Ring Counter.	136
61	RC timing flow	137
62	Photon traceback to the z -axis for a typical MEGA run.	141
63	Difference of Ring Counter time with scintillator times vs Ring Counter time	142
64	RC 2D scatterplot	144
65	Projection of RC timing	145
66	RC timing even-odd-layers	146
67	RC timing	147

68	IB timing distribution of 1994	149
69	IB events in the 1992 run	152
70	The ERC reconstruction rate vs chamber gate offset for simulated events.	154
71	Filter 3 efficiency vs run number	159
72	Four kinematic variables	161
73	The simulated 52.8 MeV positron energy spectrum	162
74	52.8 MeV Photon spectra	166
75	Positron-photon opening angle distribution	168
76	Energy box cuts for the 1992 search	169

Chapter 1

Introduction

Symmetry principles have always played a major role in modern physics, especially in nuclear and particle physics, and have served as a guide in the elaboration of theories. Among these symmetries, the Law of Conservation of Lepton Family Number is assumed to hold in every physical process, whether strong, weak or electromagnetic.

This ad hoc conservation law originally came from the studies of lepton decay modes. The muon plays a key role in these studies since the muon is the lightest decaying lepton, and muon decay provides a “*pure*” leptonic process. The normal muon decay mode, $\mu \rightarrow e\nu\bar{\nu}$, is called the Michel process. This has a typical continuous electron energy spectrum, just like a nuclear β decay spectrum, that is characteristic of a three body final state. Two other allowed decay modes of the muon are Internal Bremsstrahlung, $\mu \rightarrow e\gamma\nu\bar{\nu}$, and $\mu \rightarrow e\nu\bar{\nu}ee$. The branching fractions for these muon decay channels are listed in Table 1. As in beta decay, no neutrinoless muon decay modes—such as $\mu \rightarrow e\gamma$, $\mu \rightarrow e\gamma\gamma$ or $\mu \rightarrow eee$ —have ever been observed. This implies that not only lepton number, but also lepton family number, has to be conserved. This symmetry has been used as a basis to construct the “Standard Model,” one of the most successful theories of this century.

The law of lepton family number conservation is based upon experimental measurements. With the availability of more sources of muons and improved experimental techniques, the branching ratio sensitivity to neutrinoless decay modes has been pushed to new limits. Fig. 1 shows the history of the search for muon rare decays. A

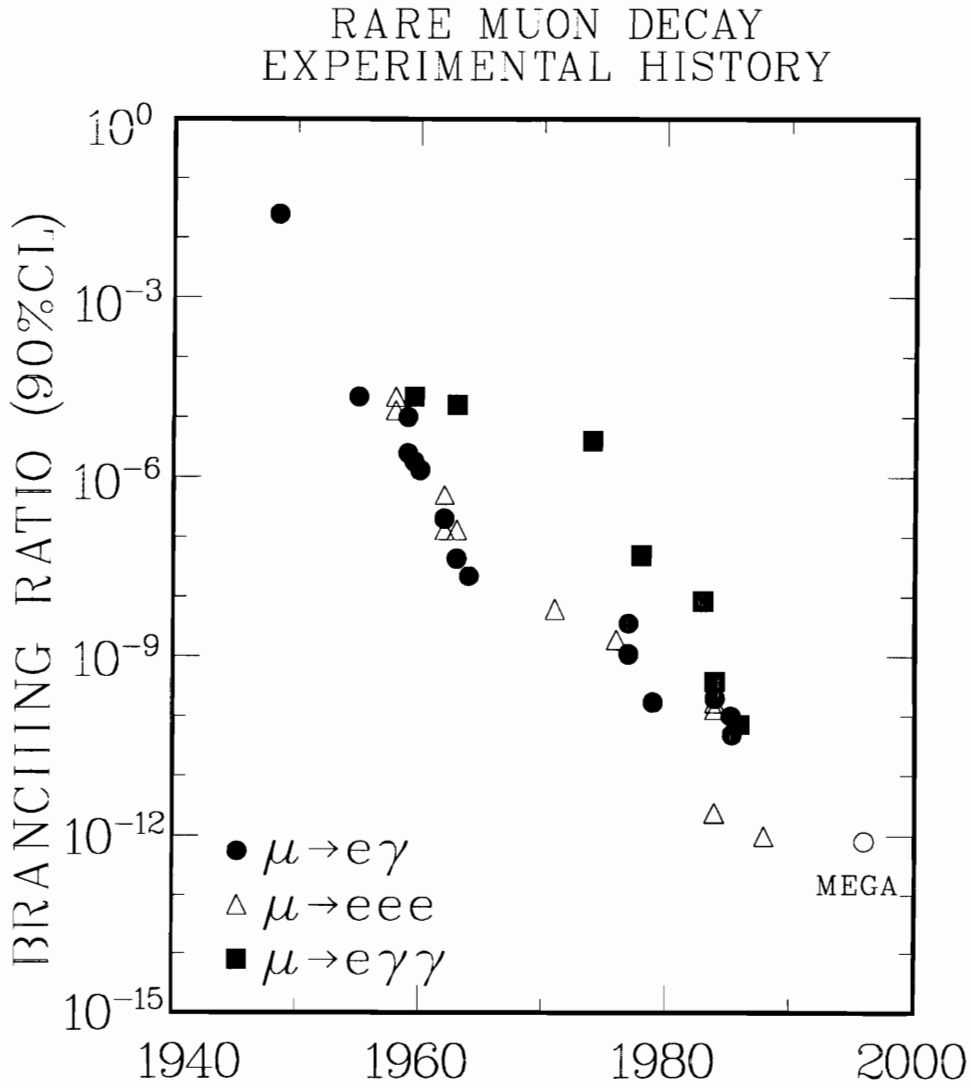


Figure 1: Rare muon decay experimental history. The open circle shows the expected sensitivity of MEGA experiment.

Table 1: μ decay modes

Modes	Fraction (Γ_i/Γ)
Γ_1 $e\nu\bar{\nu}$	0.986 ± 0.002 [1]
Γ_2 $e\gamma\nu\bar{\nu}$	$(1.4 \pm 0.4) \times 10^{-2}$ [2]
Γ_3 $e\nu\bar{\nu}ee$	$(3.4 \pm 0.4) \times 10^{-5}$ [3]
Γ_4 $e\gamma$	$< 4.9 \times 10^{-11}$ (90% <i>C.L.</i>)[4]
Γ_5 $e\gamma\gamma$	$< 7.2 \times 10^{-11}$ (90% <i>C.L.</i>)[4]
Γ_6 eee	$< 1.0 \times 10^{-12}$ (90% <i>C.L.</i>)[5]

short discussion follows.

In 1952, the search for the neutrinoless decay of the muon [6], $\mu^- N \rightarrow e^- N$, resulted in a branching ratio of 0.04 ± 0.05 . This result was the starting point in a series of experimental and theoretical developments that culminated in the formulation of the concepts of muon-number (L_μ) and electron-number (L_e) and in the postulates of muon-number and electron-number conservation. The scheme predicted the existence of a new type of neutrino in the normal muon decay $\mu \rightarrow e\nu_\mu\bar{\nu}_e$ with $\nu_\mu \neq \nu_e$. This fact was confirmed by Danby in 1962 [7].

In 1977, there was a rumor that the $\mu \rightarrow e\gamma$ process had been observed by an experimental group at the Swiss Institute for Nuclear Research (SIN) with a branching ratio of about 10^{-8} [8], but this experiment [9] ultimately reported only an upper limit of

$$B(\mu \rightarrow e\gamma) < 1.1 \times 10^{-9} \quad (90\% \text{ C.L.}). \quad (1)$$

In the same period, the $\mu e\gamma$ -I experiment [10] at the Los Alamos Meson Physics

Facility (LAMPF) reported an upper limit of

$$B(\mu \rightarrow e\gamma) < 1.7 \times 10^{-10} \quad (90\% \text{ C.L.}). \quad (2)$$

In the $\mu e\gamma$ -I detector, the positrons were measured using a magnetic spectrometer and photons were detected in a separate segmented NaI array. A sweeping magnet in front of the crystals removed all incoming charged particles.

Following the $\mu e\gamma$ -I experiment, a new collaboration at LAMPF was formed and a new experiment was designed to look for the three neutrinoless muon decays $\mu \rightarrow e\gamma$, $\mu \rightarrow eee$, and $\mu \rightarrow e\gamma\gamma$. The *Crystal Box* detector consisted of a cylindrical drift chamber for measuring positrons and banks of segmented NaI crystal arrays for detecting photons. The experiment yielded three new branching ratios limits[4, 11]:

$$B(\mu \rightarrow e\gamma) < 4.9 \times 10^{-11} \quad (90\% \text{ C.L.}). \quad (3)$$

$$B(\mu \rightarrow e\gamma\gamma) < 7.2 \times 10^{-11} \quad (90\% \text{ C.L.}). \quad (4)$$

$$B(\mu \rightarrow eee) < 1.3 \times 10^{-10} \quad (90\% \text{ C.L.}). \quad (5)$$

The SINDRUM experiment [5] at SIN, designed specifically to look for $\mu \rightarrow eee$, obtained the limit:

$$B(\mu \rightarrow eee) < 1.0 \times 10^{-12} \quad (90\% \text{ C.L.}). \quad (6)$$

A group at TRIUMF searched for the lepton-flavor-nonconserving reactions $\mu^- + Z \rightarrow e^- + Z$ and $\mu^- + Z \rightarrow e^+ + (Z - 2)$ [12]. Limits on such muon-electron and muon-positron conversion processes were obtained by using a time-projection chamber (TPC) to detect the electron or positron. The results are:

$$R_-(\text{Ti}) = \frac{\Gamma(\mu^- \text{Ti} \rightarrow e^- \text{Ti})}{\Gamma(\mu^- \text{Ti} \text{ capture})} < 4.6 \times 10^{-12} \quad (90\% \text{ C.L.}). \quad (7)$$

$$R_+(\text{Ti}) = \frac{\Gamma(\mu^- \text{Ti} \rightarrow e^+ \text{Ca})}{\Gamma(\mu^- \text{Ti} \text{ capture})} < 1.7 \times 10^{-10} \quad (90\% \text{ C.L.}). \quad (8)$$

More recently, SINDRUM reported slightly improved results [13] for these limits:

$$R_-(\text{Ti}) = \frac{\Gamma(\mu^- \text{Ti} \rightarrow e^- \text{Ti})}{\Gamma(\mu^- \text{Ti capture})} < 4.3 \times 10^{-12} \quad (90\% \text{ C.L.}). \quad (9)$$

$$R_+(\text{Ti}) = \frac{\Gamma(\mu^- \text{Ti} \rightarrow e^+ \text{Ca})}{\Gamma(\mu^- \text{Ti capture})} < 8.9 \times 10^{-11} \quad (90\% \text{ C.L.}). \quad (10)$$

In 1985, the MEGA collaboration was formed to look for $\mu \rightarrow e\gamma$ with a branching ratio sensitivity of about one part in 10^{13} with no background. To achieve this, the goal of the detector design was to improve the spectrometer resolutions to suppress the levels of the two dominant backgrounds of the experiment: $\mu \rightarrow e\gamma\nu\bar{\nu}$ (inner bremsstrahlung), and the random coincidence between a positron from normal decay $\mu \rightarrow e\nu\bar{\nu}$ and a photon from muon inner bremsstrahlung or positron annihilation in flight. The detector had to be able to work in a high beam rate environment so that more stopped muons could be taken per unit time [14].

The author of this thesis has been associated with this experiment since 1991, and has participated in the construction and commissioning of the positron chambers and associated gas system, and in the development of the online and offline software. He has done most of the analysis of the positron spectrometer data and obtained the final branching ratio sensitivity of the data taken in 1992, in cooperation with Mario Dzmidzic, a graduate student from the University of Houston.

The dissertation is organized as follows. Chapter 2 discusses the theoretical motivations for the $\mu \rightarrow e\gamma$ search. The design of the MEGA detector and associated software are described in Chapter 3. The detector response for both positron and photon spectrometers of the MEGA detector are presented in Chapter 4. This is followed finally by the results of the search for $\mu \rightarrow e\gamma$ in Chapter 5.

Chapter 2

Theoretical Background

2.1 Overview of the Standard Model

One of the major objectives of physics is to find out what, if any, are the fundamental constituents of the universe and to understand the nature of the forces by which they interact. Great progress on this has been made in the last twenty years.

The electromagnetic and weak interactions, believed to be two of the four basic interactions of nature, have been studied separately as quantum field theories since the middle of this century. The electromagnetic interaction was successfully described by a renormalizable field theory, known as quantum electrodynamics, which treats the interaction of two fermions as emission and re-absorption of a virtual photon. On the other hand, the weak interaction was formerly described by the four-fermion V-A Fermi theory. Even though it described muon and nuclear beta decay well, it was not considered by most physicists to be a final theory, because it was not renormalizable.

The most significant advance in weak interaction theory came from the construction of a renormalizable model by Weinberg and Salam that was based on the notion of spontaneously broken gauge symmetry. In this model, the weak and electromagnetic interactions were unified in a Yang-Mills gauge theory with the intermediate vector bosons W^\pm , Z^0 , and the photon as gauge bosons. The idea itself was not new. What was new in Weinberg and Salam's strategy was to attribute the observed dissimilarities between weak and electromagnetic interactions to a spontaneous breakdown of

the gauge symmetry. So far, no evidence contrary to this model has been found and it is referred to as the “Standard Model.”[15]

In the Standard Model, the gauge group is chosen to be $SU(2)_L \times U(1)_Y$ for weak and electromagnetic interactions. The assignment of the known fermions are shown in Fig. 2. There are three generations of leptons and quarks, arranged into left-handed doublets and right-handed singlets. Charged fermions participate in the electromagnetic interaction but only the doublets participate in the weak interaction. The gauge vector bosons A_μ and B_μ are introduced by an appropriate covariant derivative D_μ due to the requirement of gauge invariance. This covariant derivative is

$$D_\mu = \partial_\mu - ig\frac{\vec{\tau}}{2}\vec{A}_\mu - ig'\frac{1}{2}B_\mu \quad (11)$$

Here g and g' are the coupling constants of the gauge group $SU(2)_L$ and $U(1)_Y$, respectively. By making a rotation in weak isospin space, we can define the charged and neutral gauge bosons by

$$W^\pm_\mu = (A^1_\mu \pm iA^2_\mu)/\sqrt{2} \quad (12)$$

$$Z_\mu = A^3_\mu \cos \theta_W - B_\mu \sin \theta_W \quad (13)$$

$$A_\mu = A^3_\mu \sin \theta_W + B_\mu \cos \theta_W \quad (14)$$

where θ_W is the Weinberg angle. The coupling constants g and g' are related to the electric charge and the Weinberg angle through:

$$\tan \theta_W = g'/g \quad (15)$$

$$g = e/\sin \theta_W \quad (16)$$

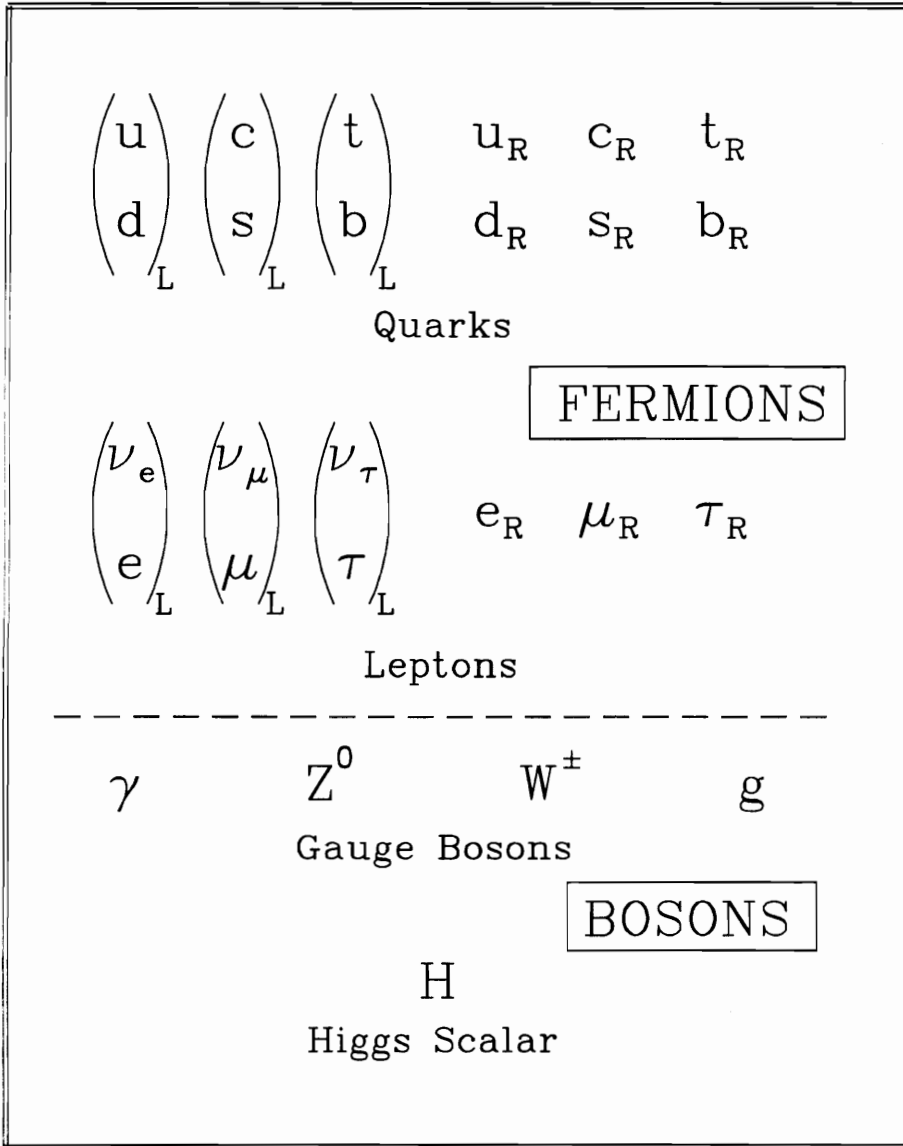


Figure 2: Constituents of the Standard Model

$$g' = e / \cos \theta_W \quad (17)$$

and θ_W is a model parameter.

The deficiency of this model as it stands is that the gauge bosons W^\pm and Z and the fermions are all massless. The problem is to generate the required masses while preserving the renormalizability of the gauge theory. This is achieved by spontaneous symmetry breaking, where the gauge symmetry of the Lagrangian remains but is “hidden” by the appearance of a preferred direction in weak isospin space.

An $SU(2)$ scalar field doublet is introduced in order that the fermions and gauge bosons acquire mass. Self-interaction of this scalar field causes spontaneous symmetry breaking, since the vacuum expectation value does not possess the $SU(2)_L \times U(1)_Y$ symmetry. The non-vanishing vacuum expectation value selects a preferred direction in the space of weak isospin and hypercharge, and thereby “spontaneously breaks” the Lagrangian down to a $U(1)_Q$ symmetry. Since the $SU(2)$ symmetry is broken, one of the four components of the scalar field, the Higgs particle, acquires mass. The other three (Goldstone particles) are “eaten” by the three gauge bosons W^\pm and Z so that they acquire mass. The Lagrangian still retains the $U(1)_Q$ symmetry and the remaining gauge boson—the photon—is massless.

The lepton and scalar fields are coupled by Yukawa terms in the Lagrangian:

$$L = G_l [\bar{l}_R (\Phi L) + (\bar{L} \Phi) l_R] \quad (18)$$

In the unitary gauge, the above term can be written as

$$L = (G_l v / \sqrt{2}) \bar{l} l - (G_l / \sqrt{2}) H \bar{l} l \quad (19)$$

Thus the lepton ℓ acquires a mass of $G_\ell v / \sqrt{2}$.

The masses of the quarks are given by mass matrices: $M_{ij} = \tilde{G}_{ij} v / \sqrt{2}$ for u, c, and t quarks; $M_{ij} = G_{ij} v / \sqrt{2}$ for d, s, and b quark. These matrices are not diagonal

Table 2: Lepton family number assignment and conservation laws.

L_e		L_μ		L_τ	
+1	e^-, ν_e	+1	μ^-, ν_μ	+1	τ^-, ν_τ
-1	$e^+, \bar{\nu}_e$	-1	$\mu^+, \bar{\nu}_\mu$	-1	$\tau^+, \bar{\nu}_\tau$
0	everything else	0	everything else	0	everything else
$\Sigma \Delta L_e = 0$		$\Sigma \Delta L_\mu = 0$		$\Sigma \Delta L_\tau = 0$	

since the quark mass eigenstates are not eigenstates with respect to the electroweak interaction. However there exists a unitary transformation between these two kinds of eigenstates that transforms the mass matrices to a diagonal form. The eigenvalues are the corresponding masses of quarks, and the relation between these two sets of eigenstates is

$$\begin{pmatrix} d_\theta \\ s_\theta \\ b_\theta \end{pmatrix}_L = U_L \begin{pmatrix} d \\ s \\ b \end{pmatrix}_L = \begin{pmatrix} V_{ud} & V_{us} & V_{ub} \\ V_{cd} & V_{cs} & V_{cb} \\ V_{td} & V_{ts} & V_{tb} \end{pmatrix} \begin{pmatrix} d \\ s \\ b \end{pmatrix}_L \quad (20)$$

Here U_L is the Cabibbo-Kobayashi-Maskawa matrix[16].

In the minimal Standard Model, the masses of neutrinos are strictly zero, and there is no interaction between the three lepton families. Thus, there is no corresponding non-diagonal CKM matrix in the lepton sector. That means that the separate lepton family numbers are conserved. Table 2 summarizes the lepton family number assignment and conservation laws. The Standard Model does not allow any lepton flavor changing processes such as $\mu \rightarrow e\gamma$ or $\mu \rightarrow eee$. It is important to test the Standard Model by searching for such lepton flavor changing processes.

Table 3: Proposed extensions to the Standard Model

perceived inadequacies	model extension
Why weak interaction is V-A?	L-R Symmetric
Many undetermined parameters	horizontal symmetries
Replication of the generations	horizontal gauge interaction
Too many elementary fields	composite models
Arbitrary Higgs sector	extra Higgs doublets/triplets
Gravity not included	supersymmetry
Elementary scalar field	Technicolor
Mass hierarchy problem	Technicolor & supersymmetry
Not a unified theory	grand-unified theories (GUTS)

2.2 Extensions to the Standard Model and $\mu \rightarrow e\gamma$

Many physicists believe that Standard Model is not a final theory. The model contains too many parameters since each fermion is accompanied by a separate parameter specifying its Higgs coupling, and hence its mass. Thus, there is no explanation as to why the ratio of the masses of these quarks and leptons have their special values. The model doesn't explain why P and C are not conserved. Although the minimal model sets the masses of neutrinos to be zero, these masses are not predictable by Standard Model, and so could be non-zero in the more general case. Furthermore, there is no explanation as to the number of generations of leptons and quarks. The conservation of baryon number and of the three types of lepton number have no associated gauge symmetry, and, thus, no satisfactory explanation. Many extensions to the Standard Model have been proposed to try to solve the perceived shortcomings of the theory. Some are listed in Table 3. Each model implies a branching ratio for $\mu \rightarrow e\gamma$ that may be compared with experimental measurements. We shall discuss some of them in the following sections.

2.2.1 Massive Neutrino Model

It is still an open question whether neutrinos are strictly massless. The current experimental bounds are:

1. $m_{\nu_e} \leq 7.2eV$, 3H β -decay spectrum[17],
2. $m_{\nu_\mu} \leq 0.27MeV$, $\pi \rightarrow \mu\nu_\mu$ (SIN) [18],
3. $m_{\nu_\tau} \leq 31MeV$, $\tau \rightarrow \pi\pi\pi\nu_\tau$ [19]

If the masses of the neutrinos are not equal to zero, the lepton families can mix as in the quark sector, which means that a neutrino of one lepton flavor may spontaneously change into that of another: for example, $\nu_e \leftrightarrow \nu_\mu$ may take place. If this neutrino oscillation exists, the lepton flavor nonconservation decay such as:

$$\mu \rightarrow e\gamma \tag{21}$$

could happen.

The basic idea of the Massive Neutrino Model is to retain the essential features of the Standard Model and introduce additional right-handed neutrinos. The corresponding leptonic CKM matrix elements $U_{\ell j}$ are defined by the following relation between the weak eigenstates ν_ℓ and the mass eigenstates ν_j of the neutrinos:

$$(\nu_e)_L = \sum_i U_{ei}\nu_i = U_{e1}\nu_1 + U_{e2}\nu_2 + U_{e3}\nu_3 \tag{22}$$

$$(\nu_\mu)_L = \sum_i U_{\mu i}\nu_i = U_{\mu 1}\nu_1 + U_{\mu 2}\nu_2 + U_{\mu 3}\nu_3 \tag{23}$$

$$(\nu_\tau)_L = \sum_i U_{\tau i}\nu_i = U_{\tau 1}\nu_1 + U_{\tau 2}\nu_2 + U_{\tau 3}\nu_3 \tag{24}$$

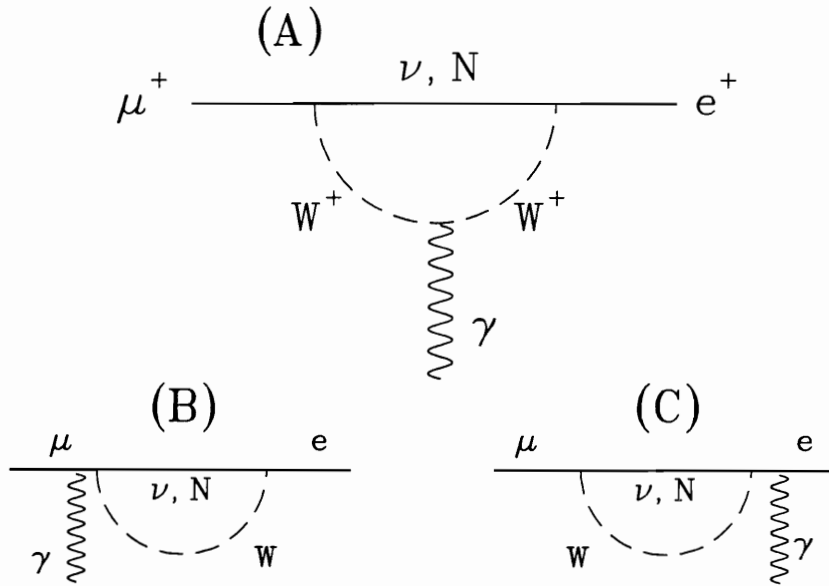


Figure 3: The Feynman diagrams for $\mu \rightarrow e\gamma$ with massive neutrinos

We can calculate the branching ratio of $\mu \rightarrow e\gamma$ decay from the processes shown in Fig. 3. The details will be given next section.

In this model, the branching ratio of $\mu \rightarrow e\gamma$ is proportional to

$$\left| \sum_j U_{ej}^* U_{\mu j} \frac{m_j^2}{M_W^2} \right|^2 \quad (25)$$

where m_j , U_{ej} and $U_{\mu j}$ are the mass of the j th generation neutrino, and the leptonic CKM matrix elements, respectively. These parameters are to be determined from experiments[21].

If we use the tight bounds on both the electron- and muon-neutrino mass [19, 20], neglect the contribution of the tau neutrino and use the experimental limits $|U_{e3}U_{\mu3}| < 2.5 \times 10^{-3}$ with $m_3 < 32\text{MeV}$; the upper limit of the branching ratio is

$$B(\mu \rightarrow e\gamma) < 10^{-22} \quad (26)$$

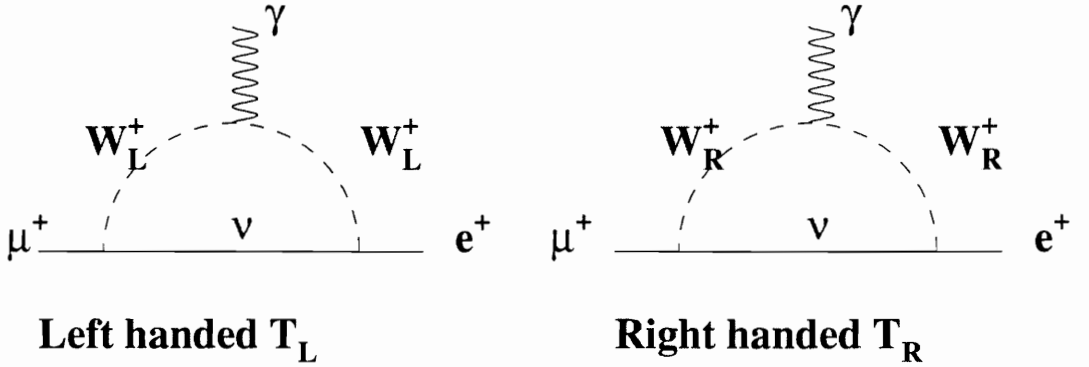


Figure 4: The T matrices of the Left-right Symmetric Model.

However, the current result from the LAMPF Crystal Box experiment is $B(\mu \rightarrow e\gamma) \sim 4.9 \times 10^{-11}$. This value is much larger than the prediction of the massive neutrino model.

2.2.2 Left-right Symmetric Electroweak Interaction Model

An obvious question about the Standard Model is why nature has selected the left-handed V-A interaction, with parity violation observed in weak interactions. Many physicists believe that this is probably a phenomenon at low momentum transfer for processes with $q^2 < 10^3$ GeV, and that for large momentum transfers, parity should be conserved even in weak interactions.

The left-right symmetric electroweak interaction model was proposed as an extension of the Standard Model to study CP violation phenomena in weak interactions. The Lagrangian for this model is both parity and charge invariant before spontaneous symmetry breaking, and the observed parity violation is attributed to non-invariance of the vacuum[22, 23]. The simplest gauge group, $SU(2)_L \otimes SU(2)_R \otimes U(1)$, is chosen and four charged bosons— W_L^+ , W_L^- , W_R^+ , W_R^- —and three neutral bosons— γ , Z_1^0 ,

Z_2° —are included. Since $SU(2)_R$ exists, there are additional right-handed doublets. The lepton sector is expressed as follows:

$$\begin{pmatrix} \nu_e \\ e \end{pmatrix}_L; \quad \begin{pmatrix} \nu_\mu \\ \mu \end{pmatrix}_L; \quad \begin{pmatrix} \nu_e \\ e \end{pmatrix}_R; \quad \begin{pmatrix} \nu_\mu \\ \mu \end{pmatrix}_R \quad (27)$$

Thus the Lagrangian of the model possesses both left-handed and right-handed charged current interactions. Two additional scalar fields are introduced to reduce the symmetries to $U(1)_Q$. This causes the masses of the vector bosons mediating the V+A interaction to be much larger than their V-A counterparts. Hence, at low q^2 , the effective Lagrangian appears to be left-handed as in the Standard Model. However, the left-right symmetry becomes apparent at large q^2 . The additional scalar fields will generate a large mass for the right-handed neutrino. The transition matrix of the processes $\mu \rightarrow e\gamma$ is given by

$$T(\mu \rightarrow e\gamma) = \sum_j T_{jL} + \sum_j T_{jR} \quad (28)$$

Here the T_{jL} and T_{jR} terms are for the processes shown in Fig. 4. They lead to the branching ratio:

$$B(\mu \rightarrow e\gamma) = \frac{3\alpha}{32\pi} \left(\frac{M_{W_L}}{M_{W_R}} \right)^4 \left| \sum_j U_{\mu j}^* U_{ej} \frac{m_j^2}{M_{W_R}^2} \right|^2 \quad (29)$$

where M_{W_R} is the mass of the right-handed W boson, and $U_{\mu j}$ and U_{ej} are the mixing matrix elements between right handed muon and electron neutrinos. If the absolute value of the mixing matrix element is $\sim 10^{-2}$ to 10^{-3} , and the ratio for $(M_{W_L}/M_{W_R})^2$ is about 1/100, then $B(\mu \rightarrow e\gamma)$ is of the order of 10^{-11} to 10^{-13} .

2.2.3 Grand Unified Theories

The gauge group of the Standard Model of strong and electroweak interaction is $SU(3) \times SU(2) \times U(1)$. $SU(3)$ is the gauge group of quantum chromodynamics

(QCD) while $SU(2) \times U(1)$ is the gauge group of the electroweak interaction. Since the total gauge group is a cross product, each group has its own gauge coupling constant. Even for the electroweak interaction, the model still has two parameters—the electric charge, e , and the Weinberg angle, θ_W . The aim of Grand Unified Theories (GUTs) is to find a gauge group with a single gauge coupling constant G to describe all interactions[24].

$SU(5)$ and $SO(10)$ grand unified theories seem to give a unification of α_1 , α_2 and α_3 which are the coupling constants of $SU(3)_c$, $SU(2)_W$ and $U(1)_Y$ respectively at α_{GUT} when the momentum transfer is the order of $Q_{GUT} \sim 10^{15}$ GeV/c. On the other hand, grand unified theories typically also predict additional constituents. For example, the 16 fermions in the $SO(10)$ model include all the 15 left-handed states in the Standard Model plus one additional neutrino N_L . It is possible for muon lepton number nonconserving processes to take place if the mass of this additional neutrino is large enough.

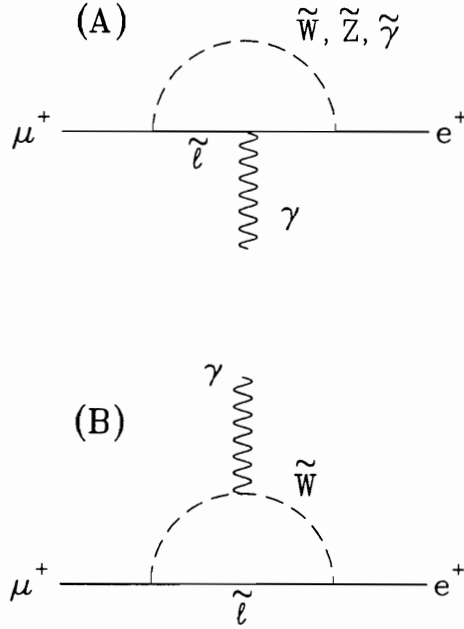
GUT models also suffer from the “hierarchy problem.” A possible solution is Supersymmetry, a higher symmetry model.

2.2.4 Supersymmetric Model

Supersymmetry goes beyond the quarks/leptons and gauge bosons unification of GUTs and attempts to unify the treatment of particles with different spins. It also seems to hold promise that the spin-2 graviton can be unified with all of the other particles.

The model introduces a large number of new particles called superpartners. There are new contributions to muon-number nonconserving processes from intermediate states that correspond to the superpartners of the usual particles. For example, $\mu \rightarrow e\gamma$ is allowed to occur via slepton mixing. The diagrams are shown in Fig. 5. The branching ratio is proportional to the square of the mass difference of sleptons of different generations[25]:

$$B(\mu \rightarrow e\gamma) \propto \frac{g_A^2}{M_B^2} \frac{\Delta M_{st}^2}{M_{st}^2} \quad (30)$$

Figure 5: $\mu \rightarrow e\gamma$ via slepton mixing.

where $g_{\tilde{A}}$ is the gauge constant, $M_{\tilde{sl}}$ the mass of the slepton, and $M_{\tilde{B}}$ is the mass of the \tilde{W} or \tilde{Z} or $\tilde{\gamma}$. The ratio is directly limited by mass-difference terms $\Delta M_{\tilde{sl}}$ of the sleptons, and if the following equation [26] holds:

$$\frac{1}{M_{\tilde{B}}^2} \frac{\Delta M_{\tilde{sl}}^2}{M_{\tilde{sl}}^2} < 10^{-8} \text{GeV}^{-2}$$

then the branching ratio will be 10^{-13} .

Due to the abundance of free parameters, the $\mu \rightarrow e\gamma$ branching ratio could be anywhere below the present experimental limits. The MEGA experiment can serve to limit the range of these parameters.

2.3 Calculation of the Rare Decay $\mu \rightarrow e\gamma$

In this section, we provide some details of the calculation of the $\mu \rightarrow e\gamma$ process using the Massive Neutrino Model. The computation is done in the R_ξ gauge but is

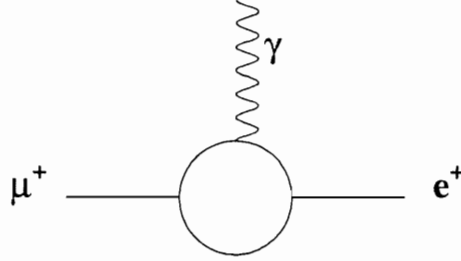


Figure 6: The block diagram of $\mu \rightarrow e\gamma$.

transformed to the unitary gauge in the end to give the result of equation (25) [27].

2.3.1 Operator Analysis

The $\mu \rightarrow e\gamma$ amplitude of Fig. 6 is

$$T(\mu \rightarrow e\gamma) = \epsilon^\lambda(q) \langle e | J_\lambda | \mu \rangle \quad (31)$$

where the current matrix element $\langle e | J_\lambda | \mu \rangle$ is given by:

$$\langle e | J_\lambda | \mu \rangle = \bar{u}_f(p - q) \left[i q^\nu \sigma_{\lambda\nu} (A + B\gamma_5) + \gamma_\lambda (C + D\gamma_5) + q_\lambda (E + F\gamma_5) \right] u_i(p) \quad (32)$$

This can be simplified by the following considerations:

1. Current conservation of the electromagnetic currents, $\partial^\nu J_\nu = 0$, require C and D to be zero.
2. $q^\nu \epsilon_\nu(q)$ is equal to zero, thus the last term in equation (32) vanishes.

If we neglect the mass of the electron and suppose that A and B have the same values, equation (31) can be written as

$$T(\mu \rightarrow e\gamma) = (iA)\epsilon^\lambda(q)\bar{u}_f(p-q)\sigma_{\lambda\nu}q^\nu(1+\gamma_5)u_i(p) \quad (33)$$

Note that (after neglecting the mass of electron) the Dirac equation is:

$$\bar{u}(p-q)(\not{p} - \not{q}) = 0 \quad . \quad (34)$$

Then we have

$$\begin{aligned} T(\mu \rightarrow e\gamma) &= iA\epsilon^\lambda(q)\bar{u}_f(p-q)\sigma_{\lambda\nu}q^\nu(1+\gamma_5)u_i(p) \\ &= (-A)\frac{1}{2}\bar{u}_f(p-q)[2g_{\lambda\nu}\epsilon^\lambda q^\nu - 2\not{q}\not{\epsilon}](1+\gamma_5)u_i(p) \\ &= (-A)\bar{u}_f(p-q)[\epsilon^\lambda q_\lambda - 2p \cdot \epsilon + \not{p}\not{\epsilon}](1+\gamma_5)u_i(p) \\ &= A\bar{u}_f(p-q)[2p \cdot \epsilon - \epsilon \cdot \gamma m_\mu](1+\gamma_5)u_i(p) \\ &= A\bar{u}_f(p-q)(1+\gamma_5)[2p \cdot \epsilon - \epsilon \cdot \gamma m_\mu]u_i(p) \end{aligned} \quad (35)$$

Our goal is to calculate the invariant amplitude A, and we need only concentrate on the $p \cdot \epsilon$ term.

2.3.2 The Diagrams of $\mu \rightarrow e\gamma$

In Fig. 7, we have to consider the different particles, the massive neutral lepton and the Higgs particle, where:

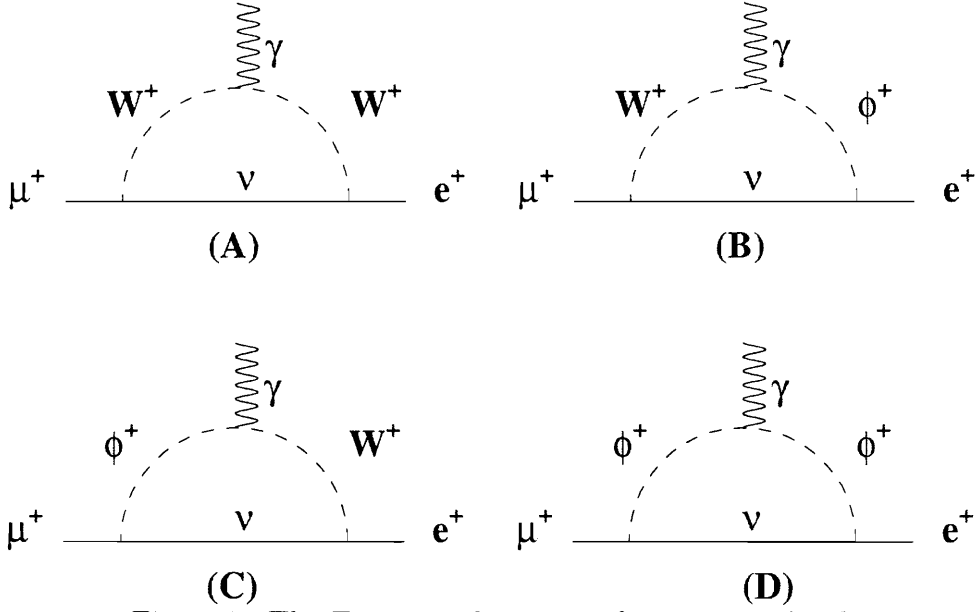
W ; the vector boson.

ν_i ; the massive neutral lepton.

ϕ ; the scalar particle.

2.3.3 Calculation of Transition Matrix of $\mu \rightarrow e\gamma$

To calculate the diagrams in the previous section, we have to consider the fermion propagator and the vector boson—photon vertex. For the propagator, we have


 Figure 7: The Feynman diagrams of $\mu \rightarrow e\gamma$ under R_ξ gauge.

$$\begin{aligned}
 iS_{AB,L}(x-x') &= \langle 0|T[\psi_{AL}(x)\bar{\psi}_{BL}(x')]|0\rangle \\
 &= (1-\gamma_5)\langle 0|T[\psi_A(x)\bar{\psi}_B(x')]|0\rangle(1+\gamma_5) \\
 &= \sum_i U_{Bi}^* U_{Ai} (1-\gamma_5) \langle 0|T[\psi_{Ai}(x)\bar{\psi}_{Bi}(x')]|0\rangle (1+\gamma_5) \\
 &= \sum_i U_{Bi}^* U_{Ai} (1-\gamma_5) iS_{AB,i}(x-x') (1+\gamma_5)
 \end{aligned} \tag{36}$$

In momentum space, it can be expressed as

$$iS_{AB,L}(p) = \sum_i U_{Bi}^* U_{Ai} (1-\gamma_5) \frac{i}{\not{p} - m_i} (1+\gamma_5) . \tag{37}$$

The vector boson-photon vertex yields

$$\Gamma_{\mu\nu\tau}(k_1, k_2, k_3) = (-ie) [g_{\mu\nu}(k_1 - k_2)_\tau + g_{\tau\mu}(k_3 - k_1)_\nu + g_{\nu\tau}(k_2 - k_3)_\mu] . \tag{38}$$

We begin to calculate Fig. 7-a. Using the Feynman rules, the transition matrix can be written as

$$\begin{aligned}
T(a) &= \sum_j T_j(a) \\
&= (-i) \sum_j \int \frac{d^4 k}{(2\pi)^4} \bar{u}_f(p-q) \left[\frac{ig}{2\sqrt{2}} U_{fj}^* \gamma_\mu (1 - \gamma_5) \frac{i}{\not{p} + \not{k} - m_j} \frac{ig}{2\sqrt{2}} U_{ij} \gamma_\nu (1 - \gamma_5) \right] u_i(p) \times \\
&\quad \times i \Delta^{\nu\beta}(k) i \Delta^{\alpha\mu}(k+q) (-ie) \Gamma_{\gamma\alpha\beta} \epsilon^\gamma(q)
\end{aligned}$$

We can simplify the above equation by using

$$\Gamma_{\alpha\beta} = \epsilon^\gamma(q) \Gamma_{\gamma\alpha\beta} = [g_{\alpha\beta}(2k \cdot \epsilon) - (k+2q)_\beta \epsilon_\alpha - (k-q)_\alpha \epsilon_\beta] \quad (39)$$

with $\sum_j U_{fj}^* U_{ij} = 0$, and

$$\begin{aligned}
\sum_j U_{fj}^* U_{ij} \frac{i}{\not{p} + \not{k} - m_j} &= i \sum_j U_{fj}^* U_{ij} \frac{\not{p} + \not{k} + m_j}{(p+k)^2 - m_j^2} \\
&= i \sum_j U_{fj}^* U_{ij} (\not{p} + \not{k} + m_j) \left[\frac{1}{(p+k)^2} + \frac{m_j^2}{(p+k)^4} + \dots \right] \\
&= i \sum_j U_{fj}^* U_{ij} (\not{p} + \not{k} + m_j) \frac{m_j^2}{(p+k)^4}
\end{aligned} \quad (40)$$

If $m_j(p+k)^{-2} \sim \epsilon$, then

$$\epsilon < \epsilon^2 m_j < \epsilon^2 (p+k)_\mu$$

and in equation (40), we can drop the m_j term and keep the term $(\not{p} + \not{k})$. Then;

$$\begin{aligned}
T(a) &= i \frac{eg^2}{4} \sum_j U_{fj}^* U_{ij} m_j^2 \int \frac{d^4 k}{(2\pi)^4} \frac{1}{(p+k)^4} \left[\bar{u}_f(p-q) \gamma_\mu (\not{p} + \not{k}) \gamma_\nu (1 - \gamma_5) u_i(p) \right] \\
&\quad \times \Delta^{\mu\alpha}(k+q) \Gamma_{\alpha\beta}(k, q, \epsilon) \Delta^{\nu\beta}(k)
\end{aligned}$$

Defining

$$C = \frac{eg^2}{4} \sum_j U_{fj}^* U_{ij} m_j^2 \quad (41)$$

and

$$N_{\mu\nu} = \bar{u}_f(p-q)\gamma_\mu(\not{p} + \not{k})\gamma_\nu(1 - \gamma_5)u_i(p) \quad (42)$$

we can rewrite $T(a)$ as

$$T(a) = iC \int \frac{d^4k}{(2\pi)^4} \frac{1}{(p+k)^4} N^{\mu\nu} \Delta_{\mu\alpha}(k+q) \Gamma^{\alpha\beta}(k, q, \epsilon) \Delta_{\nu\beta}(k) \quad (43)$$

where Δ is the W vector-propagator in the R_ξ -gauge:

$$\begin{aligned} \Delta_{\mu\nu}(k) &= \Delta_{\mu\nu}^{(1)}(k) + \Delta_{\mu\nu}^{(2)}(k) \\ &= -\frac{g_{\mu\nu} - M^{-2}k_\mu k_\nu}{k^2 - M^2} - \frac{M^{-2}k_\mu k_\nu}{k^2 - M^2} \end{aligned} \quad (44)$$

It is easy to see that

$$\Delta_{\mu\alpha}^{(2)}(k+q) \Gamma^{\alpha\beta} \Delta_{\nu\beta}^{(2)}(k) = 0 \quad (45)$$

because

$$(k+q)_\alpha k_\beta \Gamma^{\alpha\beta} = 0 \quad (46)$$

therefore, we have

$$\begin{aligned} \Delta_{\mu\alpha}(k+q) \Gamma^{\alpha\beta} \Delta_{\nu\beta}(k) &= \Delta_{\mu\alpha}^{(1)}(k+q) \Gamma^{\alpha\beta} \Delta_{\nu\beta}^{(1)}(k) \\ &\quad + \Delta_{\mu\alpha}^{(1)}(k+q) \Gamma^{\alpha\beta} \Delta_{\nu\beta}^{(2)}(k) + \Delta_{\mu\alpha}^{(2)}(k+q) \Gamma^{\alpha\beta} \Delta_{\nu\beta}^{(1)}(k) \end{aligned}$$

The first term is

$$\begin{aligned} \Delta_{\mu\alpha}^{(1)}(k+q) \Gamma^{\alpha\beta} \Delta_{\nu\beta}^{(1)}(k) &= \\ \Gamma^{\alpha\beta} \frac{g_{\mu\alpha} - M^{-2}(k+q)_\mu (k+q)_\alpha}{(k+q)^2 - M^2} \cdot \frac{g_{\nu\beta} - M^{-2}k_\nu k_\beta}{k^2 - M^2} \end{aligned}$$

$$= \frac{1}{[(k+q)^2 - M^2][k^2 - M^2]} [\Gamma_{\mu\nu} - M^{-2}(k+q)_\mu [\Gamma_{\nu\beta}(k+q)^\beta] - M^{-2}k_\nu (\Gamma_{\mu\beta}k^\beta)]$$

and the cross terms are

$$\Delta_{\mu\alpha}^{(1)}(k+q)\Gamma^{\alpha\beta}\Delta_{\nu\beta}^{(2)}(k) = \frac{1}{[(k+q)^2 - M^2][k^2 - \xi M^2]} M^{-2}k_\nu (\Gamma_{\mu\beta}k^\beta)$$

$$\Delta_{\mu\alpha}^{(2)}(k+q)\Gamma^{\alpha\beta}\Delta_{\nu\beta}^{(1)}(k) = \frac{1}{[(k+q)^2 - \xi M^2][k^2 - M^2]} M^{-2}(k+q)_\nu (\Gamma_{\mu\beta}(k+q)^\beta)$$

We write

$$\begin{aligned} & N^{\mu\nu}\Delta_{\mu\alpha}(k+q)\Gamma^{\alpha\beta}\Delta_{\nu\beta}(k) \\ = & \frac{S_1 - S_2 - S_3}{[(k+q)^2 - M^2][k^2 - M^2]} + \frac{S_2}{[(k+q)^2 - M^2][k^2 - \xi M^2]} + \frac{S_3}{[(k+q)^2 - \xi M^2][k^2 - M^2]} \end{aligned}$$

where the S_1 , S_2 and S_3 are

$$S_1 = \Gamma^{\mu\nu}N_{\mu\nu}; \quad S_2 = M^{-2}(\Gamma^{\mu\lambda}k_\lambda)(N_{\mu\nu}k^\nu); \quad S_3 = M^{-2}[\Gamma^{\mu\lambda}(k+q)_\lambda][N_{\mu\nu}(k+q)^\nu]$$

Using the above formula, we can re-express the term $T(a)$ as

$$\begin{aligned} T(a) = & iC \int \frac{d^4k}{(2\pi)^4} \frac{1}{(p+k)^4} = \\ & \left[\frac{S_1 - S_2 - S_3}{[(k+q)^2 - M^2][k^2 - M^2]} + \frac{S_2}{[(k+q)^2 - M^2][k^2 - \xi M^2]} + \frac{S_3}{[(k+q)^2 - \xi M^2][k^2 - M^2]} \right] \end{aligned}$$

Using the identities

$$\frac{1}{a_1 \cdot a_2 \cdots a_n} = (n-1)! \int \frac{dx_1 \cdot dx_2 \cdots dx_n \delta(1 - \sum_j^n x_j)}{[a_1 x_1 + a_2 x_2 + \cdots + a_n x_n]^n}$$

$$\frac{1}{a_1^2 \cdot a_2 \cdots a_n} = n! \int \frac{dx_1 \cdot dx_2 \cdots dx_n \delta(1 - \sum_j^n x_j)}{[a_1 x_1 + a_2 x_2 + \cdots + a_n x_n]^{n+1}}$$

and changing the integration variable, we have

$$T(a) = 3!(iC) \int_0^1 x_1 dx_1 dx_2 \int \frac{dk^4}{(2\pi)^4} \left[\frac{\bar{S}_1 - \bar{S}_2 - \bar{S}_3}{(k^2 - a^2)^4} + \frac{\bar{S}_2}{(k^2 - b^2)^4} + \frac{\bar{S}_3}{(k^2 - d^2)^4} \right] \quad (47)$$

and the parameters a^2 , b^2 and d^2 have the following forms:

$$a^2 = (1 - x_1)M^2 + x_1 m_\mu^2 \dots \quad (48)$$

$$b^2 = [(1 - x_1 - x_2)\xi + x_2]M^2 \dots \quad (49)$$

$$d^2 = [(1 - x_1 - x_2) + \xi x_2]M^2 \dots \quad (50)$$

Picking only the $p \cdot \epsilon$ terms in \bar{S}_1 , \bar{S}_2 and \bar{S}_3 , we have

$$\bar{S}_1 = (p \cdot \epsilon) \bar{u}_f(p - q)(1 + \gamma_5) u_i(p) 2m_\mu [2(1 - x_1)^2 + 2(x_1 - 1)x_2]$$

$$\bar{S}_2 = -k^2 (p \cdot \epsilon) \bar{u}_f(p - q)(1 + \gamma_5) u_i(p) \frac{m_\mu}{M^2} [(3x_2 - 1) + [2x_1^2 - x_1 + x_2(2x_1 - \frac{1}{2})]]$$

$$\bar{S}_3 = -k^2 (p \cdot \epsilon) \bar{u}_f(p - q)(1 + \gamma_5) u_i(p) \frac{m_\mu}{M^2} [2x_2^2 + x_1 + x_2(2x_1 - \frac{1}{2})].$$

Using

$$\int \frac{dk^4}{(2\pi)^4} \frac{1}{(k^2 - a^2)^4} = \frac{i}{96\pi^2 a^4}$$

$$\int \frac{dk^4}{(2\pi)^4} \frac{k^2}{(k^2 - a^2)^4} = \frac{(-i)}{48\pi^2 a^2}$$

and integrating over the Feynman parameters x_1 and x_2 , we have for Fig. 7-a

$$A(a) = \frac{C}{64\pi^2} \frac{m_\mu}{M^4} [1 - \frac{1}{3} \frac{\ln \xi}{\xi - 1} + \frac{1}{\xi - 1} (\frac{\xi \ln \xi}{\xi - 1} - 1)] \quad (51)$$

Using the same methods, we can calculate the other three diagrams. Fig. 7-b gives

$$A(b) = \frac{C}{64\pi^2} \frac{m_\mu}{M^4} [\frac{5}{6\xi} - \frac{4\ln \xi}{3(\xi - 1)} - \frac{7}{3} \frac{1}{\xi - 1} (\frac{\xi \ln \xi}{\xi - 1} - 1)] \quad (52)$$

Fig. 7-c gives

$$A(c) = \frac{C}{64\pi^2} \frac{m_\mu}{M^4} \left[\frac{5}{6\xi} - \frac{\ln\xi}{\xi-1} + \frac{1}{3} \frac{1}{\xi-1} \left(\frac{\xi \ln\xi}{\xi-1} - 1 \right) \right], \quad (53)$$

and Fig. 7-d gives

$$A(d) = -\frac{C}{32\pi^2} \frac{m_\mu}{M^4} \frac{5}{6\xi}. \quad (54)$$

If we choose the unitary gauge ($\xi \rightarrow \infty$), we have the following expression for the T matrix:

$$T = T(a) + T(b) + T(c) + T(d) = A \bar{u}_f(p-q)(1 + \gamma_5)(2p \cdot \epsilon) u_i(p)$$

A is expressed as

$$A = B = e \frac{g^2}{8M^2} \frac{m_\mu}{32\pi^2} \sum_j U_{fj}^* U_{ij} \frac{m_j^2}{M^2} \quad (55)$$

2.3.4 Results for the Rare Decay $\mu \rightarrow e\gamma$

Using the results of equation (55), we have $\mu \rightarrow e\gamma$

$$\Gamma(\mu \rightarrow e\gamma) = \frac{m_\mu^3}{8\pi} (|A|^2 + |B|^2) = \frac{m_\mu^3}{4\pi} |A|^2 \quad (56)$$

while for $\mu \rightarrow e\nu\bar{\nu}$, we have

$$\Gamma(\mu \rightarrow e\nu\bar{\nu}) = \frac{m_\mu^5}{192} \frac{G_F^2}{\pi^3} \quad \left(\frac{G_F}{\sqrt{2}} = \frac{g^2}{8M^2} \right) \quad (57)$$

The $\mu \rightarrow e\gamma$ branching ratio is

$$B(\mu \rightarrow e\nu) = \frac{\Gamma(\mu \rightarrow e\gamma)}{\Gamma(\mu \rightarrow e\nu\bar{\nu})} = \frac{3\alpha}{32\pi} \left| \sum_j U_{fj}^* U_{ij} \left(\frac{m_j^2}{M^2} \right) \right|^2 \quad (58)$$

as expressed earlier in equation (25).

Chapter 3

Experimental Design

3.1 Overview

In nuclear and particle physics experiments, momentum is typically measured by a magnetic spectrometer (where the curvature of a particle's track in a known magnetic field can be related to its momentum if the charge is known), and energy is measured by a calorimeter (where a particle comes to rest in a block of material and a signal proportional to the size of the electromagnetic or hadronic cascade is extracted). Generally speaking, a spectrometer should be very light so that it doesn't deform the track, while a calorimeter should be massive so that it contains the entire cascade of the interacting particle.

The MEGA experiment uses separate spectrometers to measure the momenta of both positrons and photons (the latter by converting them to e^+e^- pairs then measuring the pair's momenta) that would be emitted in the lepton family number nonconserving decay $\mu^+ \rightarrow e^+\gamma$. The original goal of the experiment, as stated in the proposal to the LAMPF Program Advisory Committee, was to achieve a branching ratio sensitivity of one part in 10^{-13} [14], 500 times better than the result from the Crystal Box experiment[4]. The present more realistic estimate of the ultimate sensitivity of the MEGA experiment is 7.0×10^{-13} .

The design of the MEGA experiment was driven by the desire to avoid the limitations of the previous generation Crystal Box experiment. The Crystal Box detector

was built to search simultaneously for three different muon decay modes: $\mu \rightarrow e\gamma$, $\mu \rightarrow e\gamma\gamma$ and $\mu \rightarrow eee$ [28]. The best choice that met these physics objectives within a reasonable budget was a non-magnetic detector that used a segmented NaI(Tl) calorimeter for both photon and electron energies, and a drift chamber for electron (straight-line) direction. For $\mu \rightarrow e\gamma$, the energy resolution of crystals at 52.8 MeV is only about 8% (FWHM), limiting the ability to reject known backgrounds such as $\mu \rightarrow e\gamma\nu\bar{\nu}$ by cuts on energy. Also, NaI(Tl) crystals are inherently slow devices ($\sim\mu s$ light collection times) that limited the time resolution and the muon stopping rate in the Crystal Box[29]. The Crystal Box was ultimately background limited, in the sense that further running to improve the branching ratio sensitivities was no longer profitable since the gains in sensitivity would only scale as \sqrt{N} for N muon decays.

The MEGA detector's design was optimized to look for $\mu \rightarrow e\gamma$, with the following objectives:

1. Improve the resolutions of measured kinematic quantities (energy, direction, time) to better reject the backgrounds and defer the onset of the background-limit regime to a branching ratio of $\leq 10^{-13}$.
2. Raise the rate capacity of the detector systems to fully utilize the LAMPF beam, so that the branching ratio sensitivity of 10^{-13} could actually be achieved.

The design called for (1) a large solenoid to provide the magnetic field for a spectrometer to measure the positron's momentum, and to separate the volumes of the photon and positron detectors, thereby assuring a relatively quiet environment for the photon detector, (2) fast thin multiwire proportional chambers and plastic scintillators to measure positron momentum and time with high precision and at high rate, (3) a set of pair spectrometers measure photon momentum via $\gamma \rightarrow e^+e^-$.

Figs. 8–10 show the MEGA detector from a cut away view, the end view and the side view respectively. The central core contains the positron spectrometer, which is composed of eight cylindrical multiwire proportional chambers (MWPC) and two segmented barrels of plastic scintillators. The photon detector, located outside the positron spectrometer, is composed of three independent layers of pair spectrometer.

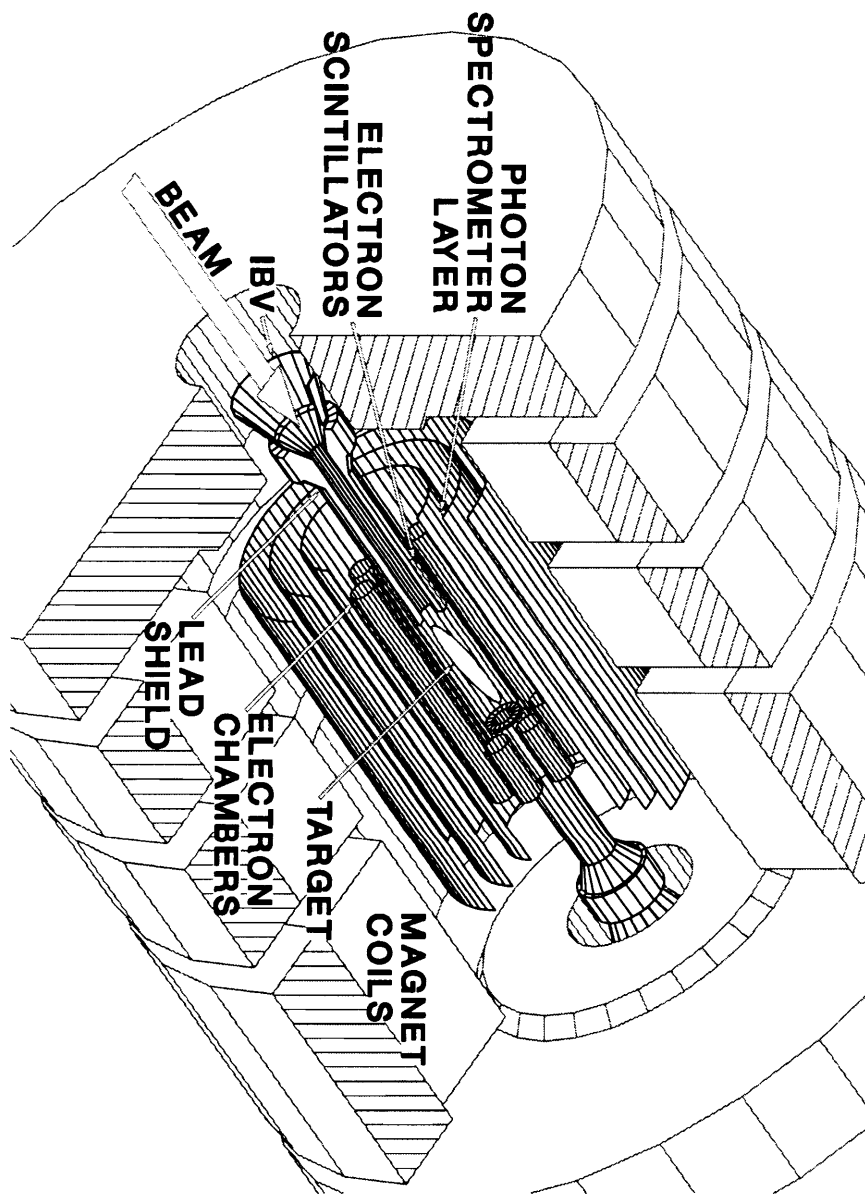


Figure 8: Cut away view of MEGA detector.

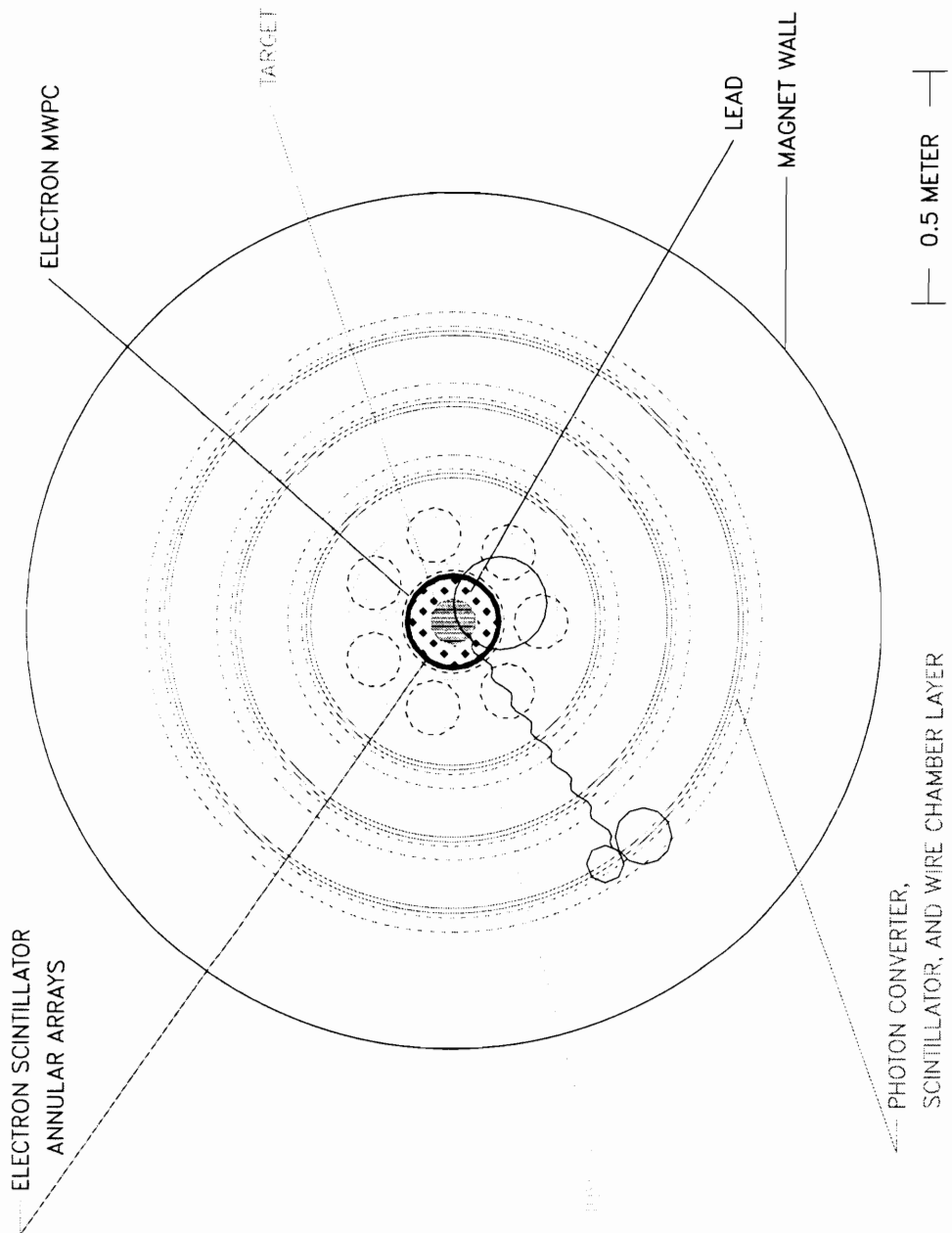


Figure 9: End view of MEGA detector.

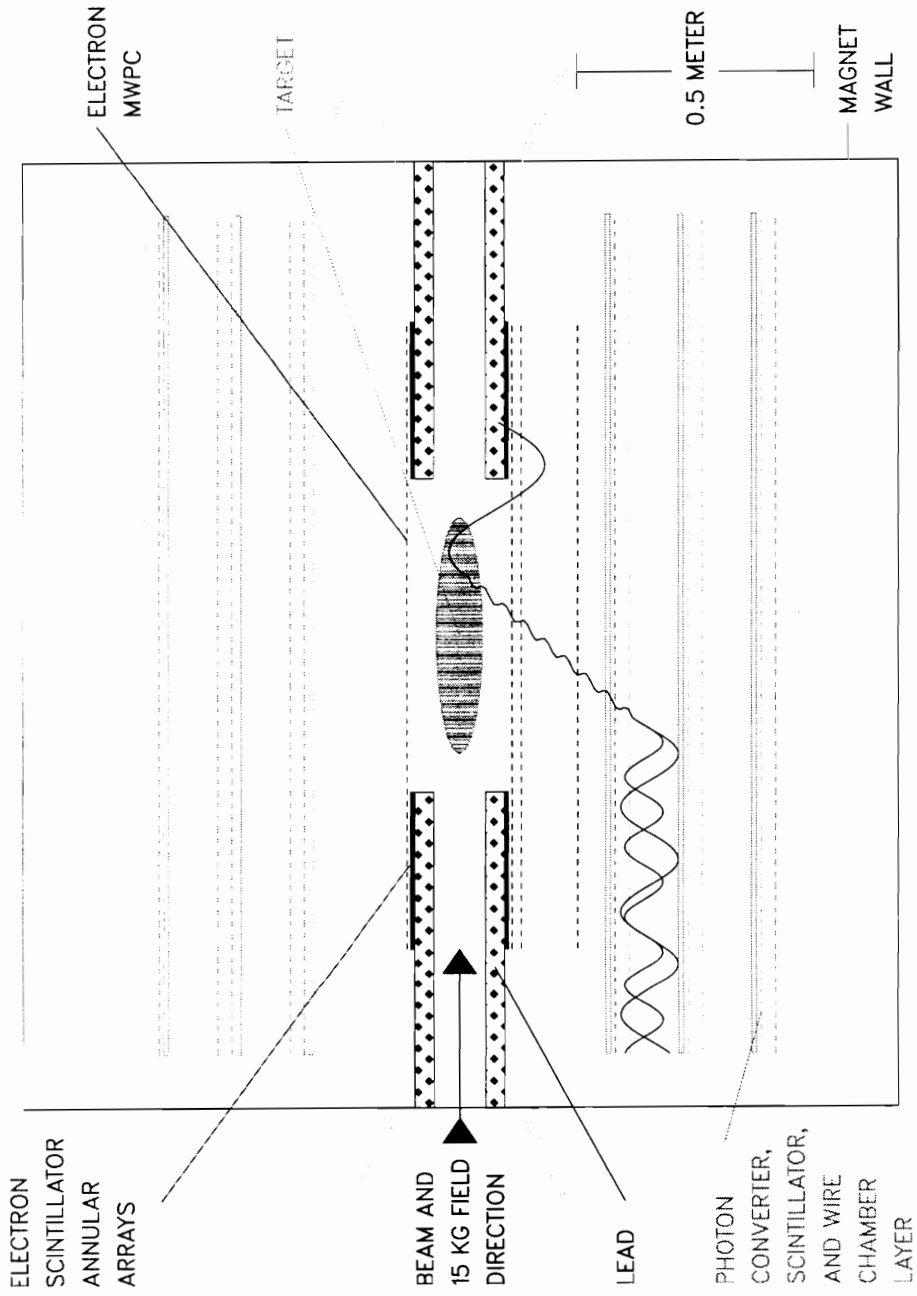


Figure 10: Side view of MEGA detector.

Each cylindrical pair spectrometer contains two sheets of lead converters separated by a MWPC, three layers of drift chambers, and segmented scintillator barrels.

The MEGA data acquisition system contains the detector-mounted preamplifiers, rack-mounted amplifier-discriminators, a custom-built trigger system, FASTBUS TDCs, ADCs and latches, an on-line workstation farm of eight DECstation 5000/240 processors, and a master microVAX computer.

A 29 MeV/c muon beam is brought into the apparatus along the solenoidal axis. The muons come to rest in a thin, steeply canted mylar target, then decay—nearly always via the “Michel decay” process $\mu \rightarrow e\nu\bar{\nu}$. If a muon stops on the target and decays via $\mu \rightarrow e\gamma$, the photon can convert into an electron-positron pair in one of the two lead sheets in a photon pair spectrometer. The e^+e^- pair will separate in the magnetic field and the drift chambers will track their motion; their track curvatures will be used to determine their momenta. The photon time is recorded by the plastic scintillators as the pair passes through them after the first half loop. The MWPC between the two lead sheets distinguishes between “inner” and “outer” conversions to better correct the average energy loss of the e^+e^- pair in the spectrometer materials. Meanwhile, the positron from the same decay will be tracked by eight MWPCs—one larger coaxial chamber named SNOW WHITE and seven small off-axis chambers named DWARFS. The positron momentum is extracted from the hits in the axial anodes and stereo cathodes in these MWPCs; its time is measured by the positron scintillator barrels at either end of the positron spectrometer.

The hardware trigger is generated from the pattern of hits in the photon pair spectrometer MWPC and scintillator barrel. If the azimuthal spread of these hits is large enough—indicative of a fairly energetic photon—then a trigger is generated and the hit information from the wire chambers and the timing and pulse information from the scintillators are digitized by the FASTBUS modules and recorded in a memory buffer within each module. At the end of a LAMPF macropulse (typically 750 μ s duration and 80 Hz repetition rate, i.e., 6% duty factor), all of the memory buffers for the 20 or so stored events are flushed into one of the online workstations. There, the data are unpacked, reformatted and sorted into separate events. The online filter code examines the hits for each event, does a partial reconstruction of the photon and

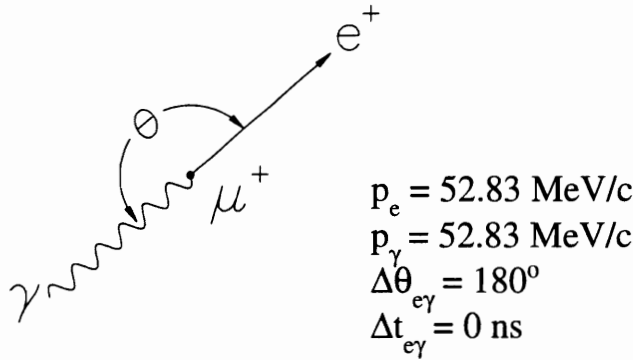


Figure 11: The kinematics of $\mu \rightarrow e\gamma$ decay at rest.

positron if necessary, and discards events that clearly do not satisfy the kinematic requirements of $\mu \rightarrow e\gamma$. The remaining candidate events are passed to the master microVAX for taping and future off-line analysis.

In the following sections, the various components of the MEGA detector design are described in more detail. Before that, we give the estimation of background for $\mu \rightarrow e\gamma$ that drove the experiment design, followed by a description of the target, magnet and beam of LAMPF.

3.2 Background and Sensitivity

When searching for a rare physical process such as $\mu \rightarrow e\gamma$, the separation of the signal from the background is always limited by the finite resolution of the detector. The kinematic character of $\mu \rightarrow e\gamma$ in the center of mass helps a great deal in this regard: a muon at rest decays into a positron and a photon in time coincidence, with equal and opposite momenta (see Fig. 11). The following four kinematic parameters allow us to identify the decay products from $\mu \rightarrow e\gamma$ [32]:

$$\begin{aligned}
p_e &= (m_\mu^2 - m_e^2)/2m_\mu = (52.827959 \pm 0.000017) \text{ MeV}/c \\
p_\gamma &= p_e \\
\theta_{e\gamma} &= 180^\circ \\
\Delta t_{e\gamma} &= 0
\end{aligned}$$

The dominant sources of background are the allowed prompt decay $\mu \rightarrow e\gamma\nu\bar{\nu}$ (“Inner Bremsstrahlung”) and random coincidences between an energetic photon and an independent energetic positron roughly back-to-back with the photon. In the latter case, the main source of high energy photons are inner bremsstrahlung (typically emitted with a very soft positron) and a photon from the annihilation-in-flight of an energetic Michel decay positron. Fig. 12 shows a diagram of the integral number of photons per muon decay above a given cutoff energy (measured in units of 52.8 MeV) from these sources in the MEGA apparatus. We see from this figure that the higher the photon energy cutoff can be set, the better the backgrounds to $\mu \rightarrow e\gamma$ are suppressed. When the photon energy cutoff is set to $0.98 \cdot m_\mu/2$, only 1 in 400,000 muon decays gives rise to such an energetic photon, and inner bremsstrahlung and annihilation-in-flight are roughly equally represented.

If a similar energy cutoff of $0.98 \cdot m_\mu/2$ is imposed on the positron energy as well, the phase space for finding an inner bremsstrahlung event with $E_\gamma > 0.98 \cdot m_\mu/2$ and $E_e > 0.98 \cdot m_\mu/2$ is extremely small (probability $\sim 10^{-13}$ per muon decay). With such cutoffs, the prompt background can be ignored. The expected background level from random coincidences is given by the following expression:

$$P_{bkg} = P_e \times P_\gamma \times P_t \times f_{e\gamma} \times f_\gamma \times P_{IBV} \quad , \quad (59)$$

where:

- P_e : probability of finding a positron within the positron energy window
- P_γ : probability of finding a photon within the photon energy window
- P_t : probability of an $e\gamma$ time coincidence within the timing window
- $f_{e\gamma}$: probability of back-to-back tracks within the opening angle window
- f_γ : probability of the photon pointing back to the positron origin
- P_{IBV} : inefficiency of inner bremsstrahlung veto detector

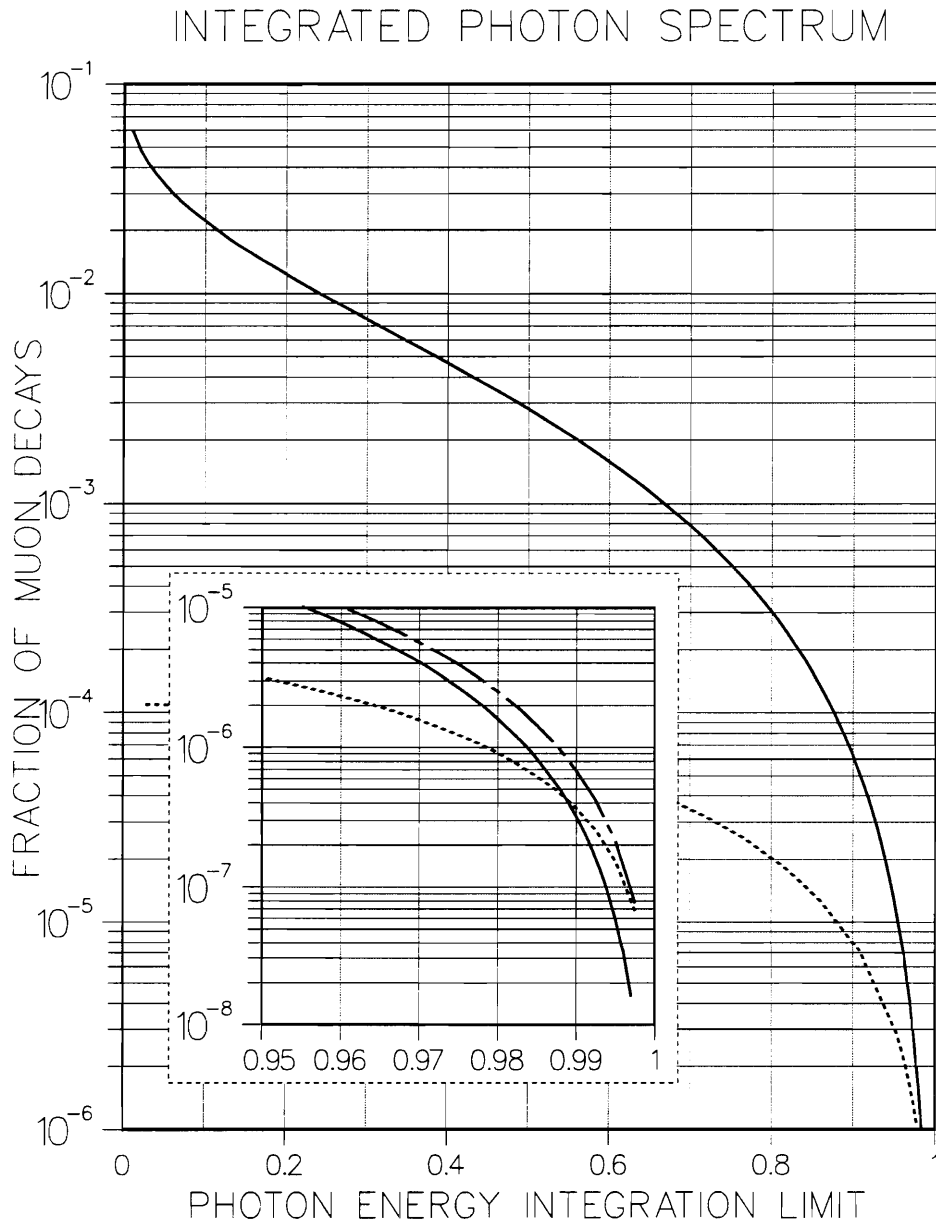


Figure 12: Integrated energy spectrum of photons from $\mu^+ \rightarrow e^+ \bar{\nu}_\mu \nu_e \gamma$ (solid curve), and positron annihilation-in-flight (dotted curve), and both (dot-dash curve in the set).

The detector resolutions determine the sizes of the cut windows, and therefore determine the overall background level of the experiment.

Table 4 lists the design goals of the MEGA experiment as well as the attained values of the Crystal Box and $\mu e\gamma$ -I experiments. The substantial improvements in detector resolutions and beam capacity were required for the MEGA experiment to achieve its goal of a $\mu \rightarrow e\gamma$ branching ratio sensitivity of a few parts in 10^{13} . The background and signal efficiencies for $\pm 2\sigma$ cuts on the measurable quantities are listed in Table 5. MEGA's goal is an essentially background-free measurement of the $\mu \rightarrow e\gamma$ branching ratio with a sensitivity inversely proportional to the running time T , in comparison with the background-limited Crystal Box experiment with a sensitivity proportional to $1/\sqrt{T}$ (See Fig. 13).

If the experiment sees no candidate events after all cuts have been applied, the branching ratio at 90% confidence limit would be limited to:

$$BR.(\mu \rightarrow e\gamma) \leq \frac{2.3}{N_\mu} \quad (90\% \text{ C.L.}) \quad (60)$$

Here, N_μ is the number of useful muon decays, given by:

$$\begin{aligned} N_\mu &= N_{stop} \times \frac{\Omega_{e\gamma}}{4\pi} \times \eta_{pair} \times \eta_e \times \eta_\gamma \times \eta_{cut} \\ &= \nu \times \varepsilon \times T \times \frac{\Omega_{e\gamma}}{4\pi} \times \eta_{pair} \times \eta_e \times \eta_\gamma \times \eta_{cut} \quad . \end{aligned} \quad (61)$$

The definitions and design values in equation (61) are listed in Table 6. The 53% fractional solid angle is limited by the pitch angle range of $10^\circ < |\lambda| < 45^\circ$ for both the positron and photon detectors. (Positrons with pitch angles below 10° are removed because their energy and direction are smeared by multiple looping and because part of the track may fall outside the time window imposed by the gate to the chambers' FASTBUS latches. Positrons with pitch angles above $\sim 45^\circ$ fall outside the acceptance of the positron scintillators.) The signal cut efficiency η_{cut} comes from Table 5. The goal for the ultimate branching ratio sensitivity was 5×10^{-13} for 140 days of running time (1.2×10^7 seconds), with only about 3 background events expected to survive all cuts. Assuming all observed events in the final data sample

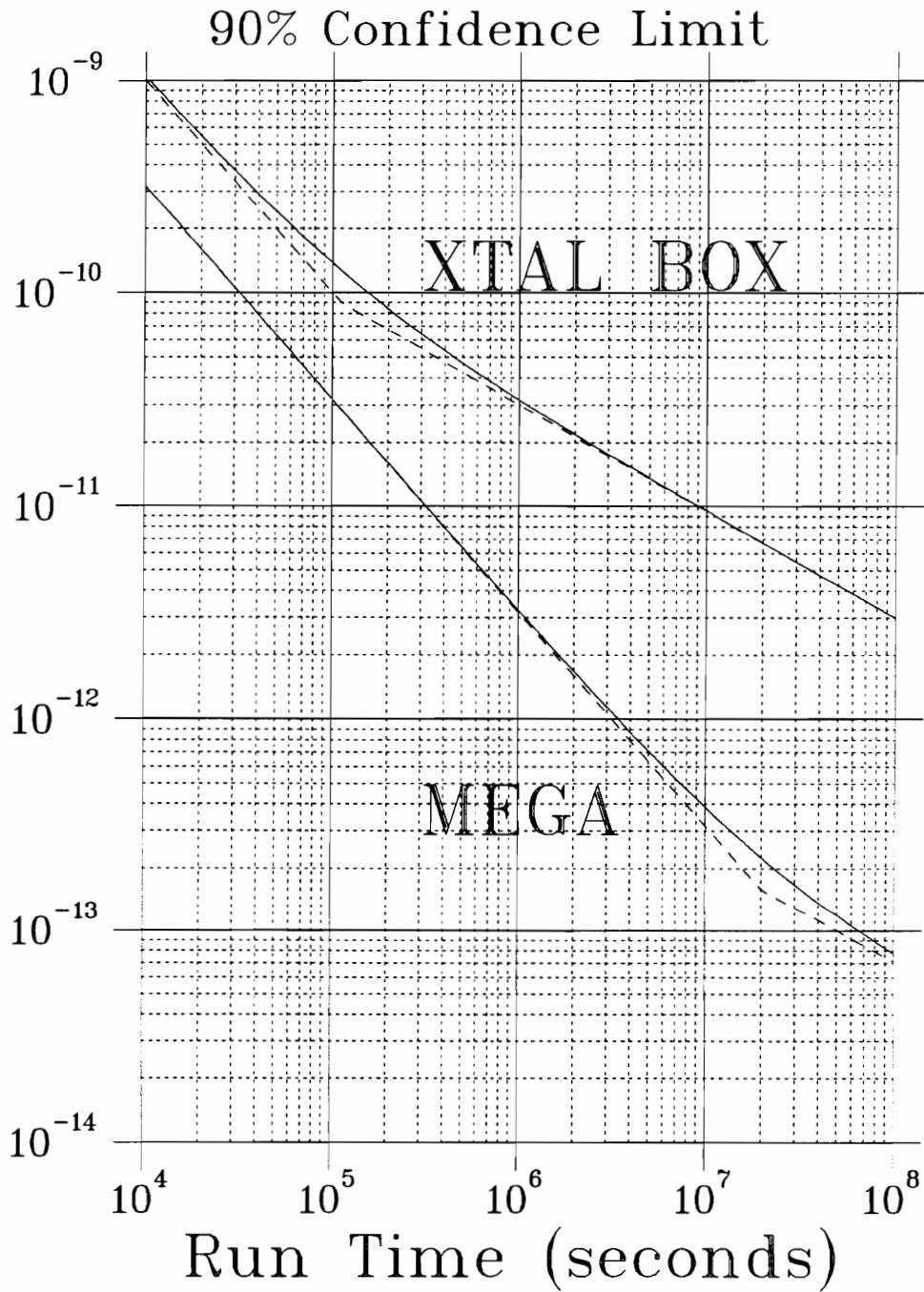


Figure 13: The comparison of the 90% confidence sensitivity as function of running time for MEGA and the Crystal Box experiment.

Table 4: Comparison of goals of MEGA with previous experiments.

Parameters	MEGA	Crystal Box	$\mu\epsilon\gamma$ I
E_e resolution	0.6%	8%	9%
E_γ resolution	2.5%	8%	8%
$\Delta t_{e\gamma}$ resolution	0.8 ns	1.1 ns	2.0 ns
e^+ position resolution at target	2.0mm	2.0mm	3.0mm
e^+ angular resolution including scattering in the target	0.6°	1.3°	1.3°
γ conversion point resolution	3mm	25mm	76mm
$\theta_{e\gamma}$ resolution	0.6°	8.0°	3.8°
γ direction	10°	—	—
IBV inefficiency	0.6	0.5	—
fractional solid angle \times detection eff.	3%	20%	1.8%
Note: All resolutions are quoted as FWHM			
avg. μ stop rate (MHz)	30	0.5	2.0
running time ($10^6 s$)	12	2	1.1
Branching ratio sensitivity	5×10^{-13}	4.9×10^{-11}	1.7×10^{-10}
Background events ($\pm 2\sigma$ cuts)	≈ 3	≈ 50	≈ 10

Table 5: Background and signal levels per muon decay in MEGA

parameter	cut ($\pm 2\sigma$)	background efficiency	$\mu \rightarrow e\gamma$ efficiency
$E_e(52.8MeV)$	± 0.0051	0.010	0.92
$E_\gamma(52.8MeV)$	± 0.021	2.5×10^{-6}	0.60
$\Delta\theta_{e\gamma}(^\circ)$	< 1.0	7.6×10^{-5}	0.80
$\phi_\gamma(^\circ)$	< 10	0.3	0.96
$\Delta t_{e\gamma}$ (ns)	± 0.68	0.68	0.97
IBV cut		0.6	0.97
		2.3×10^{-13}	0.40

are due to background, the 90% C.L. upper limit on the $\mu \rightarrow e\gamma$ branching ratio can be extracted by replacing the numerator 2.3 in equation (60) with a larger number (e.g., 4.0 for 3 observed events, and 6.7 for 6 observed events)[33].

3.3 Beam, Target and Magnet

In order to process enough muon decays, the MEGA experiment had to admit the maximum muon intensity of the LAMPF Stopped Muon Channel— $3 \times 10^7 \mu^+/\text{s}$. The typical beam entering the MEGA apparatus is roughly 5.0 cm in transverse radius with a purity of $\mu : e \geq 10 : 1$ (after removing positrons with an electrostatic separator). The layout of the Stopped Muon Channel (SMC) is shown in Fig. 14.

An 800 MeV proton beam impinges on the A2 target, producing pions. Some of the positive pions come to rest near the surface of A2 target and decay via $\pi^+ \rightarrow \mu^+ \nu$ (negative pions tend to be captured). These “surface muons” are roughly monoenergetic and fully polarized and are the most copious source available for MEGA

Table 6: Evaluation of number of useful muon stops.

factor	value	definition
ν	500 MHz	instantaneous muon stopping rate
ε	0.06	accelerator duty factor
T	1.2×10^7 s	total running time
N_{stop}	3.6×10^{14}	total number of muons stopped
$\Omega_{e\gamma}$	0.53	$\mu \rightarrow e\gamma$ fractional solid angle
η_{pair}	0.173	pair-conversion prob. \times trigger efficiency
η_e	0.95	$\mu \rightarrow e\gamma$ positron reconstruction efficiency
η_γ	0.60	$\mu \rightarrow e\gamma$ photon (pair) reconstruction efficiency
η_{cut}	0.40	cut efficiency (see Table 5)
N_μ	7.5×10^{12}	Number of useful muon decays
$\Gamma_{free}(90\%)$	5×10^{-13}	90% confidence branching ratio limit

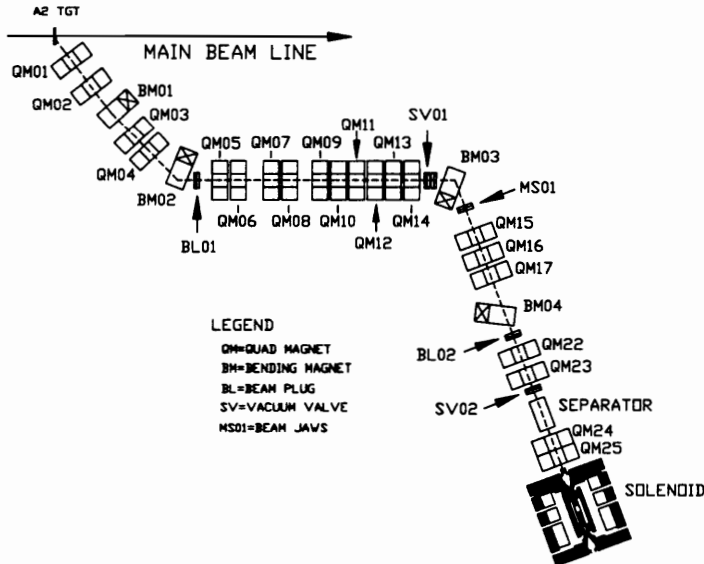


Figure 14: Stopped Muon Beam line at LAMPF

experiment. The SMC is tuned to deliver a 28.5 MeV/c beam of roughly 3 cm transverse radius to the MEGA apparatus, with a $\mu : e$ ratio of 1:10. (The positrons arise predominantly from pion and muon decays before *QM01*). Most of the positrons are removed from the beam before it enters MEGA by an $\vec{E} \times \vec{B}$ velocity selector between *QM23* and *QM24* that is tuned to pass the $\beta_\mu = 0.26$ muons but sweep out the $\beta_e = 0.9998$ positrons. This separator employs a 200 kV electron field and a crossed 1 kG magnetic field. The muon to positron ratio after separation is 10:1.

After passing through a 5 mil aluminum and 1 mil mylar vacuum window at the end of the SMC beam line, the muons are further slowed by their passage through a 16.5 mil mylar degrader and 66 cm of helium before coming to rest in a 3 mil mylar target. This target is tilted at a steep angle relative to the beam axis (79°) so that its effective thickness for muons appears to be $3 \text{ mil} / \cos 79^\circ = 15.7 \text{ mil}$. (This places the muon range within the stopping target; we estimate that $\sim 75\%$ of the muons stop within this target thickness in the absence of a hole.) The target is cut into the shape of an ellipse and mounted in a 5cm radius, 66cm long and 0.5 mil thick cylindrical “target bag” aligned on the beam axis. The target bag is inflated with helium at 30 torr of overpressure to maintain its cylindrical shape (and thereby the target’s planar shape). A survey found that the target normal was at an azimuthal orientation of 166° counterclockwise from the x axis (horizontal). Note that this canted target orientation also presents very little material to scatter or degrade the exiting positrons of interest to us ($10^\circ < |\lambda| < 45^\circ$). A vertical target 15.7 mil muon stopping target would have placed five times more target material in the positron path. The slanted target also aids in the photon traceback’s rejection of random positron-photon coincidences by spreading out the muon decay points over a large area.

A GEANT[34] Monte Carlo showed that if the helium in the target bag was contaminated with few percent air, it would cause 20% of the beam to stop upstream of the target. We checked for the absence of air by verifying that the target bag held its overpressure (i.e., no leaks), and by designing the inlet and outlet so that heavy gases would be purged easily during flushing and filling with helium. The outlet gas was checked for the absence of contaminants.

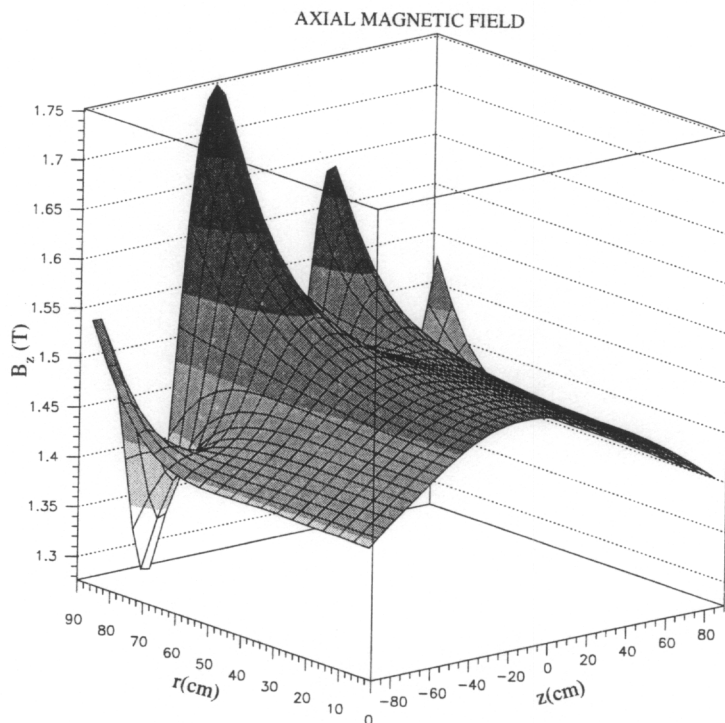


Figure 15: Field strength vs position.

The magnet used for MEGA experiment is a large bore, segmented coil superconducting solenoid, working at $4^\circ K$. (This magnet was previously used in the LASS experiment at SLAC.) It produces a 15 kG field in the central region at the full current of the power supply. The clear bore is 2.89m long and 1.85m in diameter. A field map, compiled from an extensive hall probe survey, shows only 3% variation along its axis in both the positron and photon detector volumes (see Fig. 15). Table 7 lists all the magnet parameters[35].

3.4 Photon Pair-Spectrometer

The photon detector is composed of three concentric pair spectrometer layers that operate independently. Each pair spectrometer consists of five major components: (a) photon converter layers, (b) plastic scintillators (c) MWPCs, (d) drift chambers, and (e) degrader. The two inner pair spectrometers each have three drift layers, while the third spectrometer has four drift layers (built after having had operating experience

Table 7: Parameters of the MEGA magnet

clear bore diameter	1.85 m
total length (with iron yoke)	4.06 m
clear bore length	2.89 m
central field	1.5 T
operating current	1118 A
total inductance	14 H
total liquid He volume	3950 ℓ
fill and cool down time	30 days
charging time	20 min
total weight of iron	180 tons
winding configuration	pancake
conductor type	cryostatically stabilized composite, multifilament wires
conductor Cu-to- Nb _x Ti ratio	20:1
conductor current density	~ 4000 A/cm ²
conductor length	~ 29 km
conductor weight	~ 10000 kg

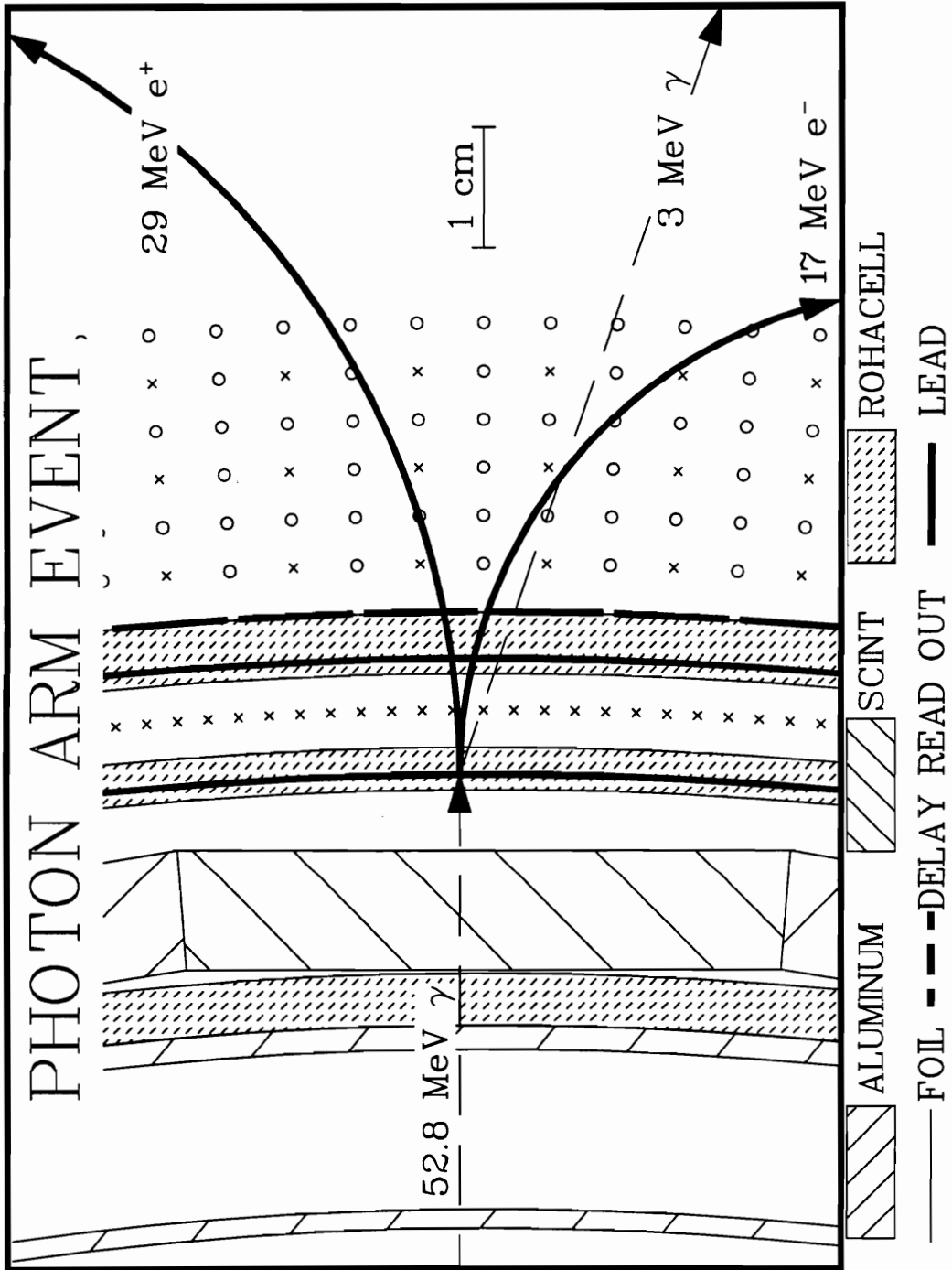


Figure 16: Cross sectional view of one layer of a typical photon conversion

with the first two). Each anode of the innermost drift chamber is instrumented a coaxial cathode delay line that measures the z coordinate of the avalanche at the anode.

The photon detector measures the energy and time of photons and supplies the signals for the $\mu \rightarrow e\gamma$ hardware trigger (“GHIGH”). The operation of one layer of pair spectrometers is illustrated in Fig. 16, where a photon converts into an e^+e^- pair in the inner lead sheet. The pair’s helices diverge and fire the MWPC, indicating that this particular conversion happened in the inner lead sheet. The three layers of drift chambers track the orbiting e^+e^- pair and determine their momenta from the first half loop. Finally, the plastic scintillators register the times at which the pair first passes through.

The mildly energetic photons striking the pair spectrometers are predominantly from the radiative muon decay $\mu \rightarrow e\gamma\nu\bar{\nu}$. (The photon scintillator thresholds are set high enough to be insensitive to the abundance of 511 keV annihilation photons within the apparatus.) Compared with normal muon decay $\mu \rightarrow e\nu\bar{\nu}$, the matrix element of the former process is two orders of magnitude smaller ($\alpha \sim 1/137$). Coupled with the low conversion probability of the photon detector itself, the pair spectrometer components operate at a relatively low rate compared to the muon stopping rate. Thus, the pair spectrometer scintillators and MWPCs provide fast, nearly deadtimeless information for the first stage of the GHIGH trigger, while the associated drift chambers provide slower information for the second stage of this trigger.

Since the photon detector operated at a sufficiently low rate, the readout cost could be reduced dramatically by multiplexing several signals into one FASTBUS channel. From Table 8, three layers of spectrometer would require more than 7500 unmultiplexed TDC channels (over \$1.2 million at \$150.0/channel). With multiplexing by quadrant in pair spectrometer 1 and 2 and by octant in number 3, the readout cost was reduced by an overall factor of 5.4. The quadrant (or octant) in which a photon converted was encoded by storing the unmultiplexed photon scintillator hits in an “enable latch.”

	Layer 1	Layer 2	Layer 3
scintillator info:			
number:	40	60	80
thickness:	1.000	1.000	1.000
mean radius:	32.500	48.448	63.869
inner Pb-conversion:			
mean radius:	33.719	49.667	65.088
thickness:	0.0254	0.0254	0.0254
outer Pb-conversion:			
mean radius:	34.699	50.648	66.069
thickness:	0.0254	0.0254	0.0254
MWPC layer:			
number of channels:	416	640	832
number of wires:	832	1280	1664
wire radius:	34.173	50.121	65.542
halfgap:	0.293	0.293	0.293
drift chambers:			
channels per layer:	208	320	416
delay line info:			
inner circum.:	219.497	319.701	416.594
width:	1.0553	.9991	1.0014
radius:	34.934	50.882	66.303
DC 1:			
sense wire radius:	35.334	51.282	66.703
cell diameter:	0.800	0.800	0.800
DC 2:			
sense wire radius:	36.134	52.082	67.503
cell diameter:	0.800	0.800	0.800
DC 3:			
sense wire radius:	36.934	52.882	68.303
cell diameter:	0.800	0.800	0.800
DC 4:			
sense wire radius:	-	-	71.103
cell diameter:	-	-	0.800

All dimensions are in centimeters unless otherwise indicated

Table 8: Summary of photon arm geometrical parameters

3.4.1 Converter

The lead sheets in the photon spectrometer convert a 52.8 MeV photon to a e^+e^- pair whose momentum can then be measured with higher accuracy than would be possible with a calorimetric measurement of the photon's energy.

Lead, being a high Z material, has a large pair production cross section, but only a modest cross section for Compton scattering or photoelectric absorption.

The optimal thickness is a compromise between the desire for high pair production probability and the need to minimize scattering and degradation by bremsstrahlung and ionization of the resultant pair in the lead sheet. The solid curve of Fig. 17 shows the pair production probability as a function of the lead converter thickness. The dotted line shows the probability that the resultant pair leaves the outer sheet with an energy loss of 2.0 MeV or less. The dashed line is the product of these two curves and gives the “useful” conversion efficiency for a 52.8 MeV photon as a function of lead thickness. From Fig. 17, the optimal thickness of the converter should be $0.2X_0$ (0.112 cm), with useful a conversion efficiency 0.034. However, we chose a more conservative thickness of $0.09X_0$ (0.0508 cm), with a useful efficiency of 0.029, to achieve a better photon energy resolution. In fact, the lead converter was segmented into two 10 mil (0.0254 cm) sheets separated by an MWPC to distinguish between conversions in the inner and outer sheet. This strategy gave us a better energy resolution for half of the conversions and slightly worse energy resolution for the remainder; the combined uncertainty in the pair's energy loss was a factor of three better than what would have been achieved with a single 20 mil lead sheet. With this thickness, the total pair production probability in one pair spectrometer was 4.325% for a 52.8 MeV photon. Three layers of pair spectrometer had a total pair production probability of 12.75%, with a photon energy resolution better than 2.5%.

3.4.2 Photon Spectrometer Scintillators

The scintillators in the photon spectrometer measure the photon time (as the e^+e^- pair passes through) and provide the inputs for the MEGA trigger. Each scintillator barrel is segmented axially into $5\text{cm} \times 1\text{cm} \times 180\text{cm}$, staves with the 1 cm edges tapered

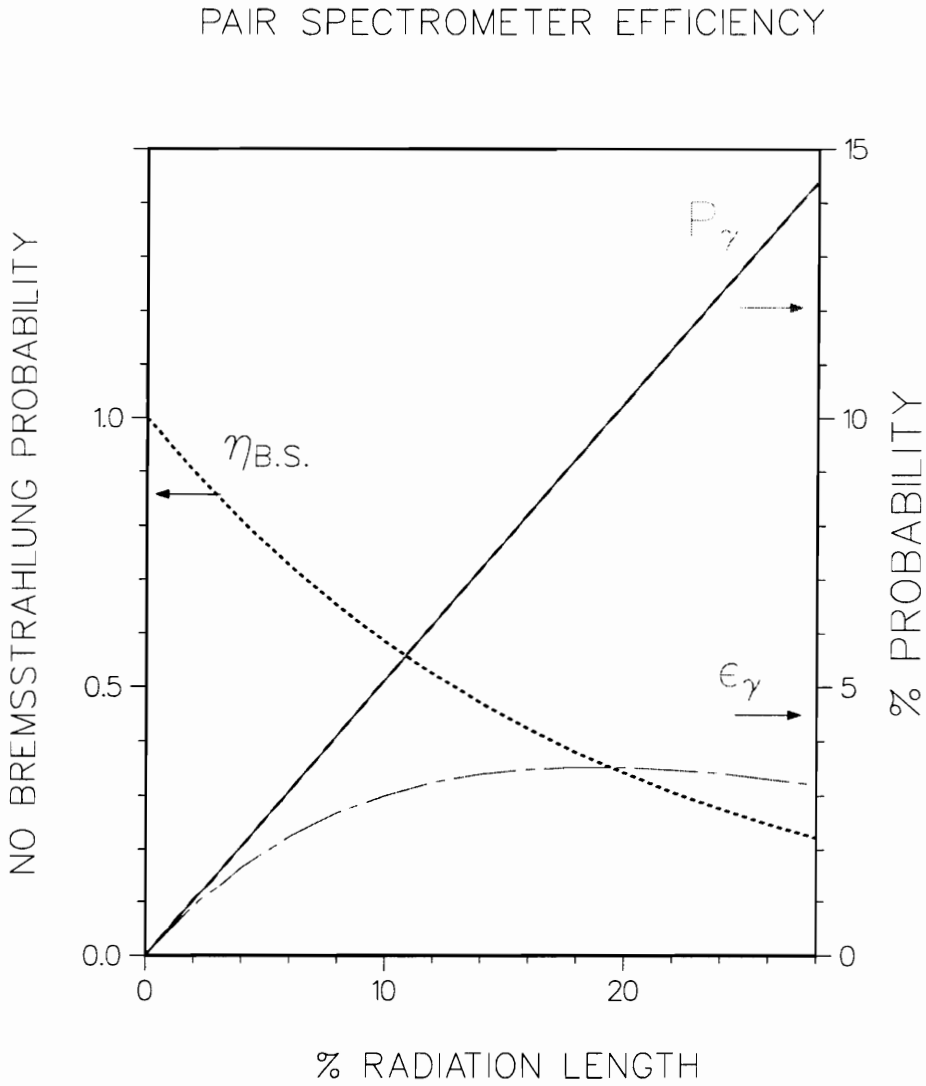


Figure 17: Plot of probability of pair-production (solid), pair *survival* probability (dotted), and net conversion efficiency (dashed) versus converter thickness, for 52.8 MeV photons

by 4.5° to avoid cracks in the barrel. The width segmentation guarantees independent timing measurement for both e^+ and e^- , and provide a comfortably broad azimuthal spread in scintillator hits to the trigger logic so that it can discriminate against lower energy photons by this breadth. The variations due to light propagation delays along the 180 cm were avoided by installing PMTs on both ends of each scintillator, then feeding the signals from both ends to a TDC (for a software calculated meantime), and to a fast meantimer module that provide the trigger signals.

As the photon's e^+e^- pair spirals repeatedly, the PMTs connected with scintillator will see multiple hits quite often, distorting the pulse shape and amplitude. Constant-fraction discriminators (CFDs) are employed to avoid timing jitter associated with such overlapping pulses.

In addition, each scintillator PMT is instrumented with an ADC to permit the offline analysis software to implement a walk correction to the measured times.

Table 9 shows the parameters of the photon scintillator system. All of the PMTs were installed two meters from the solenoid's axis (outside the return yoke) in $1/2''$ thick soft iron pipes, and were coupled to scintillators through three meter long light guides. The residual field in each phototube was less than one gauss[36, 37].

3.4.3 The Photon Spectrometer MWPC

The photon spectrometer MWPC served three purposes: distinguishing between photon conversions in the inner and outer lead layers, providing fast signals to the MEGA trigger, and locating the vertex of a given photon conversion.

Knowing in which lead sheet the photon converted, we can make a more accurate correction for the photon pair's energy loss. The latched MWPC information provides us with this knowledge. The MWPC hits are latched by two independent schemes: (1) four adjacent wires are ganged into a cluster whose combined signal is latched but not multiplexed ("cluster latch"), (2) four wires, one from each quadrant (each octant in pair spectrometer 3), are multiplexed into one latch channel ("multiplex latch"). The trigger uses the clustered MWPC signals to look for a high energy photon; this granularity is about twice as fine as the photon scintillator segmentation. The offline

Table 9: Parameters of the photon scintillator system.

scintillator	
material	Bicron BC-412
peak of emission spectrum	434 nm
light output	60% anthracene
bulk attenuation length	400 cm
rise time	1.0 ns
decay time	3.3 ns
index of refraction	1.58
phototube	
model	Hamamatsu R1355
diameter	2.8 cm
spectral response	300-650 nm (peak at 420 nm)
anode pulse rise-time	2.0 ns
electron transit time	23 ns
fiber-optic light guides	
model	Mitsubishi Rayon EK80
unit length	3 m
fiber diameter	2 mm
acceptance cone	31° half-angle
core material	polymethylmethacrylate
core refr. index	1.495
cladding material	fluorinated polymer
cladding thickness	21 μm
attenuation	<0.25 dB/m at 434 nm
average number of photons	
seen at each tube	20 - 30
efficiency of system	>98%

Table 10: Photon arm MWPC parameters

chamber length	177 cm
wire type	1 mil Au-W
wire tension	100 grams
wire spacing	5 mm
half gap	3.5 mm
chamber gas	CF ₄ (57%)+C ₄ H ₁₀ (43%)
or:	CH ₄ (67%) +C ₄ H ₁₀ (17%)+Ar(16%)

software uses the multiplexed MWPC signals to locate the conversion vertex with 5 mm resolution. The parameters of the photon spectrometer MWPC are listed in Table 10.

3.4.4 Photon Spectrometer Drift Chamber

The photon spectrometer drift chamber tracks the converted e^+e^- pair and measures the momenta of this pair. The incident photon's energy, conversion point, and direction can be extracted from the reconstructed e^+e^- pair. This apparatus consists of three drift layers of sense and field wires and a delay line cathode layer below the anodes of first drift layer. These drift cells form a locally rectangular grid as shown in Fig. 16. According to a Monte Carlo study, this arrangement is superior to a staggered cell geometry in resolving left-right ambiguities for a pair of helical tracks[38].

The sense wires are held at 2150V; the field wires at the cell edge are grounded; and the field wire at the cell corners are held at -150V to better symmetrize the field in the cell. In order to achieve high efficiency for the delay line, the cell size was chosen to give a large gas gain and therefore a large pulse—in particular, for DC1, a large image charge on the delay line cathodes that are used for the z coordinate measurement.

The circular x - y projections of tracks are fitted by using the drift times and fired cell locations. From the radii of these circles, we can calculate the energies of the converted e^+e^- pair and hence find the transverse momentum of the candidate photon.

The 15 kG solenoidal field parallel to the sense wires cause the ionization electrons in the drift cell to follow a longer curved trajectory toward the sense wires. With the field on, the maximum drift time is roughly 350 ns and the position resolution is 250 μm (FWHM). The pair's longitudinal momenta and the photon conversion point's axial position are determined from the z coordinates of the hits in DC1, measured by the difference in propagation times of signals to upstream and downstream ends of the cathode delay lines.

Each DC1 drift cell has its own 177 cm long delay line fabricated from 1.34 mil copper on both sides of a 3 mil thick kapton substrate and photo-etched on both sides to form a square-wave pattern with a 1 mm repeat distance. The pattern on opposite sides of the kapton are phase shifted by half a cycle. (The effective length of the delay line is increased by a factor of 19 by this technique.) The axial propagation speed is 13 cm/ns and the maximum time difference is about 250 ns.

The parameters of the drift chambers are summarized in Table 11.

3.5 The Positron Spectrometer

The positron spectrometer is the most challenging part of the MEGA apparatus since it has to operate in a very high rate environment as well as give high precision measurements for both momentum and time of positrons. The high positron flux can degrade the chamber performance (reduced efficiency due to space charge buildup) and potentially cause permanent damage (hydrocarbon polymerization on the anodes and/or cathodes). Also, a large number of overlapping track segments in one event will cause difficulty for the software pattern recognition code.

Fig. 18 shows the cross sectional view of the positron spectrometer. The chambers are arranged so that seven “dwarf” chambers surround the large “Snow White”

Table 11: Parameters of the photon arm drift chambers.

cell width	10 mm
cell height	8 mm
length of chamber	177 cm
chamber gas	Ar(57%)+C ₂ H ₆ (43%)
field wire	
material	4 mil Cu-Be
tension	250 grams
voltage	corners: -150 V sides: grounded
sense wire	
material	1.3 mil Au-W (1.0 mil for DC1)
tension	200 gm (100 gm for DC1)
voltage	~ +2150 V

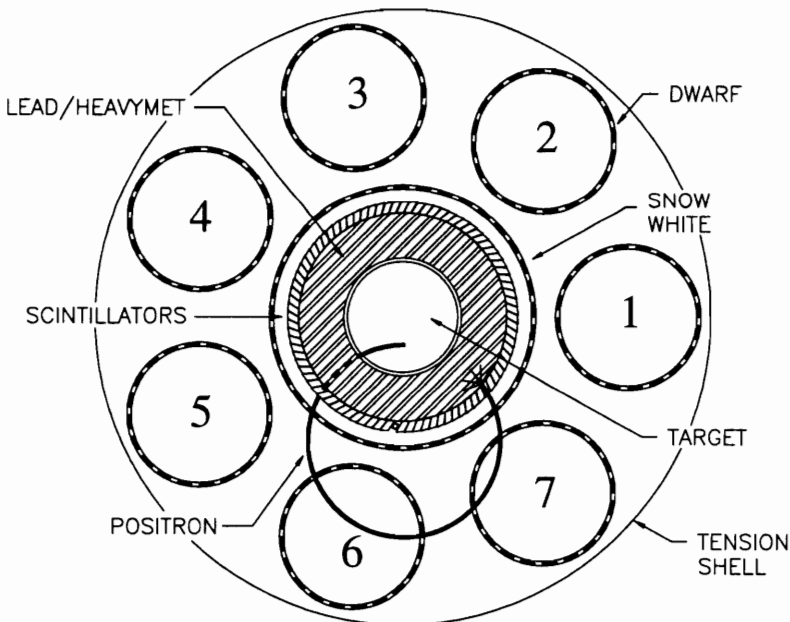


Figure 18: End view of positron spectrometer, looking upstream.

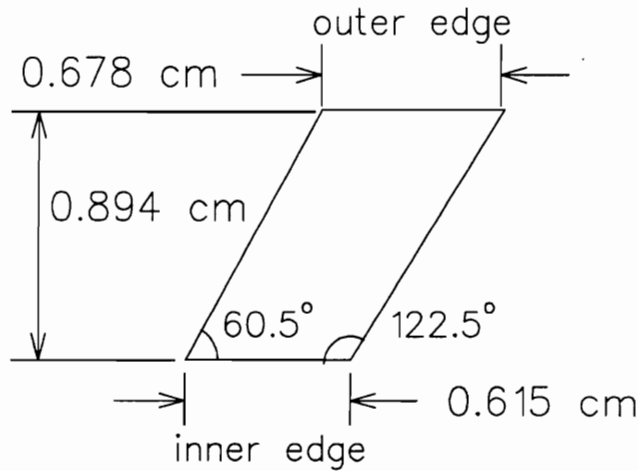


Figure 19: Cross section of a positron scintillator, looking upstream

chamber that is coaxial with the magnetic field axis. The two 33cm long scintillator barrels each are segmented azimuthally into 88 sections to reduce the occupancy caused by the high positron flux. A gas line for the target bag inlet (outlet) occupies one of these sections at the upstream (downstream) end.

As depicted in Fig. 18, a muon beam enters along the axis of the solenoid, stops in the MEGA slanted target and decays at rest via $\mu^+ \rightarrow e^+ \nu \bar{\nu}$ (Michel decay). The positron traverses a helical path under the influence of the magnetic field. It leaves the target, registers entrance and exit hits in 1–3 of the seven dwarfs as well as in Snow White, and finally penetrates a scintillator to register the time before showering in the lead pipe.

The geometrical parameters of the positron spectrometer, both MWPCs and scintillators, are summarized in Table 12.

3.5.1 The Positron Spectrometer Scintillators

The positron scintillators measure the positron time with a resolution of about 600 ps (FWHM). Fig. 19 shows the cross section of one positron scintillator bar. The shape is designed to reduce the probability that a spiraling positron track crosses two neighbor scintillators. The scintillators are individually wrapped in 1/4 mil aluminum foil for optical isolation, and the sides of each bar are tapered by 2° so that they can

Table 12: Geometric configuration of the positron arm

scintillators:	
no. of bars per end	88 (1 removed for gas line)
inner shell radius	8.842 cm
outer shell radius	9.736 cm
z coverage	$\pm[33-63]$ cm
MWPCs:	
chamber length	126 cm
chamber radius	11.138 cm (Snow White)
	5.982 cm (dwarfs)
radial offset of	
dwarf chamber centers	19.126 cm
ϕ position of	
center of dwarf N	$(N - 1)/7 \times 360^\circ$
wire type	15 μm Au-W
wire spacing	1.305 mm (Snow White)
half gap	1.778 mm
cathode foil	Cu(200 nm)+kapton(25 μm)
cathode stripe width	2.7 mm (Snow White)
	2.8 mm (dwarfs)
cathode stereo angle	29.05° (Snow White)
	16.61° (dwarfs)
chamber gas	CF ₄ (80%)+C ₄ H ₁₀ (20%)+H ₂ O(0.2%)

be closely packed into the cylindrical barrels.

The end of each scintillator that is furthest from the center of magnet is instrumented, while the near end is blackened to avoid reflected light. Because of the high magnetic field, all of the phototubes are mounted in a soft iron box outside the end-caps of the magnetic yoke, and are coupled to the scintillators through fiber-optic light guides.

The PMT signals are split in amplifier-discriminator modules (scavenged from the Crystal Box experiment), with the discriminated pulse going to a pair of TDCs and the analog pulse going to a pair of ADCs. The two TDCs and ADCs per scintillator alternate in digitizing the hits from successive events to avoid excessive readout deadtime from the $\sim 7\mu s$ ADC/TDC conversion time. The pair of TDC (or ADC) modules per scintillator are labelled “EVEN” and “ODD” since they alternate in digitizing the event stream.

3.5.2 Positron Spectrometer MWPCs

Due to the requirements that the MWPCs operate with very high rate flux ($\sim 3 \times 10^4 e^+ / mm^2 / s$) while providing very high precision measurements of positron momentum, the design and construction of these chambers is the most technically challenging aspect of the MEGA detector system. (Note that drift chambers, although having better positron resolution, are far too slow for this environment.)

Fig. 20 shows a schematic drawing of a dwarf chamber. Each 126 cm long cylindrical MWPCs has a layer of axial anode wires sandwiched between two opposite-pitch stereo cathode foils. The anode cylinder radius is 6 cm for the dwarfs and 11 cm for Snow White. The anodes are 15 μm diameter gold plated tungsten with 1.305 mm pitch; the anode-cathode gap 1.778 mm. The cathode foils are made of 25 μm thick Kapton with 200 nm thick copper vapor-deposited on one side. The copper is scribed into 3 mm wide stripes using a large Hewlett Packard drafting plotter. The cathode stereo angle is $\pm 60^\circ$; each cathode makes one complete revolution over the length of the chamber. The dwarf cathodes are split in the midplane (i.e., at $z = 0$) to halve their occupancy. This strategy is not effective enough for Snow White; in this case,

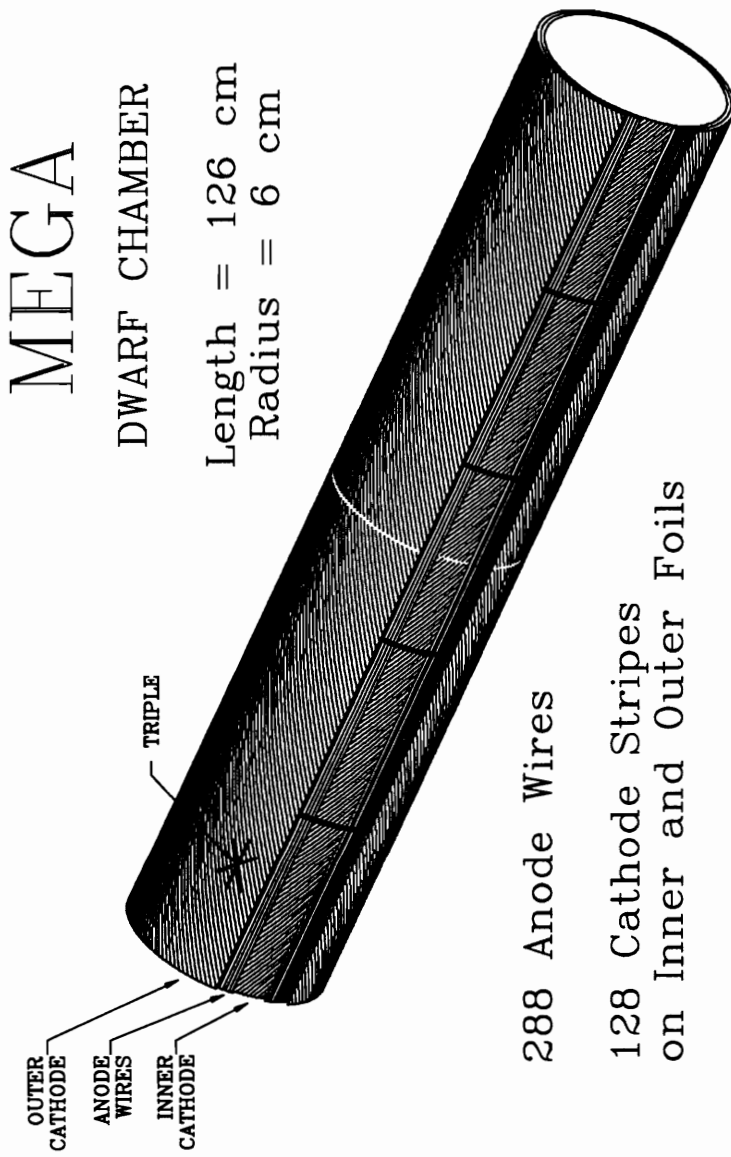


Figure 20: Schematic drawing of a dwarf chamber

the central region of $|z| < 33$ cm has no cathode strip readout at all.

To prevent the electrostatic deflection of the anode wires toward the cathode foils, a set of supporting garland rings are placed equidistant along the length of the chamber. There are four garlands in each dwarf, but only three in Snow White. (At 2150V, the electrostatic instability sets in for unsupported lengths greater than 36cm.) These garlands consist of 0.66 mm thick annealed glass-fiber rings between the anode wires and inner cathode foil suspended on 6 glass beads, and nylon mono-filaments tied around the outside of the wires (with small droplet of epoxy).

The working gas is a mixture of 80% CF_4 and 20% isobutane with a small amount of water (0.2%) to quench the dark current. The fast drift speed of this gas ($12\text{cm}/\mu\text{s}$) and the small MWPC cell size ($\sim 1.8\text{mm}$ half gap) imply a very small signal collection time ($\sim 15\text{ns}$), which means that we can reduce the pileup probability of two uncorrelated tracks' signals on a given anode or cathode by using a very narrow latch gate (25ns, with the extra 10ns to account for the spread in the arrival time of throughgoing multiple-looping positrons.)

The MWPC are built with very low mass—to minimize the multiple-scattering and energy loss contributions to the positron's momentum resolutions and the probability of positron annihilation in flight resulting a high-energy background photon. The normal thickness of the chamber (two cathode foils, gas and anode wire) is about 3×10^{-4} radiation length. Note that there is no other material in the chamber associated with any support structure. The anode tension is held by the end plates and cathode foils are supported by differential gas pressure, somewhat like inflated cylindrical balloons.

The momentum determination of a positron is obtained from the track parameters of the reconstructed helix that passes through the latched chamber hits. The location of the hit anode wires will give a group of (x, y) coordinates. The circular projection of the helix onto the x - y plane is fitted by using the anode hits; the radius of this circle gives the transverse momentum. The crossing point of these hit anode wires with both inner and outer spiral cathodes, called “triples,” give a z coordinate for each hit. The fit to these side view hits determines the longitudinal-to-transverse momentum ratio. Combined with the end view fit, we get the total momentum of

the positron.

In the high rate environment, an anode-cathode crossing (a “double”) doesn’t provide any redundancy to guard against imaginary hit points. Therefore, we always demand an anode—inner cathode—outer cathode crossing (a “triple”). Even then, the occupancy is high enough that random coincidences produce some ghost triples. Without some care, the offline analysis would be confused by these imaginary hits, perhaps failing to reconstruct, misreconstructing the helix, or, in the extreme case, reconstructing a fake track. Beyond the methods already mentioned to reduce the chamber occupancy (small cells, split cathodes, omission of cathode strips in the Snow White central region), we can restrict the areas in the chambers where we look for hits by using the information from the reconstructed photon to project a “52.8 MeV e^+ road” back through the positron MWPCs and then accepting hits only if they appear within this road.

All of the MWPCs are installed in an aluminum drum, called the tension shell (see Fig. 18). The wire tension is maintained by locking the chamber end assembly on the endcaps of the tension shell. Two neoprene ring bladders, initially deflated, also are installed on both ends of chamber. After all eight chambers are transferred into the tension shell, the bladders are inflated to isolate the tension shell volume so that it can be filled with helium.

3.6 Trigger and Data Acquisition Systems

3.6.1 MEGA Trigger System

In our experiment, we want to select events that are reasonable candidates to be $\mu \rightarrow e\gamma$ decays. The trigger is responsible for selecting these candidates out of the stream of uninteresting muon decays. It relies on the signals from the photon spectrometer, since this gives an automatic purification factor of 100 ($\sim 1/\alpha$) from the matrix element for radiative muon decays and another factor of 8 from the inverse of the photon conversion probability. The first stage trigger looks for patterns of scintillator and MWPC hits indicative of the conversion of a photon having transverse

momentum of $\sim 35\text{MeV}/c$ or more. If this selection criterion is satisfied, a fast strobe is generated that starts the TDCs and opens the gates for the ADCs and latches. Meanwhile, the second stage trigger searches for a pattern resembling two joined circles from the later-arriving signals of the photon spectrometer drift chambers. If such a pattern is not found, a fast clear signal is generated that aborts the TDC and ADC digitizations and clears the latches. (This fast clear resets the readout modules so that they are ready to accept a new event immediately, without having to wait for the $7\mu\text{s}$ digitization cycle to complete.)

The first stage of this so called “GHIGH” trigger is only one of several photon spectrometer related triggers incorporated into the MEGA trigger module known as the “Chicago Box.”

The Chicago Box consists of a set of programmable array logic (PAL) chips that are encoded to perform the fast pattern recognition of the photon spectrometer hit information. There are three categories of PALs: M modules, S modules and T modules. The M modules receive the signals from the photon MWPC clusters (four adjacent wires per cluster) and turn on their output logic signal if at least three clusters fire in a span of between 9 and 13 contiguous clusters. The minimum width of nine clusters selects e^+e^- pairs with a transverse momentum greater than about $32\text{ MeV}/c$. The S modules examine the scintillator meantimer hits and turn on their output signal if they find a pattern of at least three non-adjacent scintillator hits with a span of between four and six scintillators wide. Finally, the T modules map the azimuthal overlap of the outputs of the M modules and S modules and generate a trigger signal if an overlap is found. The total decision delay of the Chicago Box is 18 ns , subject to $\pm 3\text{ ns}$ jitter. It operates in a deadtimeless manner.

The Second Stage Trigger module (SST) is composed of CMOS Erasable Programmable Logic Device (EPLD) chips. Its purpose is to veto spurious first stage triggers that are generated by random coincidences or by “hot” MWPC wires. The SST uses the independent signals from the photon spectrometer drift chambers.

The “Routing Box” module is used to handle the controls and synchronization of the triggers, FASTBUS modules and the computer processor farm. It responds to the trigger signals from the Chicago Box and distributes them to the appropriate

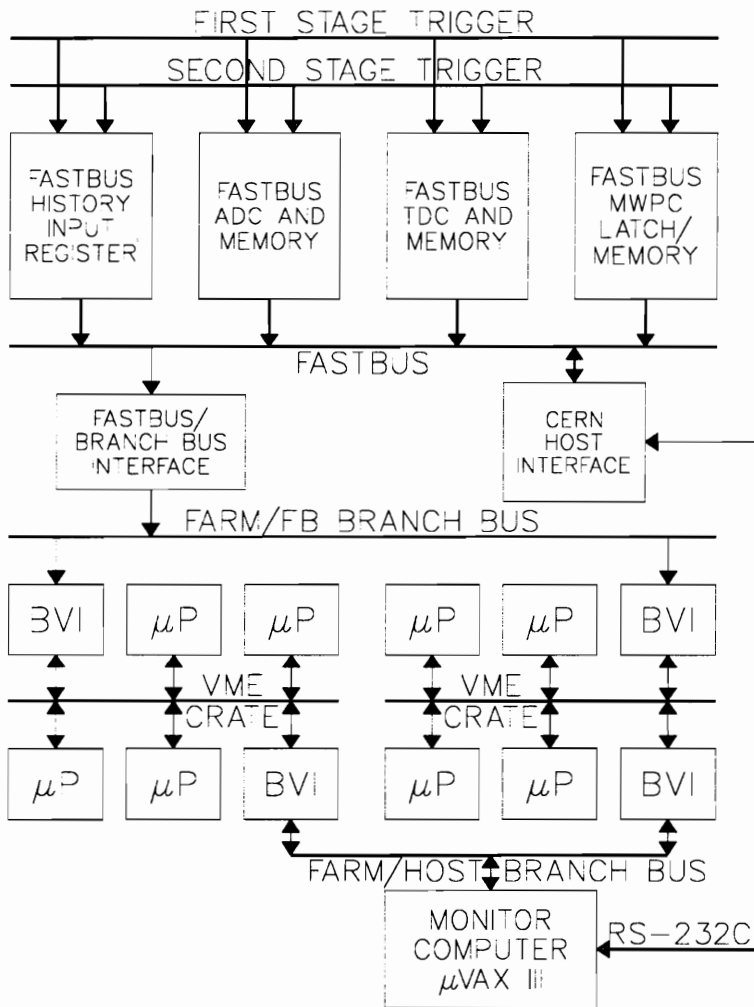


Figure 21: MEGA data acquisition system

Trigger	Typical function
Pulser	Electronics readout testing
PScinUp*PScinDn	Cosmic data
Ring Counter	Timing calibration
PScin <i>i</i> *Ring Counter	Timing calibration, enriched
Positron Scintillator (EScin)	$\mu \rightarrow e\nu\bar{\nu}$ data
Inner Bremsstrahlung Veto (IBV)	$\mu \rightarrow e\gamma\nu\bar{\nu}$ data (not used)
Photon Scintillator (PScin <i>i</i>)	Field-off $\mu \rightarrow e\nu\bar{\nu}$ data
Glow <i>i</i>	$\mu \rightarrow e\gamma\nu\bar{\nu}$ data
Ghigh <i>i</i> *EScin	$\mu \rightarrow e\gamma\nu\bar{\nu}$ data, enriched
Ghigh1*GHigh2	$\pi^0 \rightarrow \gamma\gamma$ data
Ghigh <i>i</i>	$\mu \rightarrow e\gamma$ data

Table 13: The list of triggers available in 1992 Runs. Here $i \in \{1, 2\}$ denotes the photon layer.

readout modules; processes the BUSY signals from FASTBUS; controls the second stage trigger; synchronizes its output to various external signals as appropriate (such as the LAMPF beam gate) and send several diagnostic signals to scalers so that the trigger rates and data acquisition deadtimes can be monitored. The Routing Box is the control module that the experimenter manipulates through computer commands to select the desired trigger and running conditions. Fig. 21 shows the flow chart of the MEGA trigger and data acquisition system.

The other triggers available to the experiment for physics and for detector setup and testing are listed in Table 13.

3.6.2 Data Acquisition System

The data acquisition system uses FASTBUS latches, TDCs and ADCs for the readout elements, under the control a CERN Host Interface (CHI)[39]. The choice of

FASTBUS over CAMAC or NIM reflects the high rates expected in the experiment, as well as the large number of channels to be read out. The multiple-buffering feature of the Phillips Scientific FASTBUS modules (up to 32 events in each module) is well matched to the LAMPF beam structure of 80–120 Hz with 600 μ s wide pulses. At full muon intensity, each such macropulse generates about 10 to 20 GHIGH triggers. The data is stored in the modules until the end the macropulse, at which time it is transferred by the CHI to an available workstation in the online farm. This transfer is implemented by first converting the signals from FASTBUS to a “Branch Bus” [40] and then from the Branch Bus to one of two VME buses, and from there into the workstation. Table 14 summarizes the peak data flow during the $\mu \rightarrow e\gamma$ running. (The 1992 data rate was lower because of a reduced muon stopping rate, only two photon spectrometer layers, and the availability of only four DECstation 5000/200 processors instead of the final complement of eight DECstation 5000/240 units.) The peak 3 Mbytes/s data rate into the workstations is very close to the bandwidth of the intervening buses, when all level transfer delays are included. Furthermore, the readout time for all of the events from one macropulse comes very close to saturating the available quiescent time between macropulse. If this readout time extends into the next macropulse, that macropulse is lost—effectively doubling the deadtime and halving the $\mu \rightarrow e\gamma$ branching ratio sensitivity. Clearly, the data acquisition system has been finely tuned to take maximum advantage of the available muon beam at LAMPF.

3.6.3 Online Filter

Most of the triggered events are not suitable candidates of the $\mu \rightarrow e\gamma$ decay process—they typically contain the triggering high energy photon and the partial segments of several uncorrelated Michel decay positrons. The online filter code selects only those events that look reasonably like $\mu \rightarrow e\gamma$ for taping. (In 1992, the online filter code also performed the veto duty of second stage trigger in software, since the hardware module was not available.)

The on-line photon filter code (“online PAIRS”) makes a rough reconstruction

Table 14: Estimation of the *design* peak raw $\mu \rightarrow e\gamma$ data rate.

Average event size:		(bytes)
positron MWPC latches		1000
positron scintillator TDCs		40
positron scintillator ADCs		40
internal brem. veto TDCs		20
photon scintillator TDCs		20
photon scintillator ADCs		20
photon scintillator latches		40
photon MWPC latches		120
drift chamber anode TDCs		60
delay line cathode TDCs		20
history latch module		20
Total:		1400/event
Event rate:		(Hz)
instantaneous μ decay rate		5×10^8
accelerator duty factor	0.06	3×10^7
trigger selection: $E_\gamma > 35$ MeV	0.001	
solid angle of photon arm	0.7	
conversion probability	0.1	
raw trigger rate:	4.2×10^{-6}	2.1×10^3
total data rate:		~ 3 Mbytes/s

of the e^+e^- pair, without using any sophisticated fitting program, to get a crude measure of the photon energy and conversion point and time. Then, the positron filter code (“online ARC”) uses the information provided by PAIRS and the restrictive kinematics of a two body decay to look for a candidate positron track. The basic algorithm is as follows:

1. Search for hit positron scintillators located in a $\sim 90^\circ$ azimuthal window determined by ϕ_γ . (The width of the window depends on the z component of the photon conversion point.)
2. Select the positron scintillators in this window whose times are between -5 ns and 40 ns relative to the photon.
3. Look for Snow White triples correlated with the selected positron scintillators. Use this triple location, the photon conversion point information and the measured times from the photon and positron scintillators to estimate the track parameters and muon decay point for a 52.8 MeV positron back-to-back and in time coincidence with the photon at the decay point.
4. From the calculated positron track, assemble an expected list of struck MWPCs, and generate liberal windows around the expected crossings through these chambers. Search for MWPC hits within these so-called ARC windows. At least three anodes and two triples (including a Snow White triple) are demanded for each possible track. *No fitting is done at any stage.*

If the event meets the above requirements, it is reformatted and sent to the controlling microVAX for taping. The net rate suppression is about 0.004 (in 1992) and it brings the event rate down to 8 events/s. The definitions of the on-line ARC fail codes are listed in Table 15:

Table 15: Definition of on-line ARC reconstruction fail codes

Fail code (IRCN)	Explanation
-18	No hit e^+ scintillator is found in azimuthal window determined by ϕ_γ .
-17	Failed to find time of the hit scintillator located between -5ns and 40ns.
-16	No hit e^+ scintillator found in $30\text{cm} < z < 60\text{cm}$. (not used)
-15	Failed to find hit Snow White anodes near the hit scintillator.
-14	Failed to find Snow White triples near the hit scintillator.
-13	Failed to reconstruct 52.8 MeV positron track ("ARC track").
-12	ARC track hits the beam pipe.
-11	ARC track doesn't hit enough Dwarf chambers.
-10 → -7	Too many missing Dwarf chamber anode hits.
-6 → -4	Too many missing Dwarf chamber triples.
-3	Event passes on-line ARC.

3.7 Analysis Programs

3.7.1 REPLAY

The offline analysis program for all data from the MEGA experiment ($\mu \rightarrow e\gamma$, Michel decays, cosmic rays, etc.) is called REPLAY. This program provides a standard framework for unpacking and reformatting the raw data and applying standard correction such as ADC pedestal subtraction and TDC equal-time offset subtraction, all under control of the experimenter through a command line interface. High level reconstruction, analysis and data visualization routine are incorporated straightforwardly into the REPLAY program. Although it depends on the VAX-specific Q data acquisition system[42] to read the data tapes written by the experiment's master microVAX computer, this reliance has proven to be superficial: REPLAY has been ported successfully from the original VAX platform to the faster DECstation, DEC Alpha and HP workstations.

3.7.2 Histogramming

A histogramming facility, HODA, is included in REPLAY that permits the experimenter to histogram any of a set of 10,000 raw and calculated quantities stored in an online data vector for each event.

One- and two-dimensional HBOOK histograms can be defined dynamically by typing commands while running REPLAY. These histograms can be filled once per event (e.g., a decay point scatterplot), or multiple times per event (e.g., a list of all struck positron scintillators for a frequency plot). These histograms are written into an HBOOK4-compatible file at the end of a REPLAY job for later examination with PAW[52].

3.7.3 SED

A single event display package, SED, is incorporated into the REPLAY framework. SED responds to user commands (keyboard and mouse) to display various aspects of an event in one or more windows on the screen. Printed copies are also available.

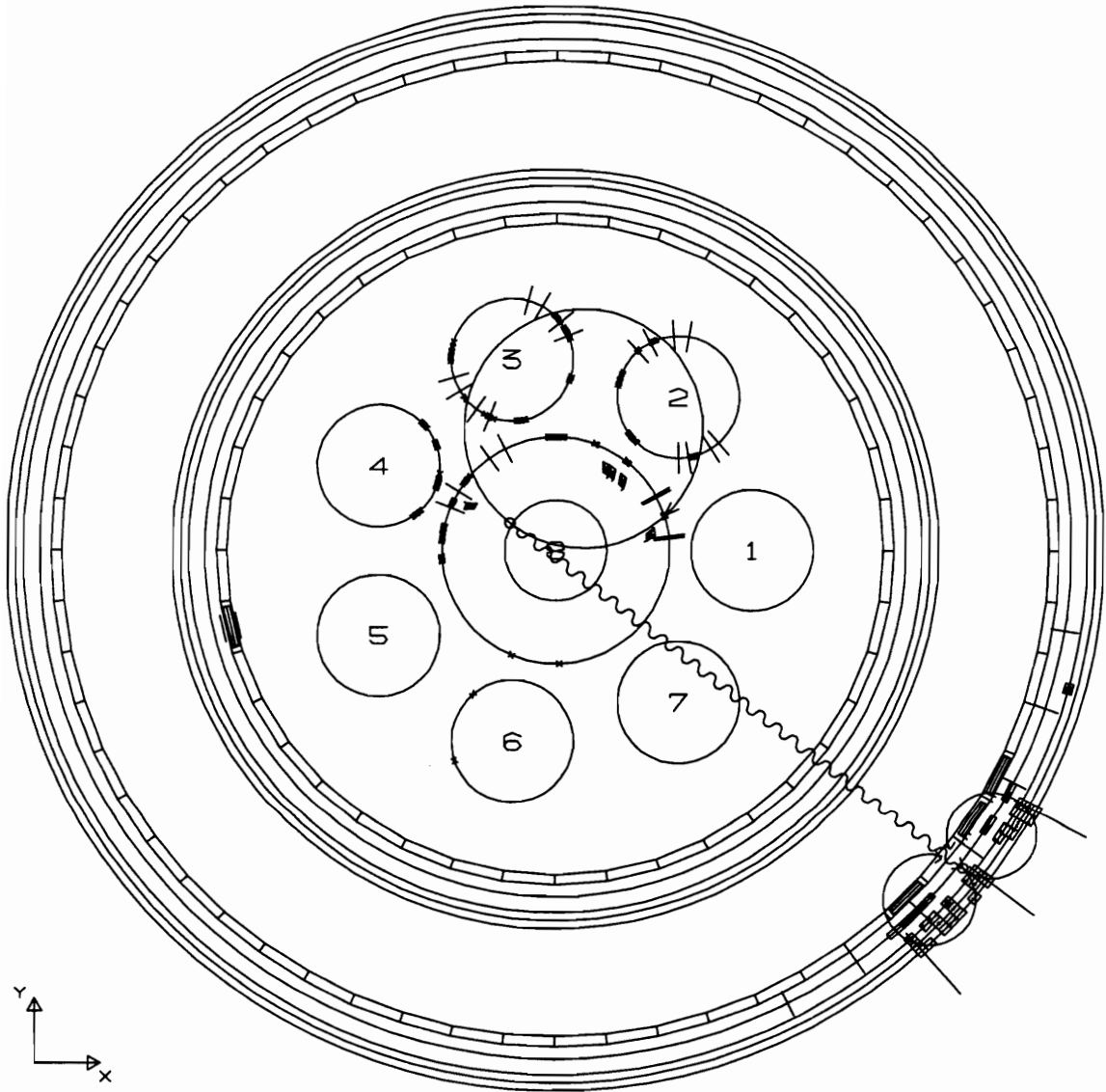


Figure 22: Graphical output of Single-Event-Display

Because SED was designed around the TEMPLATE[43] graphics package—not available on our Unix workstations—it remains bound to the VAX platform. (However, it can route its graphics output to any X11-server if the host VAX is on a TCP/IP network.) Fig. 22 shows a $\mu \rightarrow e\gamma$ candidate event as display by SED.

3.7.4 Positron Reconstruction Program

The Electron Reconstruction Code, ERC[44], is a successor to the Michel Reconstruction Code (MRC) that was used in the 1990 $\mu \rightarrow e\gamma$ data analysis and in the RHO experiment analysis. While MRC was, by design, limited to low rate data, ERC is able to reconstruct multiple tracks reliably at high muon stopping rate. Also, with low rate data, a comparison of the performance of ERC and MRC provides us with information on possible systematic biases in the reconstruction of positron helices. (For example, MRC's structure implicitly assumed the presence of a vertically oriented muon stopping target, while ERC's did not, so MRC's determination of the decay point did not work when used with the slanted MEGA target.)

ERC's design goals were: (1) to be able to reconstruct multiple helices in a single event, (2) to be able to reconstruct a track even if it was somewhat contaminated with noise or had a reasonably small number of missing hits, (3) to use a reasonable method to do the fitting that generates standard χ^2 values to indicate goodness of fit, (4) to be able to reconstruct non-standard tracks—in particular, positrons emerging from the Ring Counter, and to allow different target geometries and to be able to find all intersections of the helix with the target.

Because of the helical trajectory of positron in the magnetic field, the program has to treat the track as a helix parameterized by the following equations:

$$x = x_c + R \cdot \cos \omega \quad (62)$$

$$y = y_c + R \cdot \sin \omega \quad (63)$$

$$z = z_0 + s \cdot (\phi_0 - \omega) \quad (64)$$

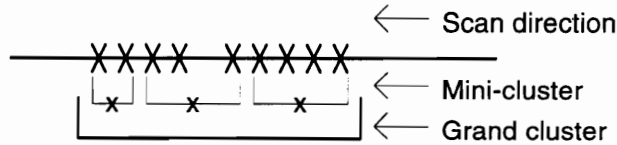


Figure 23: ERC Cluster.

ERC's task of reconstructing a helix proceeds in three steps: (a) assembling a list of chamber hits (x_i, y_i, z_i) , (b) fitting a circle to the (x_i, y_i) hits and thereby assigning a winding angle ω_i to each hit, then fitting a straight line to the (z_i, ω_i) data, and (c) applying a set of quality cuts to exclude fake tracks.

In the first step, ERC defines the wire cluster as the unit of hit information for reconstructing a track. Fig. 23 shows an ERC wire cluster that contains a set of mini-clusters and a grand cluster. The mini-cluster size is limited to four wires; its width and centroid are encoded by saving the first and last wire of the mini-cluster. Each mini-cluster is also assigned a grand cluster label. (A grand cluster is typically limited to 12 struck wires, not counting the allowed missing holes. When analyzing the 1992 data, this was expanded to 15 struck wires.) ERC triples are made up of anode, inner cathode, and outer cathode mini-clusters in spatial coincidence; they are identified by a three-dimensional ultra-cluster label that gives the mini-cluster number for anode and the two grand cluster numbers for the inner and outer cathodes, plus an upstream/downstream flag and a chamber number. This clustering information is necessary to provide ERC's track finder with a reasonably segmented set of three-dimensional points from which to select in constructing a track with the best χ^2 .

The character of the ERC track finding method is to reduce the problem of finding

a track to one of finding a tight grouping of the value of some single number that characterizes the track. For circle finding, from the list of chamber (x, y) hits, three points are selected to define a candidate circle. The points cannot be from the same grand cluster, and must be from two or three distinct chambers. A local coordinate frame is defined so that the first two points have coordinates $(0, \pm y')$ and the circle is centered at $(x'_c, 0)$ with radius $r = \sqrt{x'^2_c + y'^2}$. A search through the remaining hits is performed to see if a tight group of hits can be found near the candidate circle. If enough close hits are found, then ERC proclaims to have found a circle candidate, and a fit to these hits is performed. Transforming back to the lab frame, the circle parameters (x_c, y_c, R) are chosen to minimize the unweighted RMS variance for R^2 :

$$\sigma_{R^2}^2 = \sum_i (R^2 - [x_i - x_c]^2 - [y_i - y_c]^2)^2 \quad (65)$$

These circle parameters are used to calculate the goodness of fit:

$$\chi^2 = \sum_i \frac{(R - \sqrt{[x_i - x_c]^2 + [y_i - y_c]^2})^2}{w_i^2} \quad (66)$$

where

$$w_i = (\text{width of cluster})/\sqrt{12} \quad (67)$$

The probability of obtaining this χ^2 for the given number of degree of freedom is used for testing the quality of the fit.

A set of acceptance criteria is applied to eliminate bad circles: (1) at least four different grand clusters on the circle, (2) a χ^2 probability greater than 10^{-4} , (3) a circle radius between 4cm and 17cm, and (4) a circle center within 5.5 cm of the z axis.

Two checks are made to avoid duplicate tracks:

1. After finding a candidate circle, its center and radius are checked against the list of previously found circles. If they both match to within one centimeter, the two circles are considered to be the same circle and only the circle with the larger number of grand clusters is kept.

2. After all circles have been found, each pair of circles is examined once more. Either one of the circles must have at least two grand clusters not on the other circle to be considered distinct. Otherwise, only the circle with the larger number of grand clusters is kept. (If they are tied, the circle with the better χ^2 is kept.)

For the side view fit, ERC finds the best fit straight line relation between the z coordinates of the hits used in the circle fit and the orbit phase $\phi = \phi_0 - \omega$ of these hits:

$$z = s \cdot \phi + z_0 \quad (68)$$

ERC chooses the offset of ϕ so that the positron hits the lead at $\phi = 2\pi n$ (n an integer) and the decay point is in the range $0 < \phi < 2\pi$. Then, ERC finds candidate slopes between adjacent and next-to-adjacent triples (sorted in order of increasing z), and histograms these slopes. The data list is examined to find additional hits near these candidate slopes. A linear least squares fit is performed on each group of hits; the best fit slopes are used in a repeat of this search-fit process. After the second pass, at most one side view hit is assigned to each circle. (For some circles, the side view fit fails.)

Selection criteria are imposed to discard bad side view lines:

1. The track should have at least 3 hits. Two-hit tracks are permitted only if the two hits are in same loop and are over the lead, as happens for tracks emerging through the Ring Counter.
2. The track must either intersect the target or be in the central region of the detectors in the first loop.
3. The probability of the linear fit χ^2 must be greater than 10^{-4} .

As before, duplicate side view fits are compared and only the better of the two is kept. If either fit has a χ^2 probability below 0.10, the fit with the better probability is kept. Otherwise, the track with the largest number of different grand cluster pairs

is kept. (If a tie occurs, the track with the smallest number of loops is kept; if another tie occurs, the track with best side view fit χ^2 is kept.)

Before ERC deems a combined circle-fit and side view fit to be a “golden track,” the hit scintillators relevant to the track are checked and final track quality tests are imposed:

1. Tighter cuts on the end view and side view fit χ^2 are applied (optional).
2. The helix has no missing or extra loop.
3. In low rate data only, the helix is discarded if too many triples are left unused in the fit.
4. A good intersection with the target is required.

ERC was tested by analyzing low rate 10.5K Michel decay events with both slanted and vertical targets. Table 16 shows the reconstruction fail code results for the slanted target case. A typical Michel decay track reconstructed by ERC is displayed in Fig. 24.

3.7.5 Photon Reconstruction

The flow chart of the photon reconstruction program, PAIRS, is shown in Fig. 25. The online version of PAIRS is used in MEGA as a data filter, for which the requirements are (1) to perform a crude reconstruction of the photon e^+e^- pair; (2) to make a rough measurement of the photon energy and time, and (3) to give a reasonably precise measurement of the photon conversion point. The code is composed of three parts: the “root” section, the edge determination subroutine, and the vertex searching subroutine; followed by the calculation of the physical parameters of the photon, such as the energy and timing.

The “root” section searches for hits on DC2 and DC3 of the triggering photon spectrometer layer, and makes a fast selection to exclude bad events. The events pass only if they have (1) at least three non-adjacent DC2 hits with a minimum azimuthal width of fourteen cells and a maximum width of twenty six cells; (2) at least two

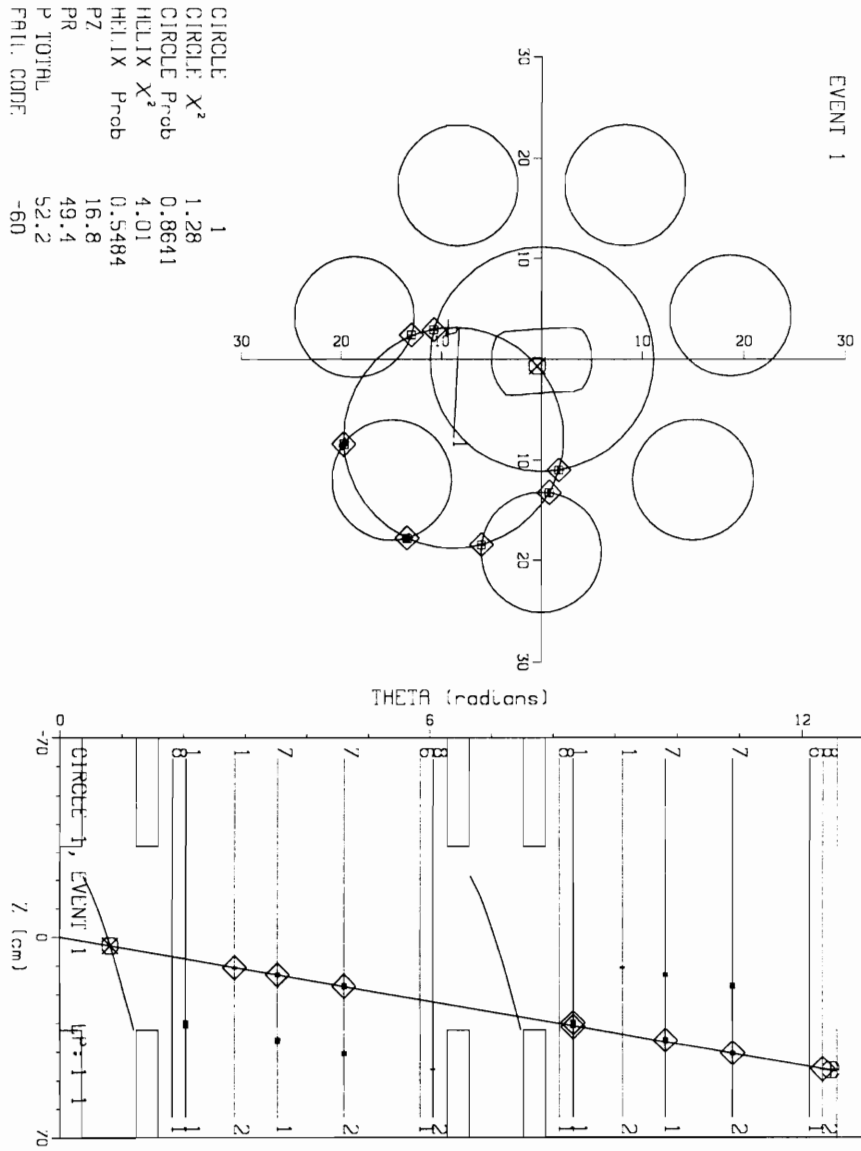


Figure 24: Display of a positron track reconstructed by ERC.

Table 16: Slanted target ERC reconstruction failures for Michel tracks

Fail code	Explanation	Events Cut	Fraction of Remainder
	Total Events ($\mu \rightarrow e\nu\bar{\nu}$)	10548	100.00%
-1 to -19	No circle found	953	9.03%
-20 to -39	No helix found	1473	15.35%
-40	Failed secondary circle χ^2 cut	1058	13.03%
-41	Failed secondary helix χ^2 cut	2	0.03%
-42	Missing loops	368	5.21%
-43	Extra loops	78	1.17%
-44	Too many unused triples	291	4.40%
-45	No intersection with target, weak cut	89	1.41%
-46	No intersection with target, strong cut	3	0.05%
-47	No scintillator hits	183	2.84%
-48	Extra scintillator hits	31	0.51%
-60	Golden track	6019	100.00%

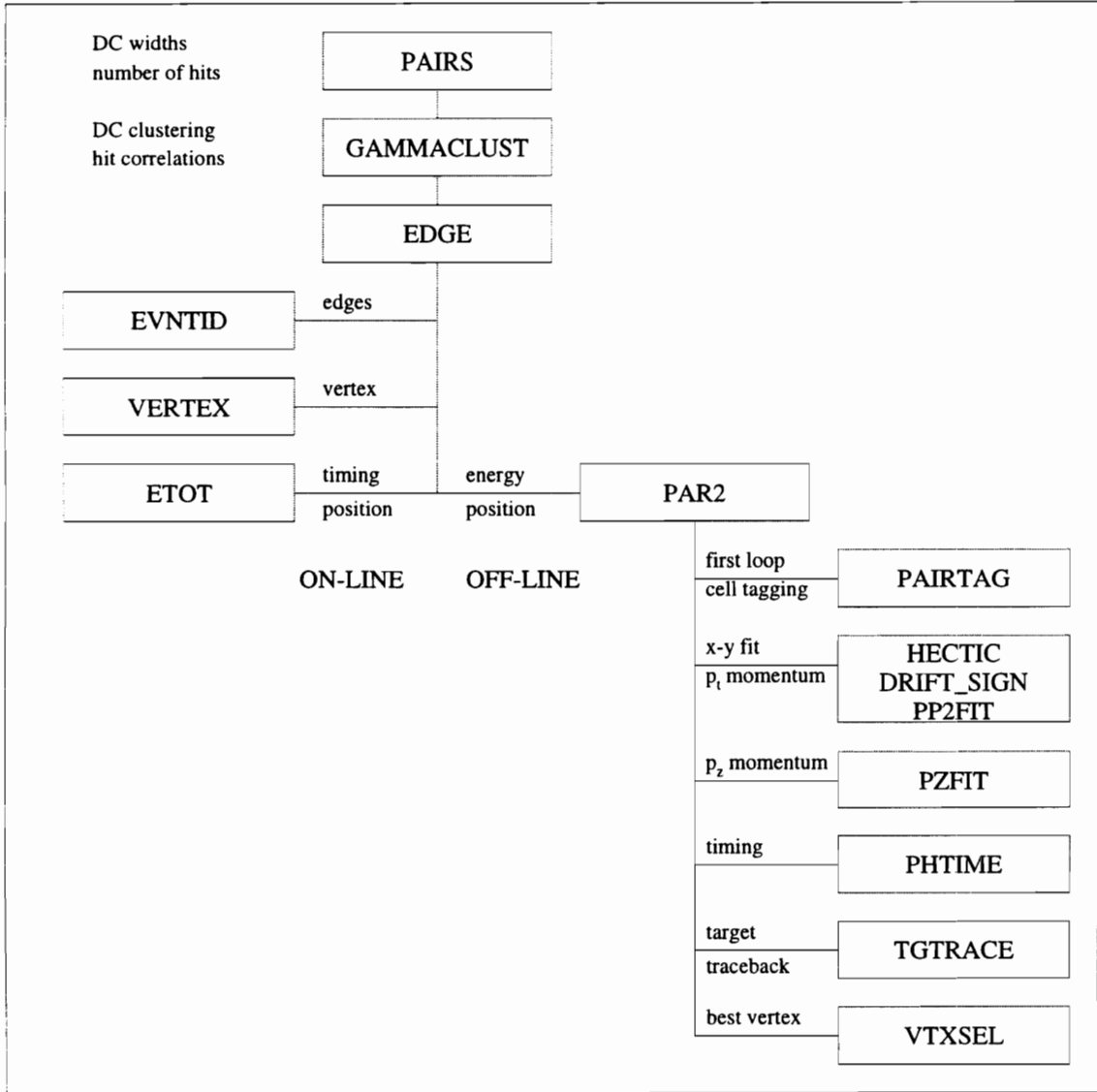


Figure 25: Photon arm pattern recognition code structure.

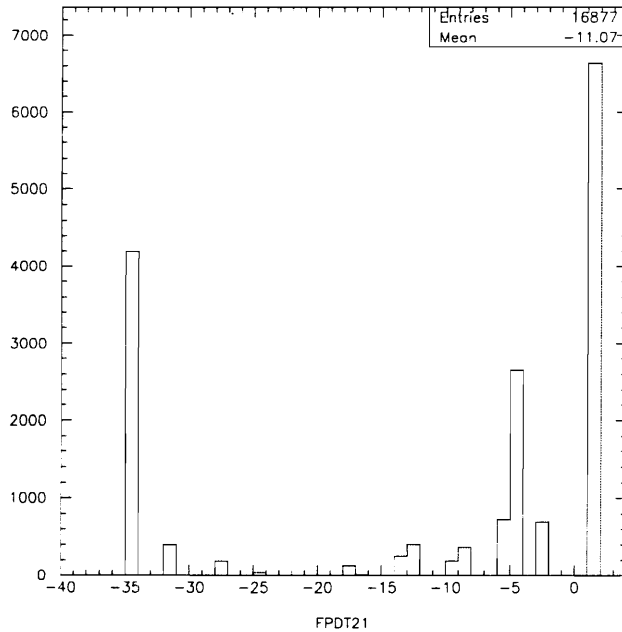


Figure 26: PAIRS fail code distribution for MEGA run 2839 (see Table 17).

non-adjacent DC3 hits, correlated with the DC2 hits, that span ten cells in width. A loose drift distance cut is applied to eliminate hits that have very long drift times. The z -measuring delay lines on DC1 must have TDC hits on both ends.

The Fig. 26 shows a typical reconstruction fail code distribution (“FPDT21”) of on-line PAIRS for a 1992 data run. About one quarter of events were rejected by the requirement of sufficient track hits in DC2 and DC3 ($-6 \leq \text{FPDT21} \leq -2$). About 7-8% events failed since they either had very long drift time or had only single-ended readout of the delay line ($-18 \leq \text{FPDT21} \leq -13$). The percentage of “fireball” events, where too many adjacent channels fired ($-10 \leq \text{FPDT21} \leq -9$), is about 5%. The remaining events pass the root section.

The EDGE subroutine classifies each particle in the e^+e^- pair into for categories: 3-edge, 2-edge, 1-edge and 0-edge, according to the number of drift chamber layers that the particle penetrates. Good pairs have 2-3, 3-2 and 3-3 edges; “bad pairs” have 0-3, 3-0, 1-3, 3-1, 2-2 edges; and Compton-generated electrons have 0-3 edges. (Note

Table 17: Definition of on-line PAIRs reconstruction failed code

Fail code (FPDT21)	Explanation
-35	Photon pattern recognition failed.
-32	DC2 - DC3 correlation failed.
-29	DC1 hits too narrow after TDC cut.
-28	Too few hits in DC1 or only one hit on delay line.
-25	“Fireball” in DC1.
-22	DC1 hits too narrow.
-21	Too few hits in DC1.
-18	DC3 hits too narrow after TDC cut.
-17	Too few hits in DC3 after TDC cut.
-14	DC2 hits too narrow after TDC cut.
-13	Too few hits in DC2 after TDC cut.
-10	“Fireball” in DC3.
-9	“Fireball” in DC2.
-6	DC3 hits too narrow.
-5	DC2 hits too narrow.
-3	Too few hits in DC3
-2	Too few hits in DC2
0	No filtering required
1	Events pass on-line PAIRS

the ambiguity in classifying the 0-3 case as either a Compton scattering or as a very asymmetric e^+e^- pair where the e^- carries off nearly all of the photon energy.) Dead cells are treated as hit cells without any drift time information in this classification. The 1-3 or 3-1 edge pairs are discarded since there is not enough information available to reconstruct the pair. The 2-2 edge pairs are rejected because their energy is too low to be of interest. The edge algorithm scans from the outer azimuthal limits of the shower inward, searching first for the positron edge and then for electron edge. For example, simulated 52.8 MeV photons are classified as “good” pairs 69.4% of the time, as “bad” pairs 22.6% of the time, and as Compton electrons 8.0% of the time.

After finding the two edges of a pair, the vertex finding algorithm searches for an intermediate cluster of DC hits that makes it appear as if the pair’s particles originate from a common point in either the inner or outer lead converter sheet (but not in the photon scintillator or the supporting aluminum can—so-called “deep pairs”). For the simulated 52.8 MeV photons, the correct vertex is found about 98.7% of the time for the good pair events, 24.9% of the time for the bad pair events, and 4.3% of the time for the Compton electron events.

Finally, the online subroutine, ETOT, calculates the diameter of each track $2r^\pm$ as the distance between the edge and the vertex, then estimates the transverse momenta via

$$P_r^\pm = r^\pm \cdot B \cdot c \quad (69)$$

The longitudinal momenta are estimated via

$$P_z^\pm = P_r^\pm \cdot \tan \theta^\pm \quad (70)$$

where

$$\tan \theta = \frac{r_{edge}^\pm - r_{vertex}^\pm}{\pi^\pm r} \quad (71)$$

The photon momentum is obtained from vector sum of the pair’s momenta. (This algorithm has been replaced by a more accurate one for the analysis of the data taken in 1993–95.) The photon conversion time is estimated by:

$$T_\gamma = \frac{1}{2}(T_{SC}^+ - T^+ + T_{SC}^- - T^-). \quad (72)$$

$$T^\pm = 1.2 \frac{\pi r^\pm}{c} \quad (73)$$

T_{SC}^\pm denotes the readout meantimes of the edge scintillators, and T^\pm is the propagation delay particle along its first half revolution. The factor of 1.2 accounts for typical dip angle of a 52.8 MeV photon of interest to us.

The off-line PAIRS package within REPLAY is based on the on-line PAIRS but it uses a sophisticated fitting subroutine, PAR2, in place of the simple-minded ETOT. PAR2 has additional features which includes pair track fitting, energy loss correction, photon traceback to the target, and best vertex selection.

Before doing pair track fits, PAR2 tags all of the hit cells produced by the first loop when the pair enters the drift chambers, then imposes two types of cuts to eliminate Compton electron and ‘‘Deep pair’’ conversion. (Deep pairs were defined in the online-PAIRS section.) Initially, an unweighted fit is applied to the passing events by using only the sense wire positions of the struck drift chamber cells. Then, a weighted fit is done, including the drift distance from the first-pass tracks to the sense wires. Finally, a non-linear fit is done in which the two independent circles from the second pass are correlated and these circles are assumed to pass through a common vertex. For a successful fit, the photon momentum components are computed as in equations (69)-(70) with r^\pm from the PAR2 fit, and the tangent of the dip angle from the expression:

$$\tan \theta^\pm = \frac{z_{edge}^\pm - z_{vertex}^\pm}{\pi(r_{edge}^\pm - r_{vertex}^\pm)} \quad (74)$$

Since the ‘‘inner’’ conversion pair traverses more material than the ‘‘outer’’ pair before the pair momenta are measured in the drift chamber, the energy resolution of the inner photon is worse than of the outer photon. Off-line PAIRS makes a mean energy loss correction of 2.10 MeV (0.56MeV) for the inner (outer) layer, as determined from a Monte Carlo study.

The reconstruction of the photon momentum provides a measure of the photon direction, but the resolution is poor due to multiple scattering within the heavy

Table 18: Comparison of the best vertex selection method for 52.8 MeV photon

Method	Fraction of events	Correct vertex choice fraction
Second loop	0.874	0.984
Pattern	0.051	0.917
Lowest χ^2	0.075	0.584
All	1.000	0.950

materials in the photon spectrometer. The axial FWHM of the photon traceback to the z -axis, measured in 1993 with all three spectrometers operational, is:

- (10.4 \pm 0.2) cm - for pair spectrometer 1;
- (14.3 \pm 0.3) cm - for pair spectrometer 2;
- (17.6 \pm 0.5) cm - for pair spectrometer 3.

This information is still helpful in the $\mu \rightarrow e\gamma$ analysis in reducing random coincidences between positrons and photons.

The off-line PAIRS selects one of several candidate photon conversion vertices as the best. It counts and classifies the drift chamber hits between the edges and the vertex candidate produced by on-line PAIRS, and checks to see if it can find the second and even the third loops of the pair; this information helps it select the “true” vertex and exclude the “false” ones. If no higher order loops are found, the program decides on the best vertex using the edge-and-vertex patterns (e.g., for 2-3 and 3-2 edges, the vertex closest to 2-edge side is chosen). If both methods fail, the program chooses the vertex candidate using the track with the better fit.

Table 18 shows the performance of the three selections for 52.8 MeV Monte Carlo photons. Using all three methods, off-line PAIRS selects the correct photon vertex

95% of the time.

3.8 Monte Carlo Simulation

A fairly sophisticated Monte Carlo simulation code is needed for any nuclear and particle physics experiment, initially for the optimization of detector system design, later for the development of analysis software and for the understanding of data quality and analysis. Because of these requirements, the code should be capable of giving a realistic descriptions on the production and transport of the particles through a detailed model of the detector, including a faithful representation of the electronics signal processing. MEGASIM, the Monte Carlo simulation code of the MEGA experiment, was designed and developed to have the capability to achieve above requirements[45]. It was designed to include all of the detector and signal modeling of the older PATH/DETECT simulation, but used the EGS4[46] electromagnetic shower transport code instead of BREM2[47] for the physics processes. In its first incarnations, MEGASIM was written to handle the simulation for the RHO experiment, and therefore incorporated only the positron spectrometer geometry. A separate EGS4-based Monte Carlo program, PARMMC, was used to simulate the response of the photon spectrometers to incoming photons. PARMMC is described in the dissertations of L. van Ausdeln[48] and M. Dzemedic.[49]

MEGASIM is composed of three parts. The first part generates the history of an electromagnetic particle or a cosmic ray muon through the positron spectrometer until it either leaves the detector system or is stopped and absorbed in one of the lead pipes. The physical interactions between the particle and the detector materials is simulated using the EGS4 package. The EGS4 subroutines calculate all of the electromagnetic processes of the particles with detector materials over discrete steps as long as the energy of particle remains above a user defined threshold. The interactions modeled by EGS4 are list in Table 19. (The muon electromagnetic interactions were taken from the GEANT package and incorporated into the EGS4 framework within MEGASIM.) In addition to these discrete interactions, a continuous energy loss process is imposed on charged particles that mimics the production of sub-cutoff

Table 19: Interactions imposed in EGS4

μ^\pm	Bremsstrahlung Production e^\pm Pair production Moliere multiple scattering Delta ray production
e^\pm	Bremsstrahlung Production Positron Annihilation Moliere multiple scattering Moller and Bhabha scattering
γ	Pair Production Compton scattering Photoelectric Effect Rayleigh scattering

electrons from atomic ionization or excitation. The EGS4 package is enhanced in MEGASIM to properly account for single and plural scattering in thin media, as well as “Vavilov”-like fluctuations in the continuous energy loss. The outputs of this part are a list of nine kinematic parameters: x , y , z , t , p_x , p_y , p_z , E , and the index of the material the particle passes through. These parameters are recorded into a “history file” and are also available for conversion into the standard detector hits by the next code section. Multiple Michel tracks, each originating at different times, can be superimposed onto each signal frame (whether $\mu \rightarrow e\gamma$, $\mu \rightarrow e\gamma\nu\bar{\nu}$ or any other process) to simulate the high rate of muon decays in the MEGA experiment.

The second part of the code assembles event frames by using the output of the first part and modeling the detector response of each hit in detail. For each crossing of a positron track through a chamber, the primary ionization is proportional to the energy deposited into the chamber gas by the incident particle. The ion clusters from the ionization are randomly distributed along the trajectory of the particle. The charge is then collected either in the nearest cell or in the neighboring cells where

applicable. The Gaussian shaped pulses, with amplitude proportional to the collected charge, is processed by a digital sampling procedure for a period T_{gate} starting at the trigger. Multiple hits from a high loop-number track on the same wire are therefore superimposed and form a non-Gaussian broadened pulse. Hits will be registered in a software latch only if the accumulated signal amplitude exceeds the threshold and overlaps the latch gate. Scintillator hits are processed in a similar fashion (including pileup).

The third part of the code is used to generate a data file that is directly readable by REPLAY. The detector element hits are transformed into the module data according to the FASTBUS format and then written into a data file that has the same structure and format as the real data file.

MEGASIM selects the geometries of the detector and electronics readout parameters, such as the pulse shape and thresholds of the discriminator, from a standard MEGA database. It reads user requirements from a command file that selects various physics processes (e.g., $\mu \rightarrow e\gamma$ decay), cut parameters (e.g., low energy threshold and solid angle cuts), and the trigger definition. It then simulates a set of events under these conditions and write the results to one or more of the above-mentioned output files for later processing by REPLAY.

Chapter 4

Experimental Detector Response

4.1 Overview of 1992 Data Taking

The 1992 run was from June 25 to October 14, and consisted of three stages. During the “testing” stage, from June 25 to July 15 and from August 11 to August 31, the positron and photon spectrometers were set up and tested. The photon spectrometer setup is described in detail in the dissertation of M. Dzemedzic[49].

Since the final gas system for the positron spectrometer was not available during the testing stage, the MWPCs were set up and tested two at a time using a smaller capacity gas system. The delay time, the threshold and gate width of discriminators, wire efficiencies as function of applied voltages were studied. The TDC and ADC spectra for each positron scintillator were checked. Grounding of the MWPC signal cables were adjusted to reduce the amount of high frequency oscillation from the chamber-mounted preamplifiers. All detectors were installed in the magnet; all channels except for 20% of the layer 2 photon spectrometer’s z -readout cathode delay lines were instrumented for readout. The engineering tests on both spectrometers were processed with the Routing Box and general purpose Programmable Logic Unit (PLU) modules since the “Chicago Box” was not available until the third stage of running.

The second stage, the engineering run for the measurement of the Michel ρ parameter in $\mu \rightarrow e\nu\bar{\nu}$ (LAMPF experiment 1240) [50], lasted from September 13 to 27.

During this run, the downstream cathodes of dwarf 3 were unusable due to electronics oscillation. Also, dwarf 7 was turned off halfway into the run because of a broken anode. The data from this run is described in more detail in the dissertation of Fan Liu[51].

The third stage, the engineering run for the MEGA data experiment, was from September 27 to October 11. In this stage, the detector system consisted of the two inner layers of photon spectrometers and the complete positron spectrometer. Due to an insufficient supply of preamplifiers, about 20% the delay line z -readout in layer two of the photon detector were not instrumented. On the side of positron spectrometer, in addition to the positron arm MWPC readout problems that existed the RHO run, half of the anodes in dwarf 5 could not be read out because of a bad high voltage connection that developed at its upstream end in the beginning of this last stage. Altogether, about 15% of the positron arm acceptance was lost during this run. The “Chicago Box” was installed at the beginning of this stage, and the data acquisition system had four UNIX workstations rather than the design value of eight. Only the first level hardware trigger was available in 1992; the second level trigger was simulated in the workstations as part of the photon arm on-line software filter. The even-TDC readout of the upstream Ring Counter was lost during the run, causing a minor complication in calibrating the equal-time offsets for the positron arm and photon arm scintillators. The slanted target had a small rectangular hole (0.75×3.0 cm) cut into it to raise the stopping rate of muons on the downstream vacuum window as an aid in the scintillator timing calibration. In fact, this feature reduced greatly the number of muons stopping on the slanted target, and was eliminated after the 1992 run.

The detector performance and data corrections for the 1992 MEGA data will be given in the remainder of this chapter. The extraction of physics output from the MEGA data run will be described in next chapter.

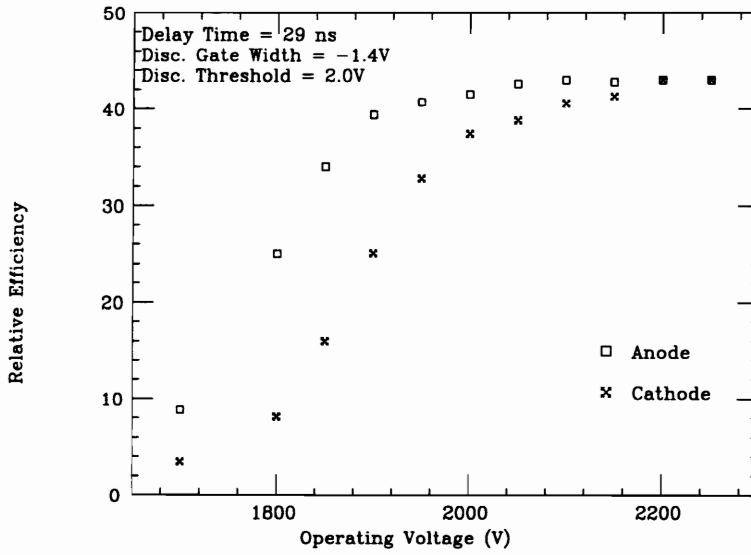


Figure 27: Anode and Cathode efficiency (relative) vs voltage. The operating voltage was typically set at 2150 V.

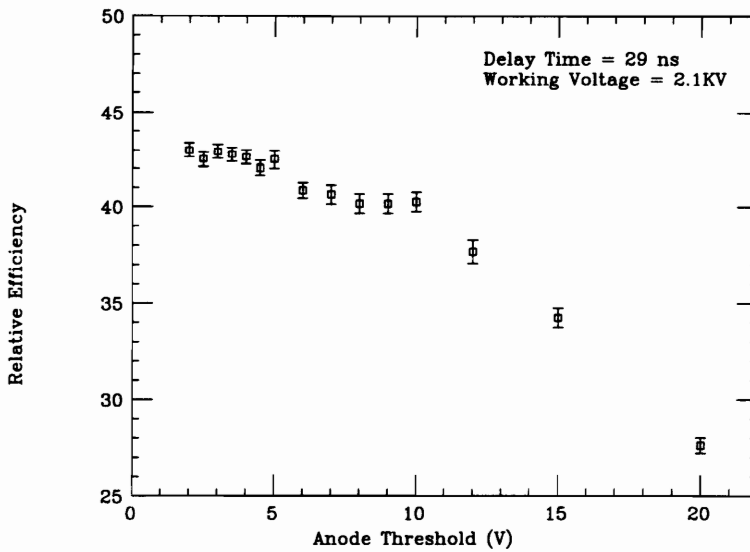


Figure 28: Anode efficiency (relative) vs the discriminator threshold.

Table 20: The positron MWPC setup

Chamber	Working Voltage (V)	Threshold set (mV)		Fraction of active channel	Comment
		anode	cathode		
Dw 1	2200	9.0	4.0	88.7%	
Dw 2	2200	9.0	4.0	88.7%	
Dw 3	2200	9.0	4.0	95.0%	Half of cathodes not read out
Dw 4	2200	9.0	4.0	88.7%	
Dw 5	2200	9.0	4.0	97.7%	Half of cathodes not read out
Dw 6	2150	9.0	10.0	83.7%	
Dw 7	-	-	-	0.0%	Turned off in ρ runs
SW	2200	9.0	4.0	95.0%	

4.1.1 Detector Performance

The detector tests for both positron and photon spectrometers were processed in the first stage of the 1992 run, from June 25 to August 31. For the positron spectrometer, the major testing included (1) the plateau curve measurement and MWPCs' working voltage setup, (2) the discriminator threshold and gate width setup, (3) the delay time (strobe time) setup, and (4) the dead and hot channels tabulation.

To select the working voltage of positron chamber, the plateau curve was measured on each chamber with a fixed discriminator setting. The working voltage was set at the starting point on the plateau of the efficiency (see Fig. 27).

The next task was to tune the discriminator gate width and threshold. For a working voltage and a specific threshold, we measured the relative efficiency of wire hits by adjusting the gate width, and set the gate width at the shortest value on the plateau of efficiency. With this fixed gate width, the relative efficiency was optimized

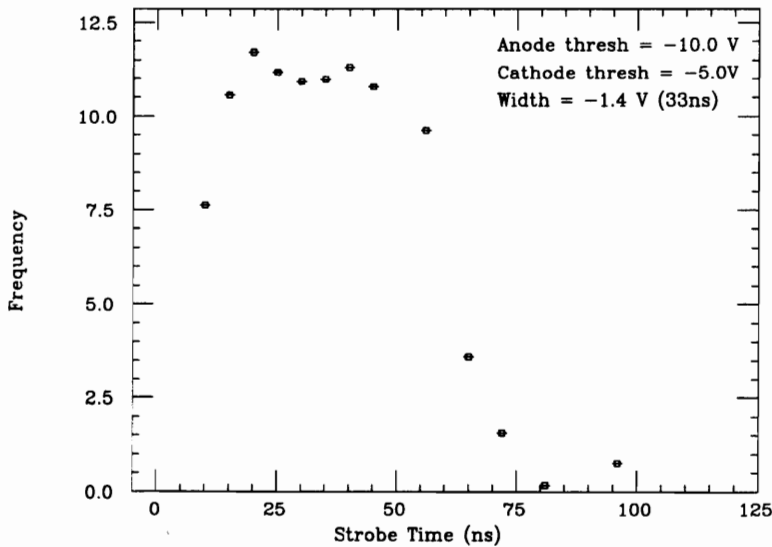


Figure 29: The strobe time vs Anode wire efficiency (relative).

by adjusting the discriminator threshold (see Fig. 28). The entire process was repeated to optimize both the gate width and threshold. The gate width was reduced to 14 ns to minimize the corruption of data by electronics noise. Table 20 shows the chamber setup in 1992.

The delay time or strobe time measures the time of the trigger signal from the Routing Box to the FASTBUS latch modules. The testing trigger was “COSMIC RAY.” By adjusting the cable length from Routing Box to the FASTBUS latches, we optimized the wire hit relative efficiency. The delay curve is shown in Fig. 29; the delay time was set at the leading edge of the plateau of this delay curve, which was 20ns.

The dead and hot channels were evaluated from wire frequency histograms. The fraction of active wires for each chamber is also listed in Table 20.

In the photon spectrometer, the detectors were more stable. The plateau curves of the MWPCs and DCs in each photon spectrometer layer were measured, and the working voltages and associated parameters such as gate width and threshold of

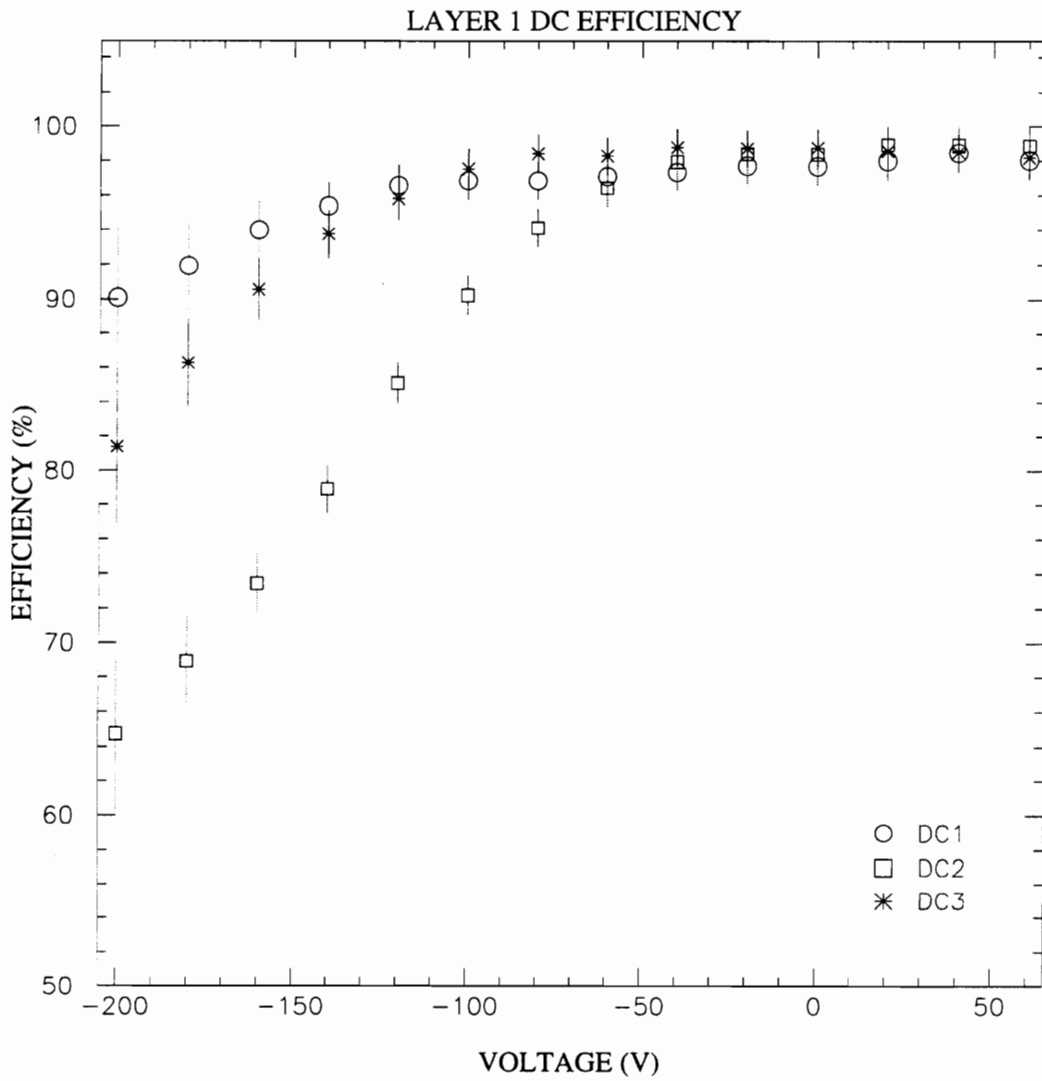


Figure 30: Plateau curve for the photon arm layer one drift chambers. Zero voltage corresponds to the nominal operating voltage, which is between 2100V to 2200V, depending on DC layer

readout electronics were set up. The length of the cable from each mean-timer of the photon scintillators to the Chicago Box was adjusted to bring their signals into the trigger in coincidence. Typical DCs plateau curves are shown in Fig. 30.

4.1.2 Data Collection

Two sets of data were taken alternately in the “MEGA data taking” stage: MEGA production data and detector calibration data. The calibration data were used to determine the detector response before the MEGA production data were processed. The types of calibration data taken in 1992 are listed in Table 21.

The photon energy resolution is extracted from the decay $\pi^0 \rightarrow 2\gamma$. A π^- beam is brought into the cave and converted to neutral pions by charge exchange, $\pi^- p \rightarrow \pi^0 n$. The π^0 decays in flight into two photons. If the opening angle of the photons is approximately 180° , the energy of each photon is about 55 MeV. By analyzing such photons, we calibrate the energy resolution for 52.8 MeV photons.

Cosmic ray data was taken with the magnetic field either on or off. For the photon spectrometer, the field-on data is used for delay line calibration, position (xy) vs time calibration, and photon MWPC efficiency determination. For the positron spectrometer, the field-off data is used to analyze the positron MWPC channel mapping and alignment, and for the inter-alignment between positron and photon spectrometers.

The positron energy resolution is extracted from the 52.8 MeV endpoint of the Michel energy spectrum from $\mu \rightarrow e\nu\bar{\nu}$ with the slanted target. This endpoint energy can be measured for different loop numbers (i.e., different polar angles) upstream and downstream separately. (The average energy loss in the target and chambers varies with polar angle.) The positron direction resolution is obtained from the Monte Carlo simulation. The simulation, which accounts for the energy loss and scattering in the target, gas, and MWPCs, is checked indirectly with other target geometries (e.g., a vertical target) and by verifying the agreement between the distribution of reconstructed direction when projected back to the target.

The determination of the muon decay point resolution uses the big hole target, which has a rectangular hole (2 cm \times 10 cm) at its center. By histogramming the

Table 21: MEGA detector calibration runs

Data type	Magnetic Field	Comments
$\pi^0 \rightarrow \gamma\gamma$	1.5 T	Photon energy resolution
	1.5 T	Photon reconstruction efficiency
Cosmic muons	1.5 T	Delay line calibration
	1.5 T	Photon detector efficiency and alignment
	0.0 T	Positron detector channel mapping and alignment
$\mu \rightarrow e\nu\bar{\nu}$ with slanted target	1.5 T	Positron energy and initial direction resolution
	0.0 T	Target location
$\mu \rightarrow e\nu\bar{\nu}$ with big hole target	1.5 T	Muon decay point resolution
	0.0 T	Target location
Timing calibration	1.5 T	Timing constants calibration and timing stability
Inner Bremsstrahlung	1.5 T	Relative $e - \gamma$ timing
RHO Michel data	1.5 T	Positron detector alignment and efficiency

crossing points of the reconstructed positron trajectory with the target plane, and then measuring the intervals of the distribution dropping from 90% down to 10% on the edges of the hole, we determine the decay point position resolution.

Scintillator timing calibration runs serve two purposes: to measure the per-channel invariants such as propagation delays in the cables and electronics, and to monitor the drift of these “constants” as the ambient temperature and/or other environmental conditions change. The calibration runs were taken every eight hours and included 200K events for TDCs calibration and 5K events for ADC pedestal calibration. (The ADCs calibration is necessary for the correction of the discriminated pulse’s “leading edge walk” with pulse height variation.)

Muon Inner Bremsstrahlung, $\mu \rightarrow e\gamma\nu\bar{\nu}$, is the physical process in which the positron and photon are coincident in time. This allows us to check the timing calibration constants. Since the detector setup is the same as for the $\mu \rightarrow e\gamma$ runs, IB runs also provide a method to check the overall detector setup.

The analysis of these calibration runs constitute the rest of this chapter. The following several sections will give detailed descriptions of the analysis as well as the results.

4.2 Positron Spectrometer Response

4.2.1 Channel Mapping and Detector Alignment

After the positron spectrometers were installed and instrumented, the channel mapping and detector element alignments were checked. Both the helical track and cosmic ray data were used to verify the FASTBUS-to-detector-channel mapping for both MWPCs and scintillators, and to check the alignment of the spectrometer elements.

The purpose of checking the positron chamber channel mapping is to ensure that the signal path of each MWPC anode and cathode to the FASTBUS latch modules was mapped correctly in the online database. This task employed $\Delta\phi$, the difference of the azimuthal angle of the inner and outer cathode crossing with that of the nearest

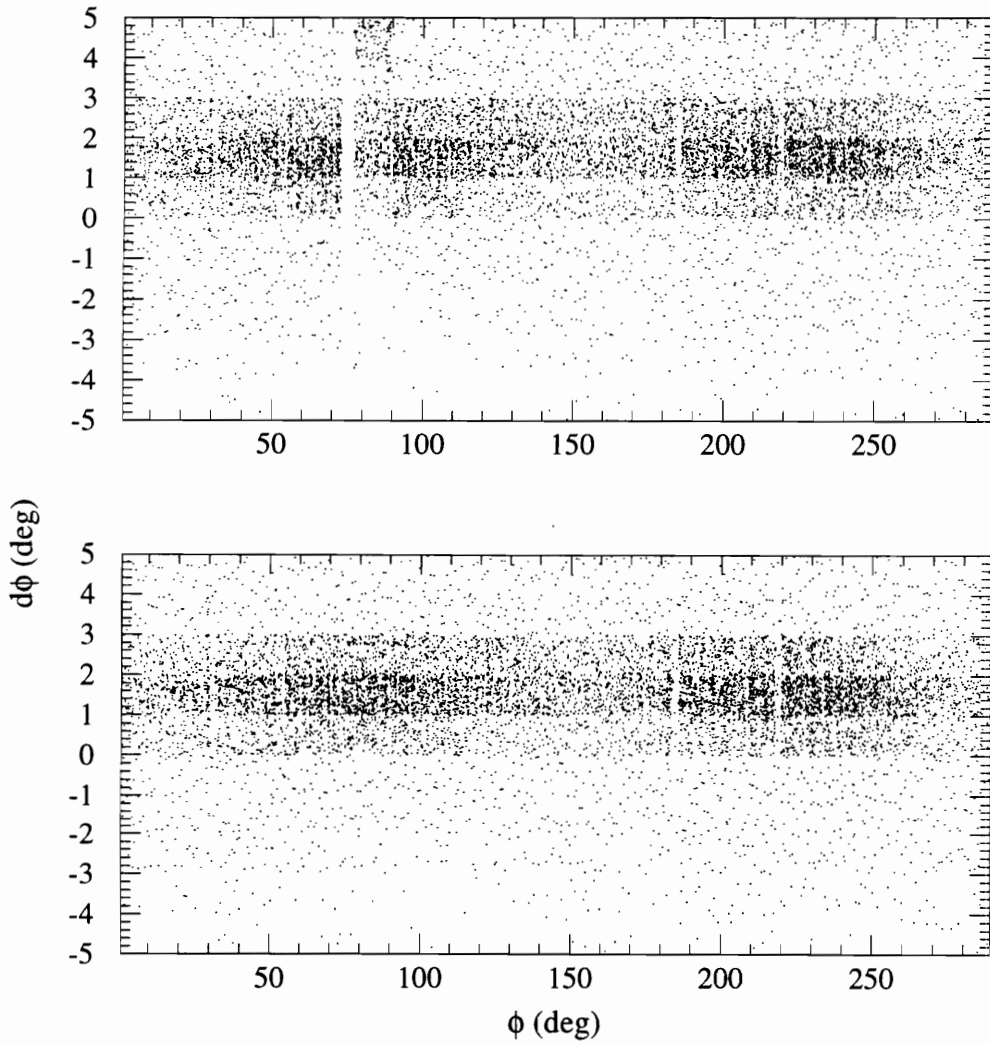


Figure 31: One example of the positron spectrometer MWPC channel map before and after correction of mapping errors.

anode cluster. A scatterplot of $\Delta\phi$ versus the anode cluster's ϕ would show a well-defined band at $\Delta\phi = 0$. Any deviation from $\Delta\phi = 0$ would indicate an error in the map. The top and bottom histogram of Fig. 31 show the $\Delta\phi$ distribution of dwarf 2 anodes before and after the channel mapping correction, respectively. (Note that the band is not yet centered on $\Delta\phi = 0$ because of an overall alignment shift between all anodes and cathodes.)

Compared to the channel mapping, the MWPC chamber alignment is a rather complex task because of the large number of degrees of freedom as well as the correlations among the alignment parameters. The analysis can be divided into two steps: the anode alignment, followed by the cathode alignment. Both helical tracks from Michel data ($B = 15$ kG) and straight line tracks from cosmic data ($B = 0$) were used for this purpose and also to check each other. The following description of the chamber alignment process applies to the Michel data; the cosmic ray data were analyzed by a similar method.

Some alignment parameters were fixed during the anode (end view) analysis: the radial size of each MWPC at $R = 5.982$ cm (dwarfs) and $R = 11.138$ cm (Snow White), and the tilt of chambers axes from the z axis at zero. Each step in the analysis used three chambers: Snow White and two adjacent dwarfs. (For cosmic ray data, the dwarf chambers chosen for the alignment analysis did not have to be adjacent.)

In the anode (endview) alignment, the anode clusters were fit to a circle (i.e., a helical track projected onto the xy plane). The distance of each anode cluster from the best fit circle and the cumulative residual for all tracks in the data set depended on three adjustable parameters: the angular offset, ϕ , that measured the chamber rotation about its axis, and the angular and radial displacements α and R of the chamber axis from the experiment coordinate axis. (See Fig 33 for the definition of these quantities.) By convention, Snow White was centered on the z axis ($R_{SW} \equiv 0$ and $\alpha_{SW} \equiv 0$) and the x axis passed through the symmetry axis of dwarf 1 ($\alpha_1 \equiv 0$). The correct anode alignment was obtained by adjusting ϕ , α and R for the three selected chambers to minimize the endview residual. This process was repeated for all 3-way chamber combinations. Fig. 32 shows the σ_a distributions before (top) and

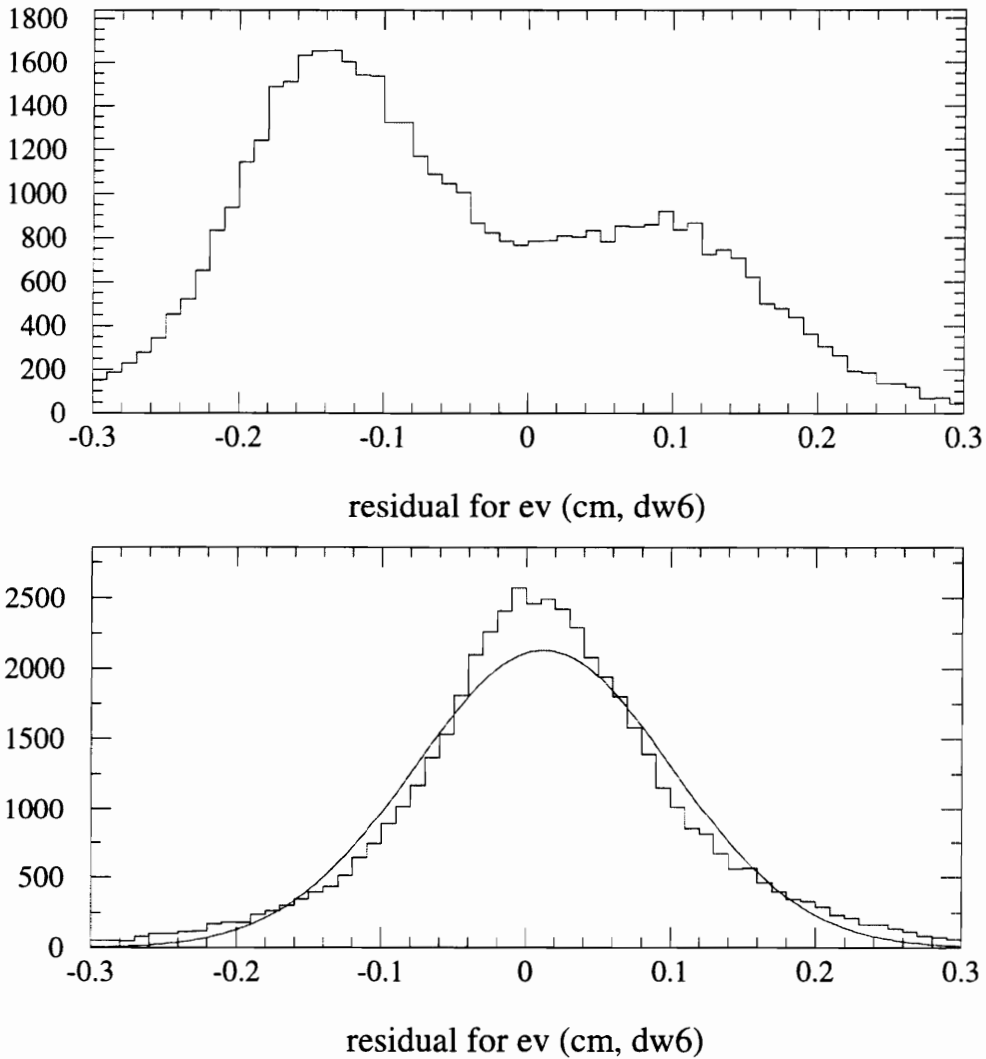


Figure 32: The circle-fit residual distributions of Dwarf 6 anodes before (top) and after (bottom) ϕ alignment.

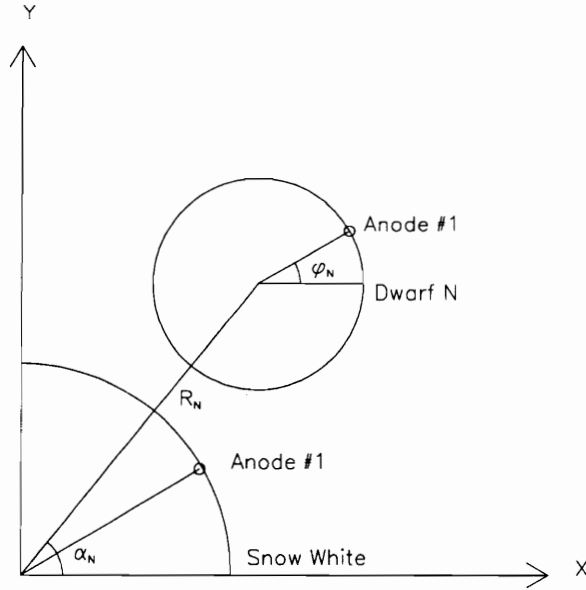


Figure 33: The parameters for MWPCs alignment.

after (bottom) the ϕ alignment corrections.

Following the anode alignment, the stereo cathodes were aligned. Holding the inner cathode foil fixed, the outer cathode was rotated azimuthally to minimize the cumulative variances $(\Delta z)^2 = (z_{in} - z_{out})^2$, where z_{in} (z_{out}) was the axial coordinate of the crossing of the anode and the inner (outer) cathode. Finally, both inner and outer cathodes were rotated azimuthally by the same amount to obtain a band centered on $\Delta\phi = 0$ between the anodes and the cathodes crossing (see Fig 31). (This common rotation is parameterized in the geometry database by an equivalent axial translation.) This shift was obtained by minimizing the cumulative residuals σ_z^2 , which is square of the z residual of each fit point from the best fit in the side view. Fig. 34 shows the example of the σ_z distribution before (top) and after (bottom) the cathode alignment was fixed. After completing the above alignment step, the cathode slope $d\theta/dz$ (or stereo angle) was calibrated by using cosmic ray data. As before, we minimized the cumulative residuals σ_z^2 by allowing the cathode slope to float.

The z locations of the garlands were used to check the cathode slope. A hit on a

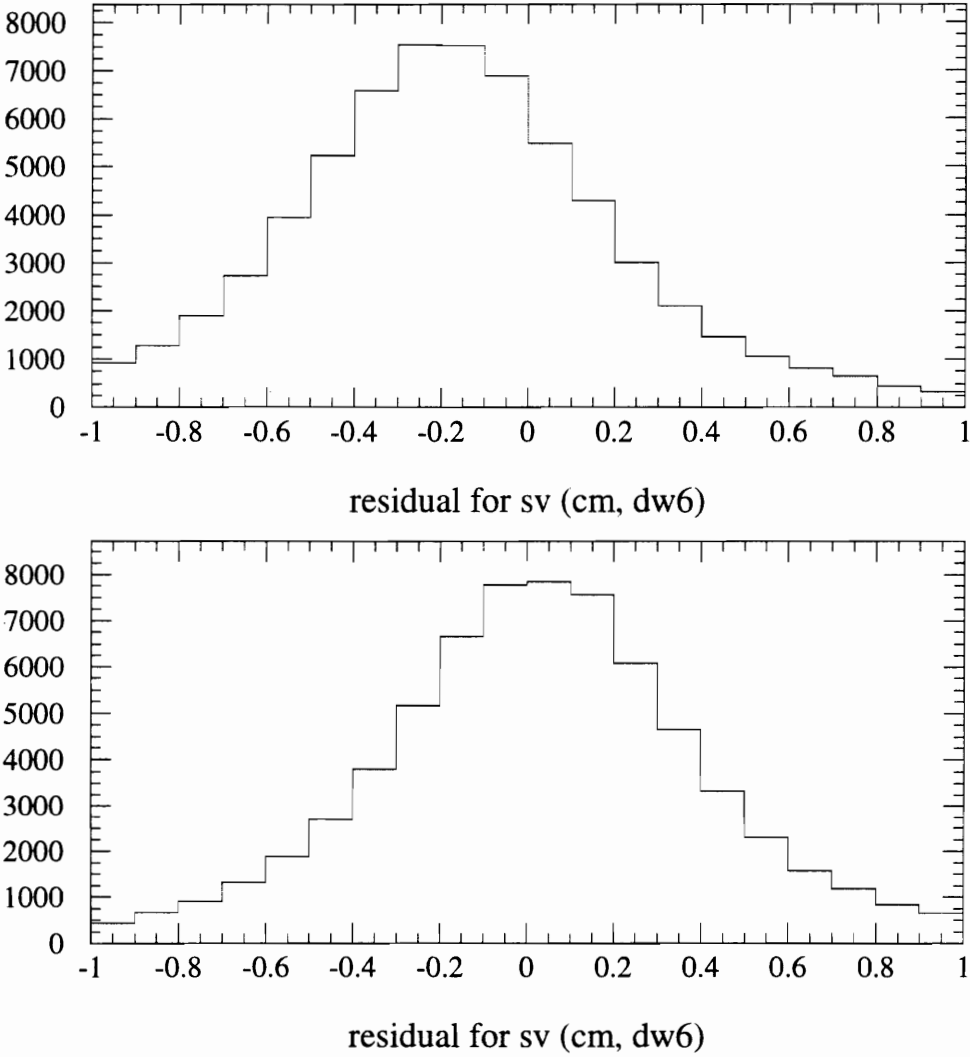


Figure 34: The side-fit residual distributions of Dwarf 6 cathodes before (top) and after (bottom) Z alignment.

chamber provided two z positions: z_{in} , the intercept between the inner cathode and the anode, and z_{out} , the intercept between the anode and the outer cathode. The low efficiency near the garlands led to holes in the z_{in} and z_{out} frequency distributions centered on the garland z locations. The cathode slopes were fine tuned to bring the garlands' Δz separations into agreement with the measurements made during chamber construction.

The positron scintillators channel mapping and alignment followed the MWPC alignment. In this case, the azimuthal angle of the intersection of a reconstructed helical track with the scintillator inner radius was compared with the azimuthal angle of the nearest scintillator having a TDC hit (within ± 5 scintillators). In a scatterplot of these two azimuthal angles, a narrow diagonal band corresponds to correctly mapped scintillators, while deviations from this diagonal band indicate errors in the database map.

The scintillator alignment (relative to the previously aligned MWPCs) is performed by making a linear least-square fit to these diagonal bands. The intercept of the best fit line gives the global offsets of the upstream and downstream scintillator barrels (see Fig. 35).

4.2.2 Spectrometer Detection Efficiency

With the correct mapping and alignment, we determined the detection efficiencies of the positron wire chambers. We used Michel decay tracks with a vertical target for this purpose and categorized the data by the number of helix loops (which is correlated with both the dip angle and p_z in this geometry). In measuring the efficiency of a particular MWPC, the track reconstructed from hits in the other chambers was projected into the MWPC in question.

A window was opened around each projected crossing point to look for one or more hits. If hits were found in the window, the central anode (or cathode) was said to be efficient for this crossing; otherwise it was inefficient. The efficiency of each detector element was given by the ratio of the number of efficient crossings to the number of all crossings.

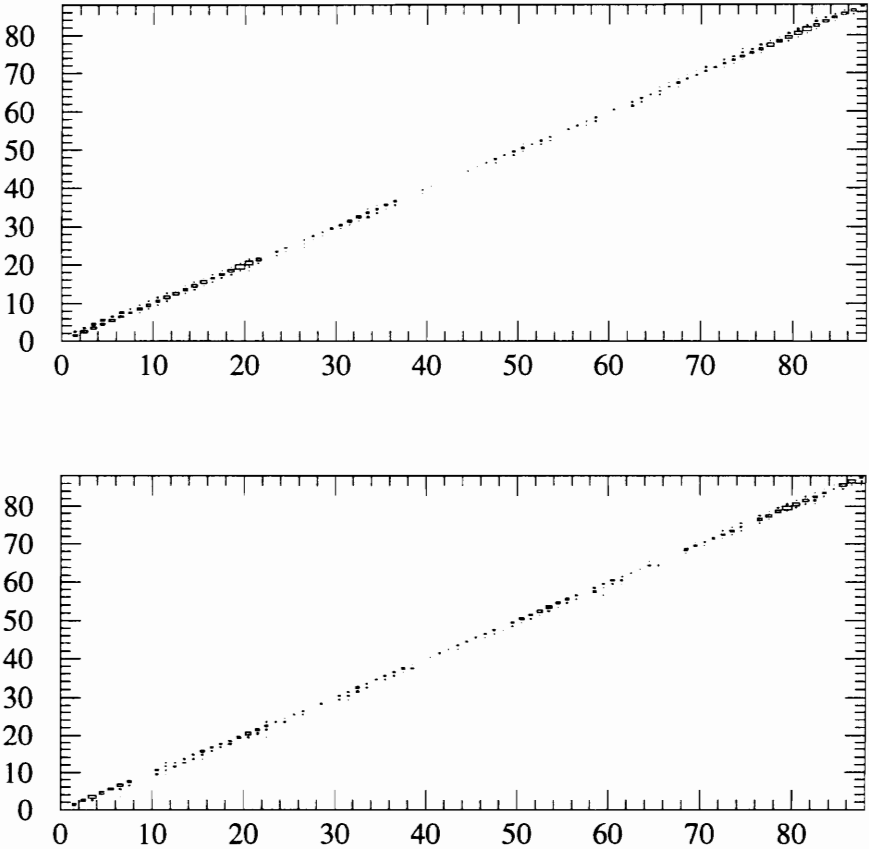


Figure 35: The scintillator map scatterplots for upstream (top) and downstream (bottom). The azimuthal angles are measured by scintillator number (1 to 88).

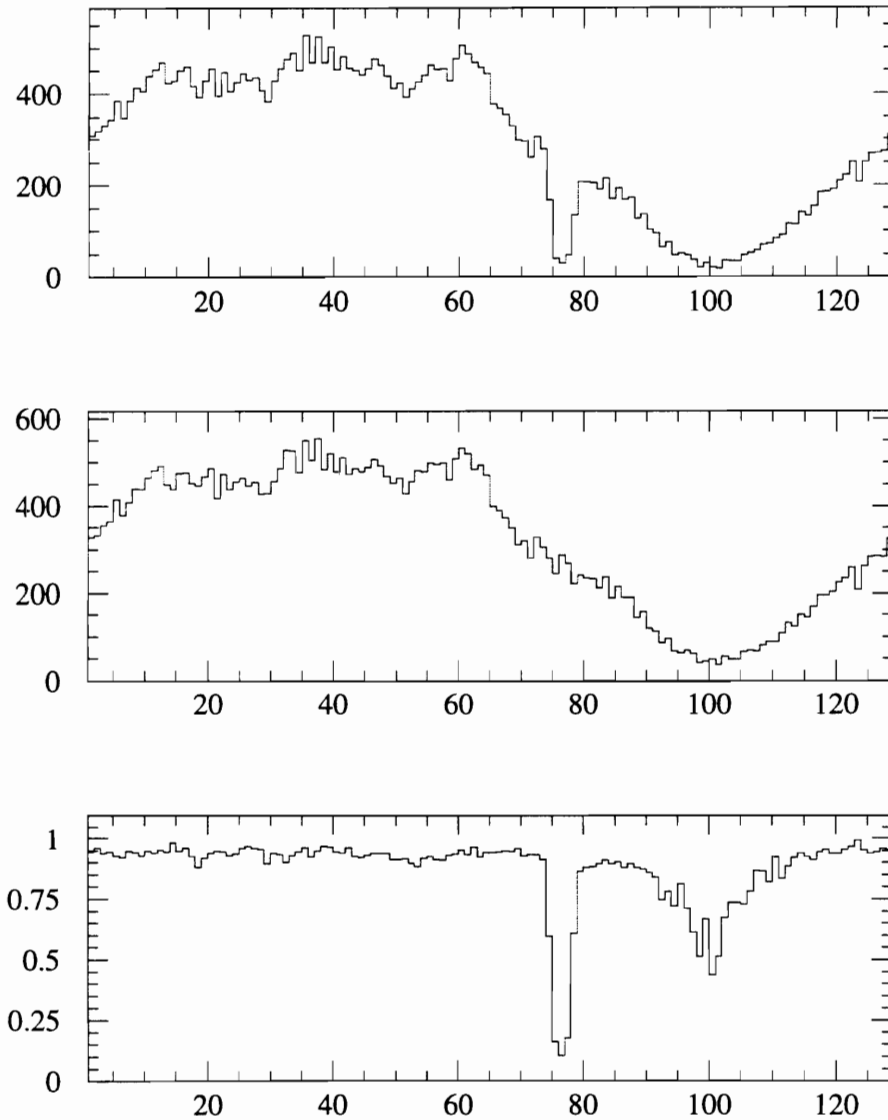


Figure 36: For dwarf 5 upstream inner cathodes, the real cathode hit distribution (top), the expected cathode hit distribution from projected tracks (middle), and the efficiency (bottom) which is the ratio of the top two histograms.

Table 22: Positron MWPCs efficiencies

Chamber	Anode	Upstream inner cathode	Upstream outer cathode	Downstream inner cathode	Downstream outer cathode
Sw	92.9±0.2	83.8±0.2	83.1±0.2	87.5±0.2	86.0±0.2
Dw1	95.9±0.4	90.3±0.2	89.5±0.2	81.3±0.3	74.6±0.3
Dw2	90.8±0.2	66.5±0.2	65.6±0.2	57.7±0.3	69.5±0.3
Dw3	89.1±0.5	94.7±0.1	93.3±0.1	-	-
Dw4	82.2±0.3	78.6±0.1	50.4±0.2	82.2±0.2	71.3±0.2
Dw5	95.4±0.4	90.8±0.1	91.3±0.1	94.2±0.1	90.6±0.2
Dw6	63.4±0.5	67.1±0.2	72.5±0.2	71.5±0.2	78.8±0.2
Dw7	-	-	-	-	-

The anode efficiency was measured using zero loop events (to avoid double hits on the same anode wire) and the cathode efficiency by one-or-more loop events. (The integer loop number refers to the number of *complete* traversals of the track’s projected circular orbit between the decay point and the impact on the scintillator barrel.) The size of the window, ± 5 wires, was determined by the multiplicities of chamber hits which depended strongly on the incident angle, by the lever arm on the track projection into the test chamber, and by a study of simulated data with 100% efficiencies. Table 22 gives the average efficiencies of positron MWPCs in the 1992 MEGA data taking stage. The low efficiencies of dwarf 6 were due to higher discriminator thresholds (to avoid preamplifier noise). The dwarf 3 downstream cathodes were turned off because of uncontrollable preamplifier oscillation. Dwarf 7 was turned off because of a broken anode.

The efficiencies of the positron scintillators were analyzed using Michel decay data triggered by a signal in the large unstriped central Snow White cathode (the “Snow White trigger”). Reconstructed tracks were projected into the scintillator barrel; a 5 scintillator wide window was opened to search for hit scintillators. As

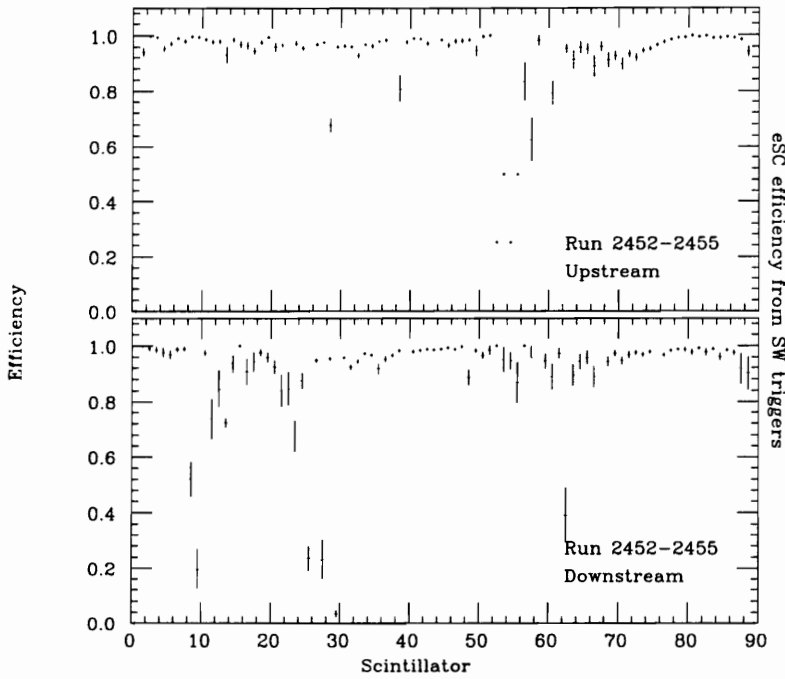


Figure 37: Efficiency of each positron scintillator. Channels with large error bars were poorly illuminated by *reconstructed tracks* due to chamber inefficiencies.

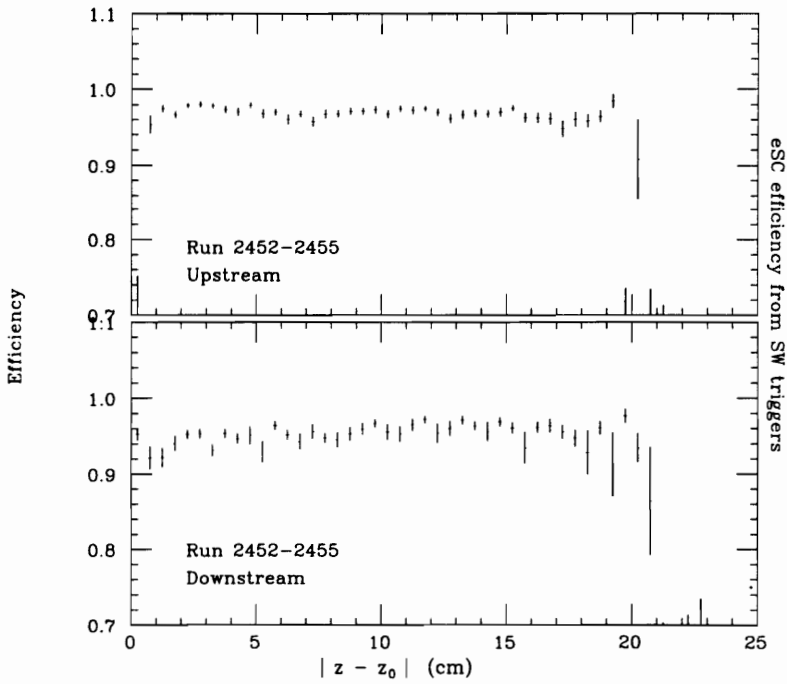


Figure 38: Efficiency of all scintillators in z .

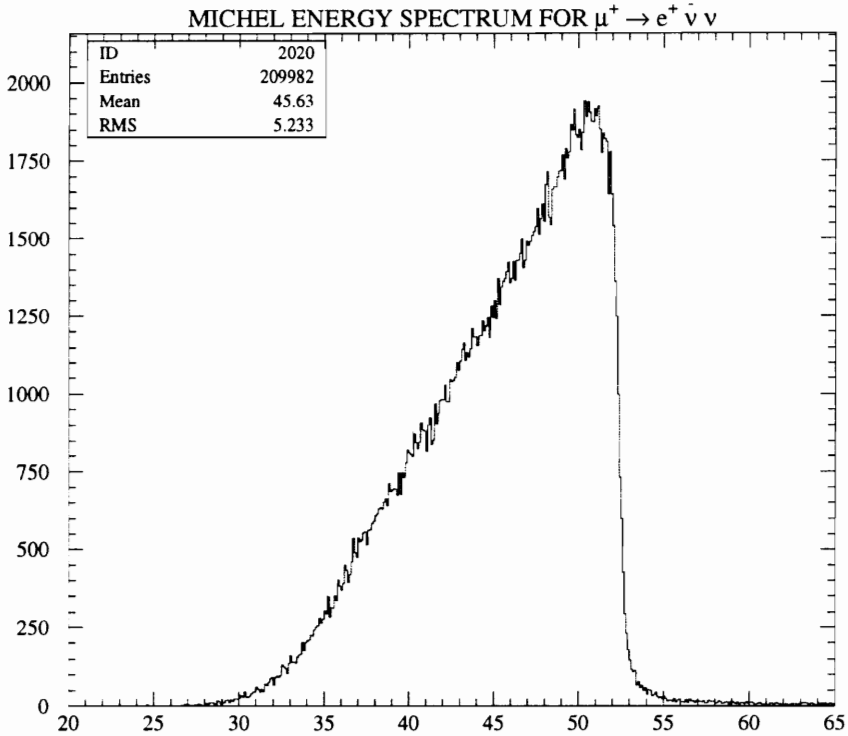


Figure 39: The Michel decay positron energy spectrum

for the chambers, the efficiency of the central scintillator in each such window was determined by the ratio of the number of intersections with hits in the window to the number of all intersections.

Fig. 37 shows the efficiency for each scintillator, while Fig. 38 shows the combined efficiency of all scintillators as a function of the axial distance from the end of the scintillator barrel that is nearest the target. The average efficiencies are 0.985 ± 0.001 for upstream and 0.948 ± 0.002 for downstream.

4.2.3 Positron Energy Spectrum

The momentum of a reconstructed track can be calculated from the track parameters and the values of the magnetic field. The transverse and longitudinal components of the momentum are

$$p_r = B \cdot c \cdot R \quad (75)$$

$$p_z = B \cdot c \cdot s \quad (76)$$

where B is the magnetic field in kilogauss, c is the speed of light in m/ns, R is the radius in cm of the end view of the helix, and s is the slope in cm/radian of the helix side view. Fig. 39 shows the energy spectrum of all reconstructed Michel positrons emerging from muon decays on the slanted target. The spectrum shape is distorted at lower energies by the nonuniform acceptance of the positron spectrometers (see Fig. 40). The theoretical spectrum (non-radiative) rises to a maximum at a positron energy of 52.83 MeV, then suddenly fall to zero for larger energies. In practice, energy loss and multiple scattering, as well as finite chamber position resolution, result in a shift and smearing out of this edge. The energy resolution near 52.8 MeV can be characterized by the energy interval over which the spectrum falls from 90% to 10% of its peak intensity.

The equivalent energy resolution for monoenergetic positrons is extracted from the data near the Michel spectrum endpoint using a special fitting program written by G. Hogan.

Table 23 lists the results of this fit. From Table 23, it is clear that the values of the centroids for downstream-going tracks are systematically larger than for upstream-going tracks. This is primarily caused by nonuniformity in the solenoidal magnetic field (not included in the track reconstruction).

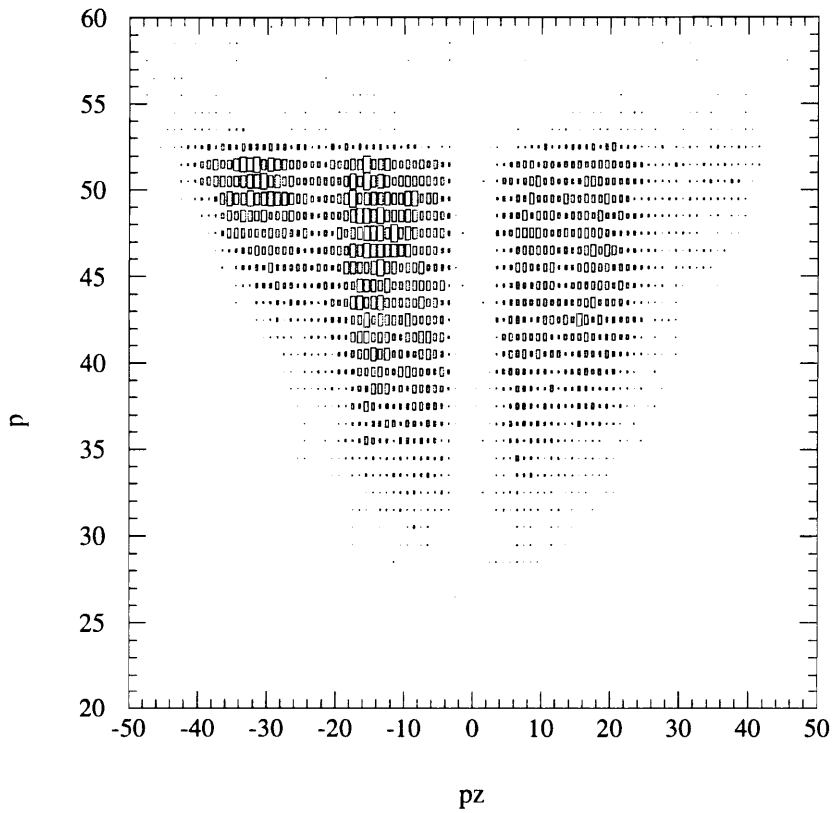


Figure 40: The Michel decay positron momentum vs longitudinal momentum for decays from the slanted MEGA target.

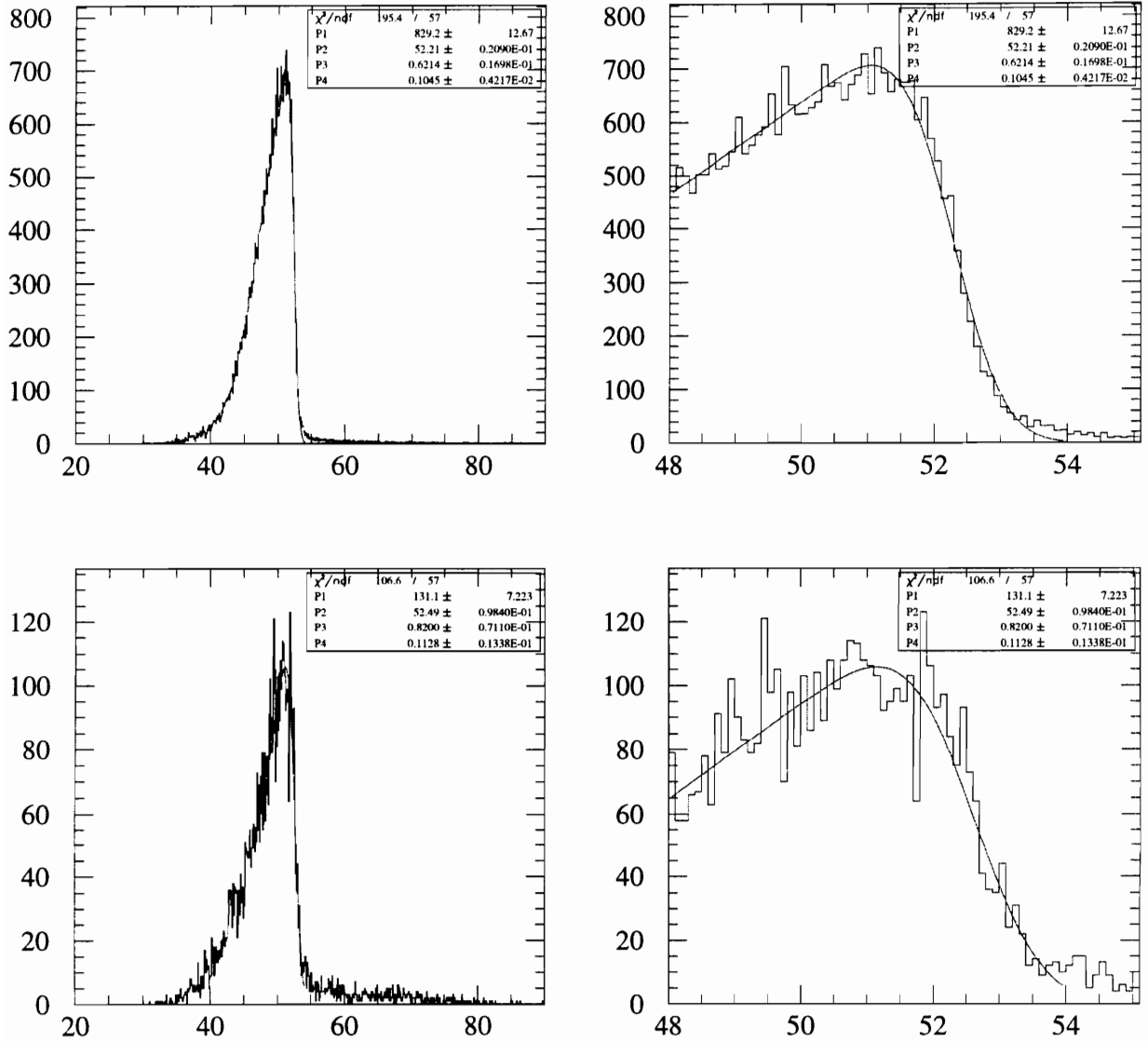


Figure 41: The Michel energy spectrum for zero loop tracks going upstream (top) and downstream (bottom). The right hand histograms show an expanded energy scale near the Michel endpoint; the curves are the best fit to the data.

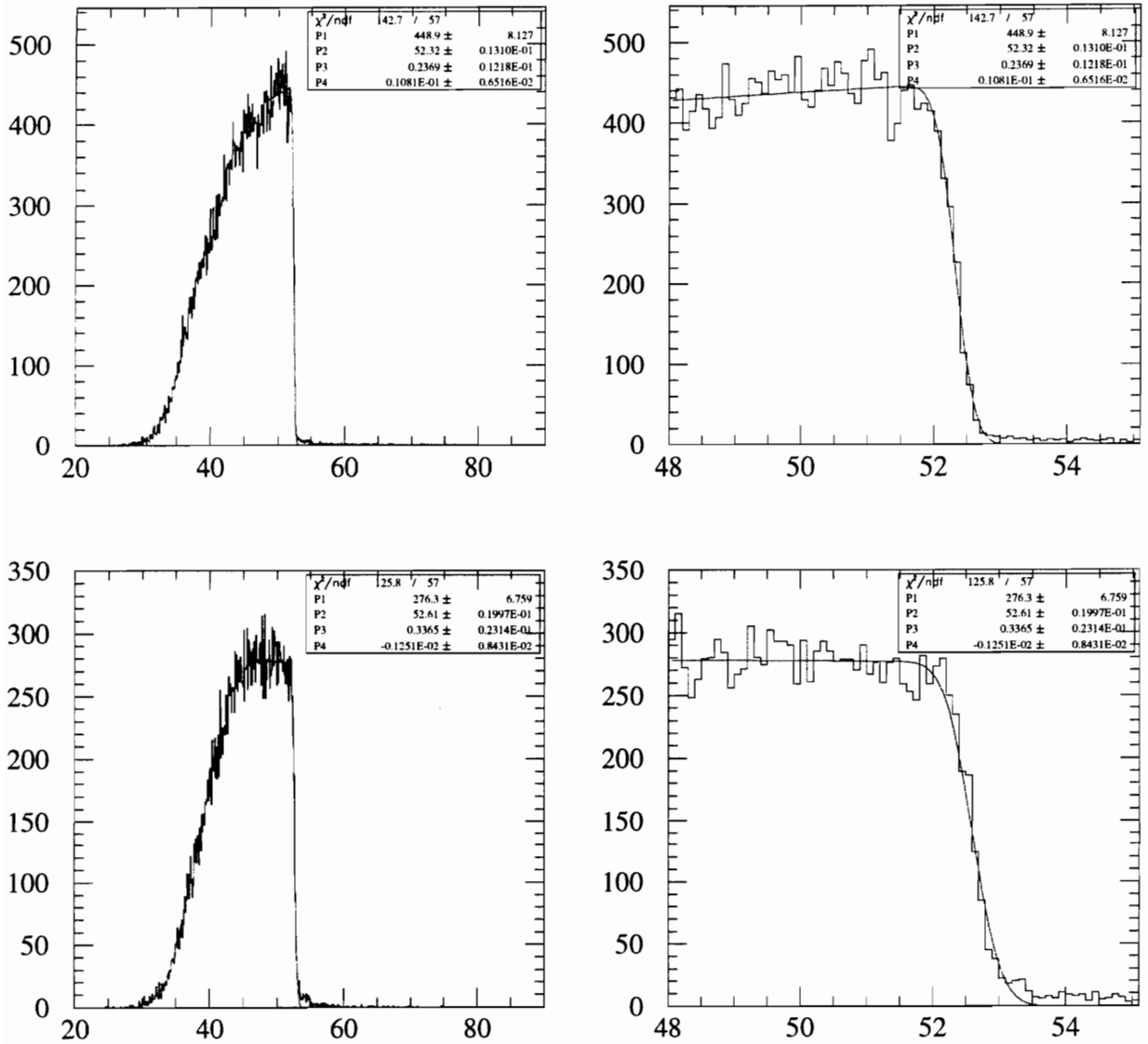


Figure 42: The Michel energy spectrum for one loop tracks going upstream (top) and downstream (bottom). The right hand histograms show an expanded energy scale near the Michel endpoint; the curves are the best fit to the data.

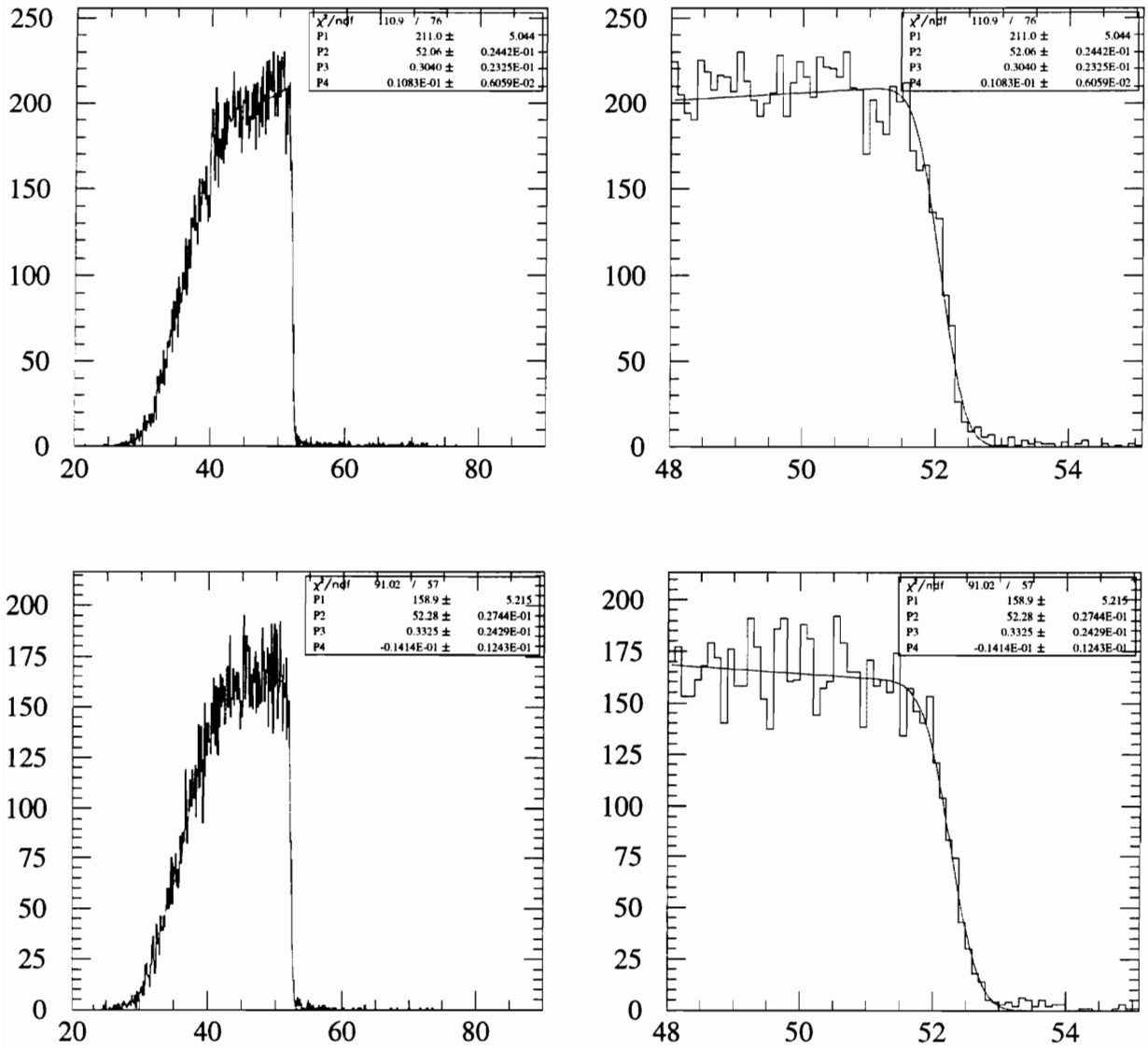


Figure 43: The Michel energy spectrum for tracks with 2 or more loops going upstream (top) and downstream (bottom). The right hand histograms show an expanded energy scale near the Michel endpoint; the curves are the best fit to the data.

Table 23: Energy endpoint centroid and spread of Michel-decay positrons

	Loop number	Centroid (MeV)	Δ (MeV)
Up- stream	0	52.21±0.02	0.62±0.02
	1	52.32±0.01	0.24±0.01
	2+	52.06±0.02	0.30±0.02
Down- stream	0	52.49±0.10	0.82±0.07
	1	52.61±0.02	0.34±0.02
	2+	52.28±0.03	0.33±0.02

4.3 Photon Spectrometer Response

4.3.1 Photon Energy Calibration

Ideally, the photon energy resolution should be measured with a monochromatic source of 52.8 MeV photons. Photons with similar energies can be generated from the process $\pi^0 \rightarrow \gamma\gamma$. A π^- beam is converted to π^0 by the charge exchange reaction, $\pi^- p \rightarrow \pi^0 n$, in a solid cylindrical CH_2 target. The π^0 then decays in flight into two high energy photons. Because of the pion's motion in the lab frame, these photons are not monoenergetic nor back-to-back. However, the photon energies are correlated with their opening angle. At the minimum value of 156.5° , the photons have equal energy ($E_\gamma = 68.94$ MeV), and at 180° (back-to-back), the photon's energy sharing is most asymmetric ($E_{\gamma 1} = 54.92$ MeV and $E_{\gamma 2} = 82.96$ MeV). The low energy photon in the latter case is very close to the desired 52.8 MeV, and therefore is used to calibrate the photon spectrometer energy response resolution. A typical $\pi^0 \rightarrow \gamma\gamma$ event from 1993 is shown in Fig. 44. Here, the high energy photon is detected in the outermost layer of the photon spectrometer and the low energy photon is detected on the innermost layer. (The π^0 trigger ignores events where both photons convert in

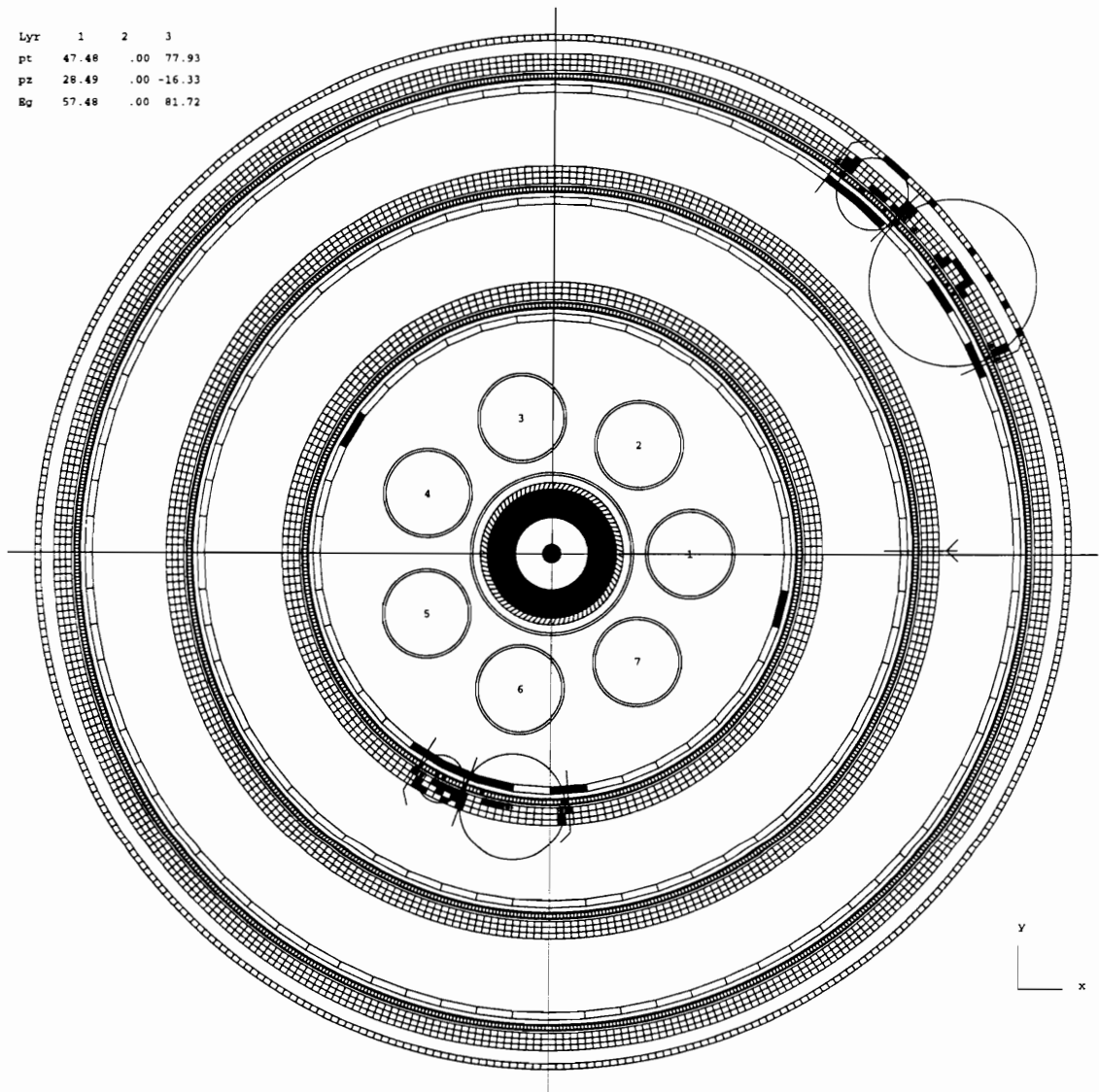


Figure 44: A typical $\pi^0 \rightarrow \gamma\gamma$ event from 1993. The high (low) energy photon is detected in the outermost (innermost) per spectrometer.

the same layer, to avoid problems with the multiplexing of the photon spectrometer signals.) Since the pion data taken in 1992 had limited statistics, the 1993 pion data were used to determine the photon energy response. Seven million events were used in this analysis[49].

Fig. 45 shows the $\gamma\gamma$ opening angle distribution of 1993 pion data (top) and Monte Carlo events (bottom). The Monte Carlo distribution shows a characteristic edge near 155° that corresponds to the minimum value of opening angle, with very few events below 150° (mainly due to reconstruction errors). On the other hand, the 1993 data spectrum has a similar distribution for opening angles above 155° but, in addition, has a broad background extending from 90° to 180° . Most of the background events were found to have come from π^- -carbon interactions in the momentum degrader that was located several centimeters upstream of the pion target. Because of the poor photon direction resolution, the decay point of these events was incorrectly traced back to the target rather than the degrader. (This background was eliminated in the 1994 runs by taking an additional measurement to subtract the contribution from these pion-carbon interactions.)

The photon energy from the pion data analysis is correlated with the opening angle, as illustrated in Fig. 46 for Monte Carlo data with no uncertainty in the drift distances. This correlation introduces a dependence of the photon energy near 55 MeV—and therefore of the apparent energy resolution—on the opening angle resolution. This effect is unfolded to extract the true photon energy resolution.

The unfolded energy spreads Δ are summarized in the third and fourth columns of Table 24. The data and Monte Carlo are in good agreement. The energy resolution σ of the pair spectrometers for a 52.8 MeV photon, shown in the last column of Table 24, is obtained by scaling the measured pion decay photon energy spread by a factor of 0.72 ± 0.08 . This factor was determined by simulating both pion decay events and mono-energetic 52.8 MeV photons, then comparing the extracted widths: spread Δ and resolution σ , respectively, as shown in the fourth and fifth columns of Table 24.

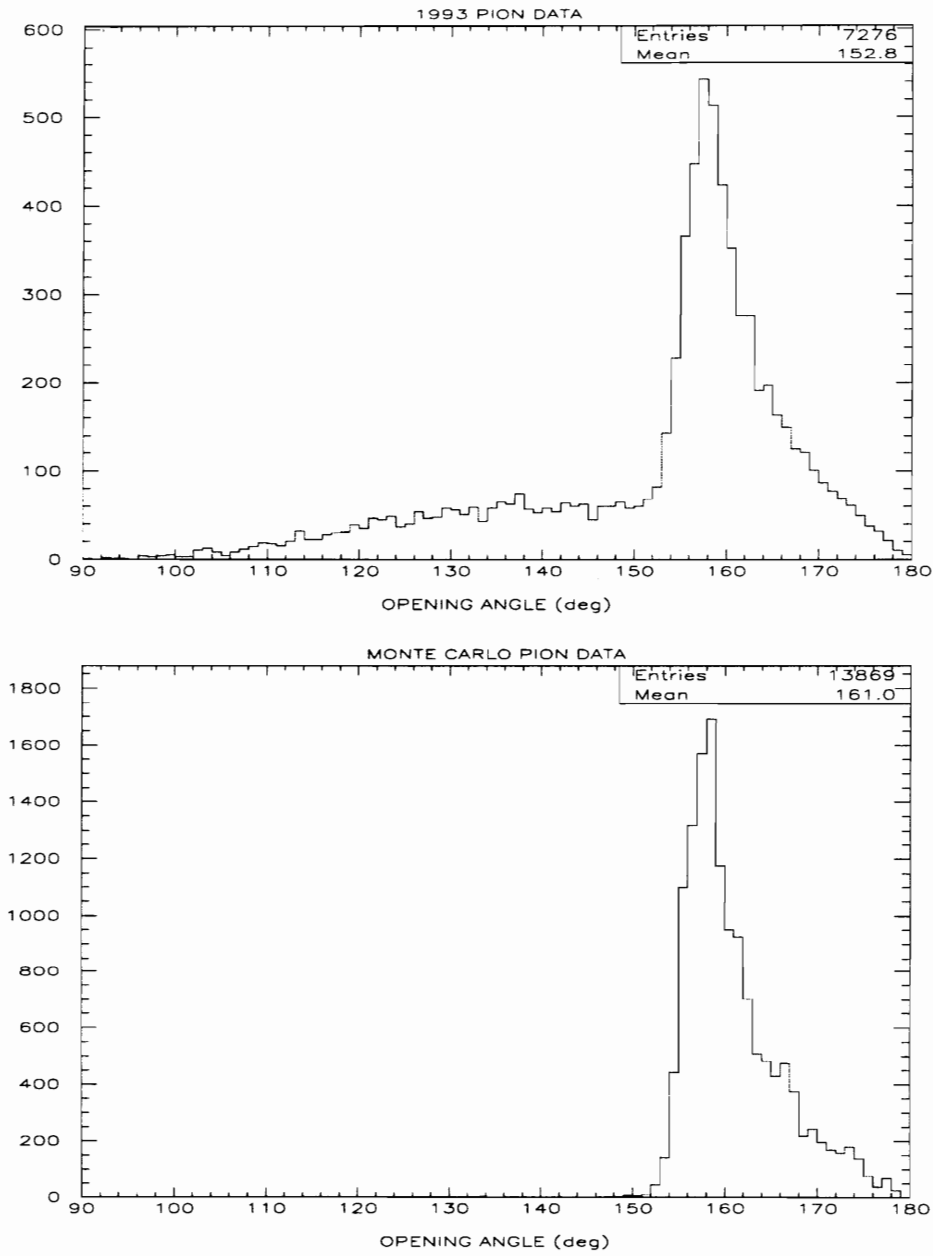


Figure 45: Opening angle between the photons from $\pi^0 \rightarrow \gamma\gamma$ for 1993 data (top) and Monte Carlo events (bottom).

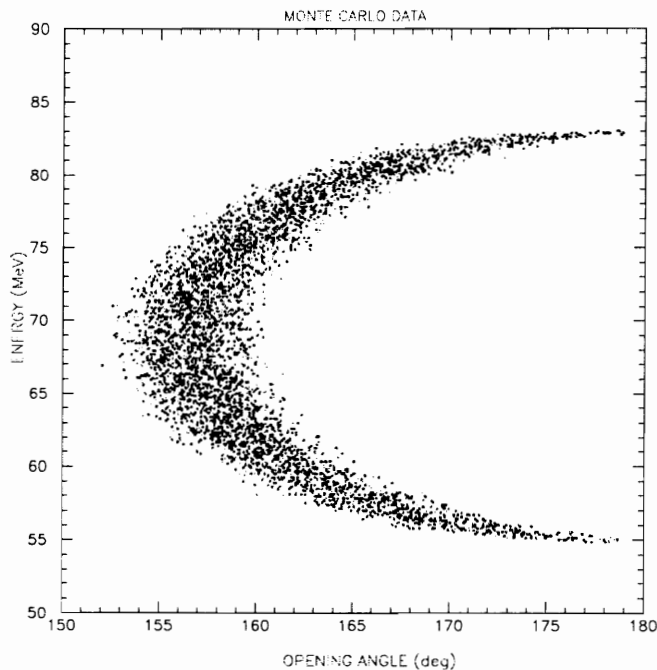


Figure 46: True Monte Carlo energy versus the $\gamma\gamma$ opening angle for photon from $\pi^- p \rightarrow \pi^0 n$ followed by $\pi^0 \rightarrow \gamma\gamma$.

Table 24: Energy spread of photons from Pion decay data after unfolding the correlation of energy with opening angle, and energy resolution of 52.8 MeV photons.

Converter	$\Theta_{\gamma\gamma}$ for $\gamma\gamma$ pairs	Δ/E (%) 1993 data	Δ/E (%) Monte Carlo	σ/E (%) Monte Carlo	σ/E (%) predicted for data
Outer	$> 173.5^\circ$	2.9 ± 0.5	2.7 ± 0.1	2.0 ± 0.3	2.1 ± 0.4
Inner	$> 170.0^\circ$	5.8 ± 0.9	5.2 ± 0.4	3.6 ± 0.5	4.2 ± 0.8

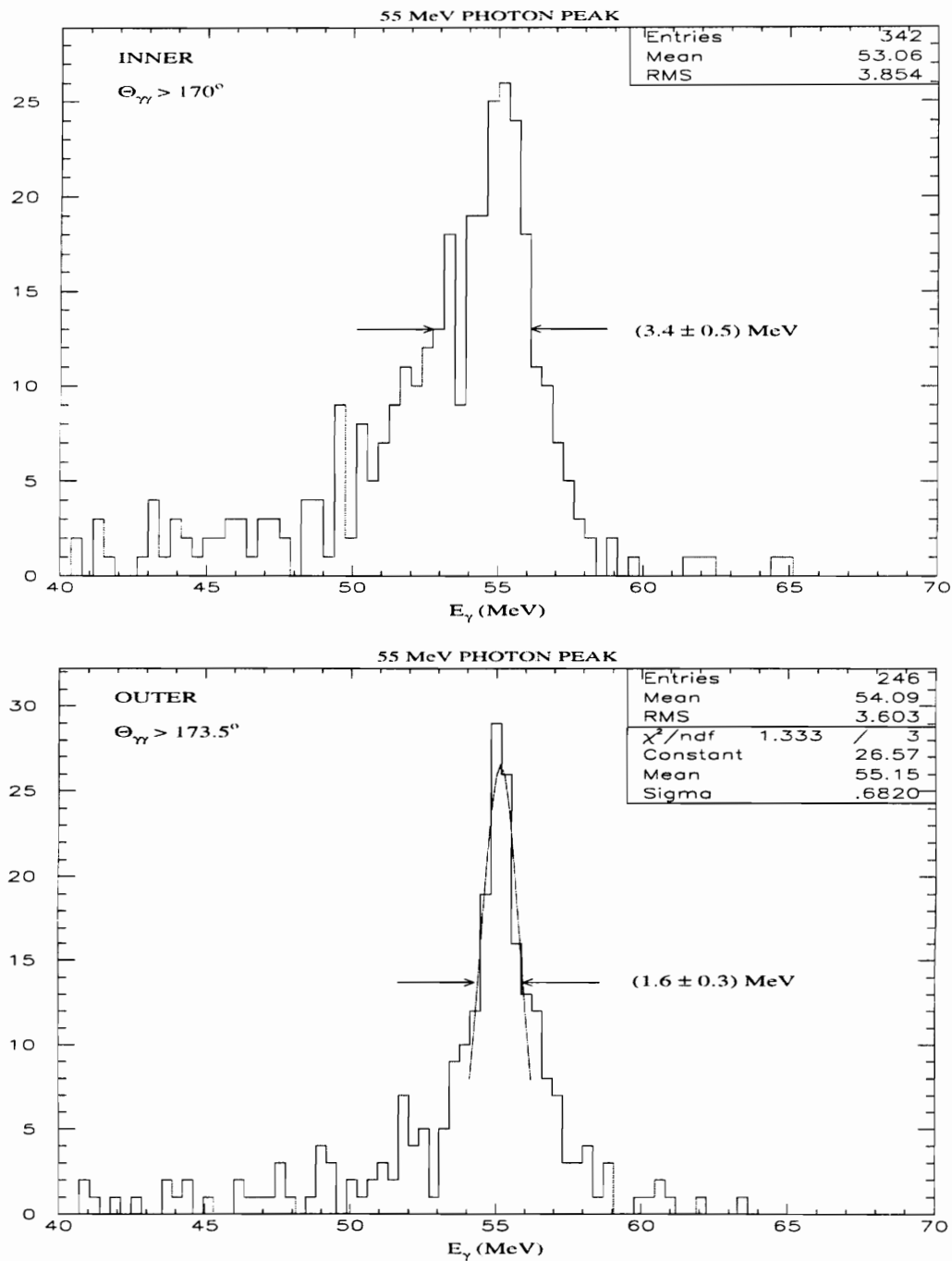


Figure 47: 55 MeV photon energy peak for inner (top) and outer (bottom) conversion events.

4.4 Target

Knowledge of the muon decay point on the thin slanted target is critical for the identification of the decay $\mu \rightarrow e\gamma$, since it affects two important quantities used to discriminate against backgrounds: the $e\gamma$ opening angle at the decay point, and the relative timing extrapolated back to the decay point. Uncertainty in the μ decay point is directly correlated with uncertainty in the positron direction at the decay point, and therefore in the $e\gamma$ opening angle determination. Also, the possibility of more than one intersection of the position helix with the slanted target plane makes it possible to misassign the decay point and thereby miscalculate the $e\gamma$ relative timing.

In 1992, we took some data with a special “big hole” target to study the decay point resolution. This target had the same geometry as the MEGA target except for a different orientation and the presence of a rectangular hole in the center of the target, 10 cm along the major axis and 2 cm along minor axis. Michel decay events were triggered by a hit in any positron scintillator. The beam rate was reduced to ensure at most one positron track segment per trigger. In the following sections, we present the analysis of these data and extract the muon decay point resolution and positron direction resolution at the decay point.

4.4.1 Muon Decay Point Resolution

Since the MEGA targets—including the “big hole” target—are passive, the decay point is located by reconstructing the positron track, then determining the correct crossing point of this helix with the target plane. The algorithm of finding the decay point resolution is as follows:

1. Find all crossing points of the reconstructed helix with the target plane.
2. Determine which of these crossing points is the μ decay point.
3. Translate the decay points from the experimental frame to the local target frame, then histogram them in a two dimensional scatter plot.
4. Project a slice of this scatter plot on to the major or minor axis of the target.

5. At the edge of the target hole in these projected histograms, calculate the distance interval over which the intensity changes from 10% to 90% to get a measure of the μ decay point resolution.
6. Convert the above measure of resolution to equivalent FWHM for decays originating from a single point.

For steps 1-3, the target plane location and orientation is defined by four parameters: the three components of the normal vector, and the target axial offset z_{off} at $x = y = 0$. The normal vector to the plane of the target is $\hat{n} \equiv (0, 1, 0)$ in the (u, v, w) target frame coordinates if the target is in the (u, w) plane. In the experimental frame (x, y, z) coordinates, this normal vector has components

$$\hat{n} = (n_x, n_y, n_z) = (\sin \xi \cos \delta, \cos \xi \cos \delta, \sin \delta) \quad (77)$$

where ξ is rotation angle of the normal vector in the (u, v) plane and δ is the second rotation angle in the (v, w) plane that couples these two coordinate frames. Then we have the equation of target plane:

$$n_x x + n_y y + n_z (z - z_{off}) = 0 \quad (78)$$

or, equivalently,

$$n_x x + n_y y + n_z z = K_0 \equiv n_z z_{off} \quad (79)$$

The helical track is given by

$$x = x(\omega) = x_c + R \cdot \cos \omega \quad (80)$$

$$y = y(\omega) = y_c + R \cdot \sin \omega \quad (81)$$

$$z = z(\omega) = z_0 + s \cdot (\phi_0 - \omega) = a \cdot \omega + b \quad (82)$$

where $a = -s$ and $b = s \cdot \phi_0 + z_0$. If we substitute equations (80–82) in (79), obtain

$$n_x R \cos \omega + n_y R \sin \omega = K_0 - K - n_z a \omega \quad (83)$$

where $K = n_x x_c + n_y y_c + n_z b$ and $\omega = (z - b)/a$.

The winding angle of the helix-target crossing points can be extracted from equation 83. Writing $\beta = \omega - \omega_o$ with

$$\omega_o = -\tan^{-1}\left(\frac{n_x}{n_y}\right), \quad (84)$$

we obtain the following relation for the intersection angle β :

$$\sin \beta = G_0 - H_0 \beta \quad (85)$$

where G_0 and H_0 are given by:

$$G_0 = -\frac{1}{\sqrt{n_x^2 + n_y^2}} [n_z a \omega_o + n_x x_c + n_y y_c + n_z (b - z_{off})] \quad (86)$$

$$H_0 = \frac{n_z a}{R \sqrt{n_x^2 + n_y^2}} \quad (87)$$

Since $-1 \leq \sin \beta \leq 1$, the physical solutions from equation (85) should be bounded between $\beta_< = G_0 + 1/H_0$ and $\beta_> = G_0 - 1/H_0$. If we find the n roots of equation (85) within these bounds, then the crossing point for the i^{th} root β_i is given by

$$x_i = x_c + R \cos(\beta_i + \omega_o) \quad (88)$$

$$y_i = y_c + R \sin(\beta_i + \omega_o) \quad (89)$$

$$z_i = a(\beta_i + \omega_o) + b \quad (90)$$

with the requirement that $r_i = \sqrt{x_i^2 + y_i^2}$ be smaller than the radius of the enclosing cylindrical target bag.

There are two methods to decide which of these crossings is the μ decay point. In the first method used by the MRC reconstruction program, the two intersections of the reconstructed helix and target bag p_1 and p_2 that immediately precede the “earliest” chamber hit on the track are determined. The decay point is then assigned to be the crossing point of the helix with the target plane that is located between p_1 and p_2 . The shortfall of this method is that if the first dwarf hit is not present due to chamber inefficiency or dead wires, then wrong helix-target intersection will be chosen for the decay point. Also, there is still an ambiguity in the 25% of cases where there are two helix-target intersections between p_1 and p_2 . These ambiguous-crossing are discarded. The second method, employed by the ERC reconstruction program, uses the same information and philosophy to determine the decay point but differs in the programming details. It also suffers from the same potential pitfalls and the double-crossing ambiguity.

Cuts are employed to raise the quality of the final sample of reconstructed tracks. (1) The probabilities of the χ^2 for both end view and side view fits must be larger than 5%. (2) The number of points used in the side view fit must be larger than three. (3) A unique crossing point of the track with target plane in the first loop is required. This criterion was defined in the previous paragraph. (4) Tracks that are nearly tangential to the target plane are removed. The scatterplots of the reconstructed decay points for tracks satisfying these requirement are shown in Fig. 48 and Fig. 49.

The μ decay points in the target coordinate frame can be calculated by transforming as follows:

$$\begin{pmatrix} u_i \\ v_i \\ w_i \end{pmatrix} = \begin{pmatrix} \cos \xi & \sin \xi & 0 \\ -\sin \xi \cos \delta & \cos \xi \cos \delta & -\sin \delta \\ -\sin \xi \sin \delta & \cos \xi \sin \delta & \cos \delta \end{pmatrix} \begin{pmatrix} x_i \\ y_i \\ z_i \end{pmatrix} \quad (91)$$

where ξ and δ were defined previously. The $u(w)$ axis is along the semi-major (semi-minor) axis of the ellipse, while the v axis is along the target normal. All decay points

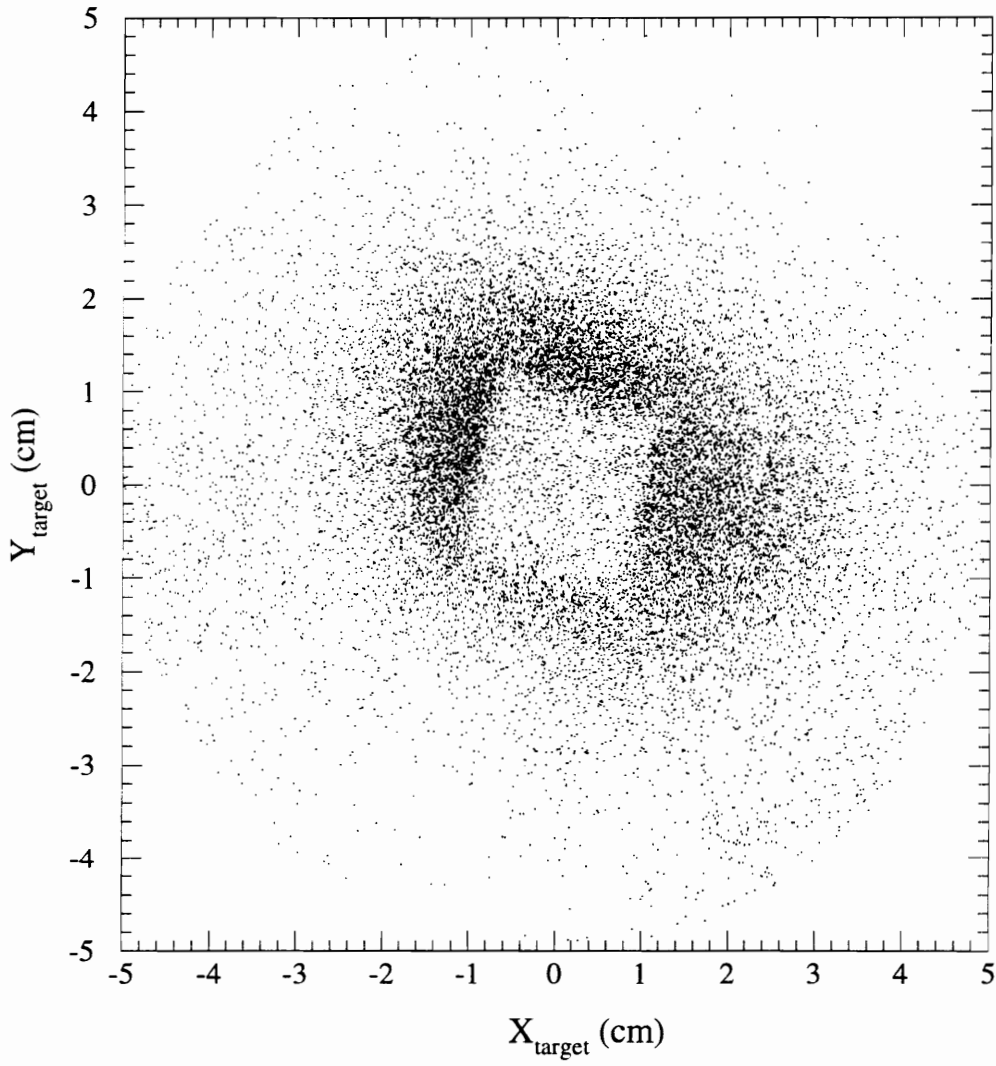


Figure 48: The projection of the muon decay points on the x-y plane at $z=0$.

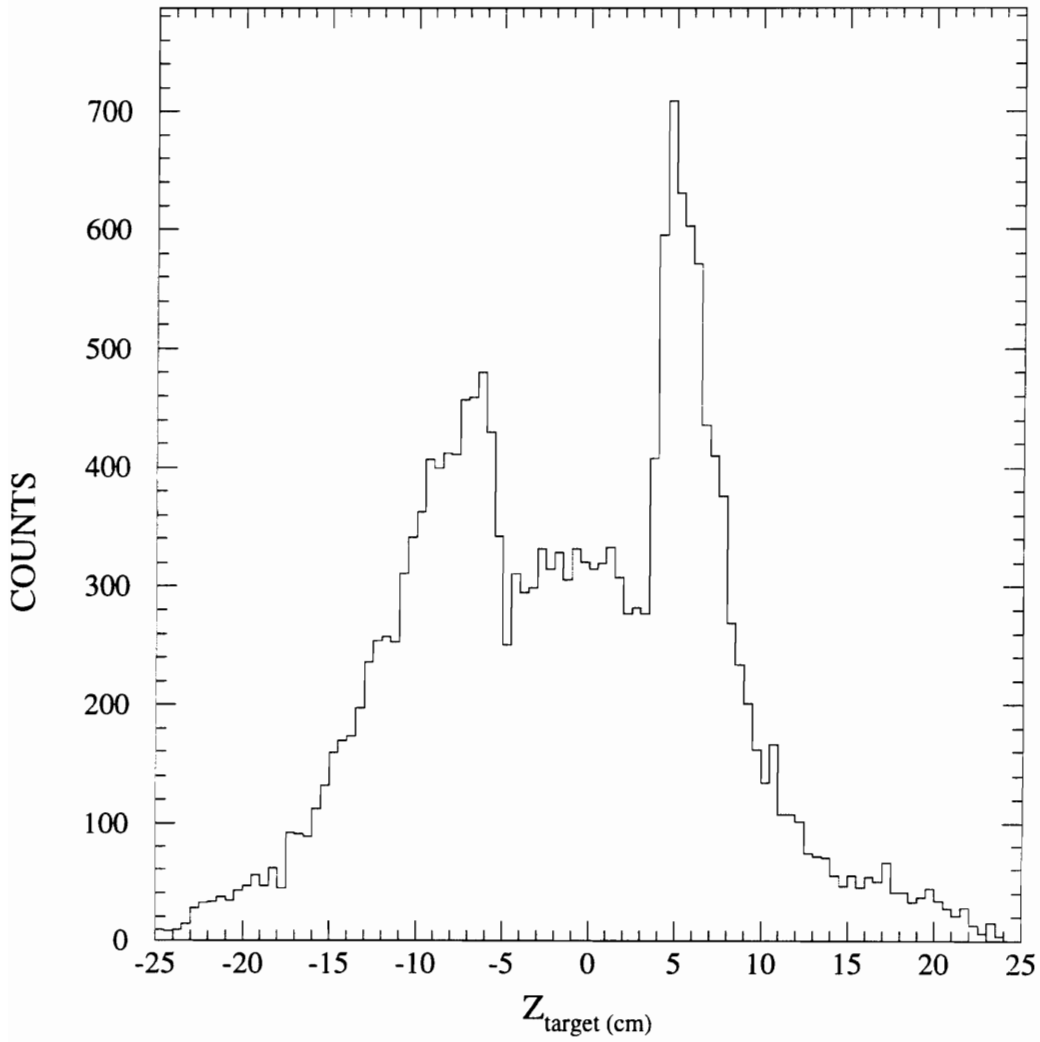


Figure 49: The z component of the reconstructed muon decay points.

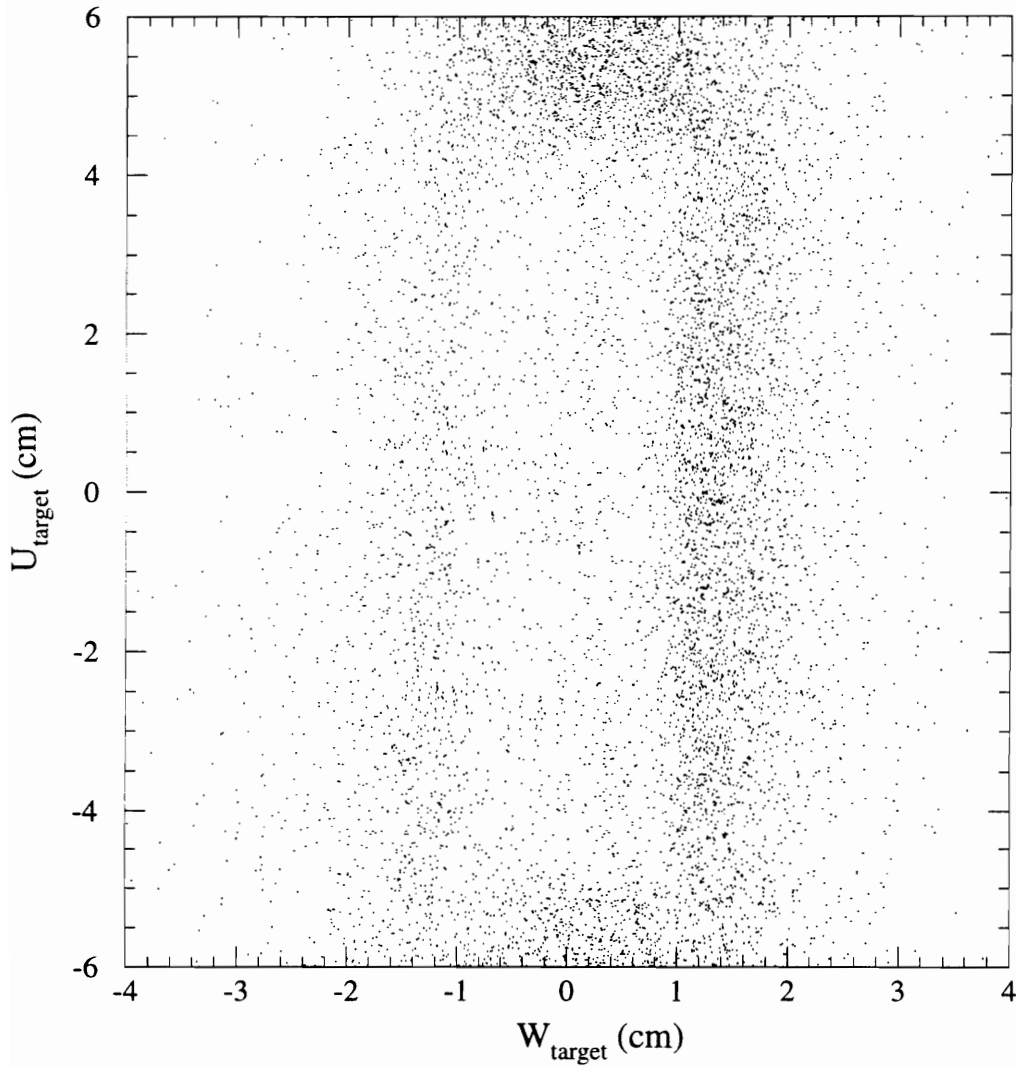


Figure 50: The μ decay points in the target plane. $u(w)$ is along the semi-major (semi-minor) axis of the target ellipse.

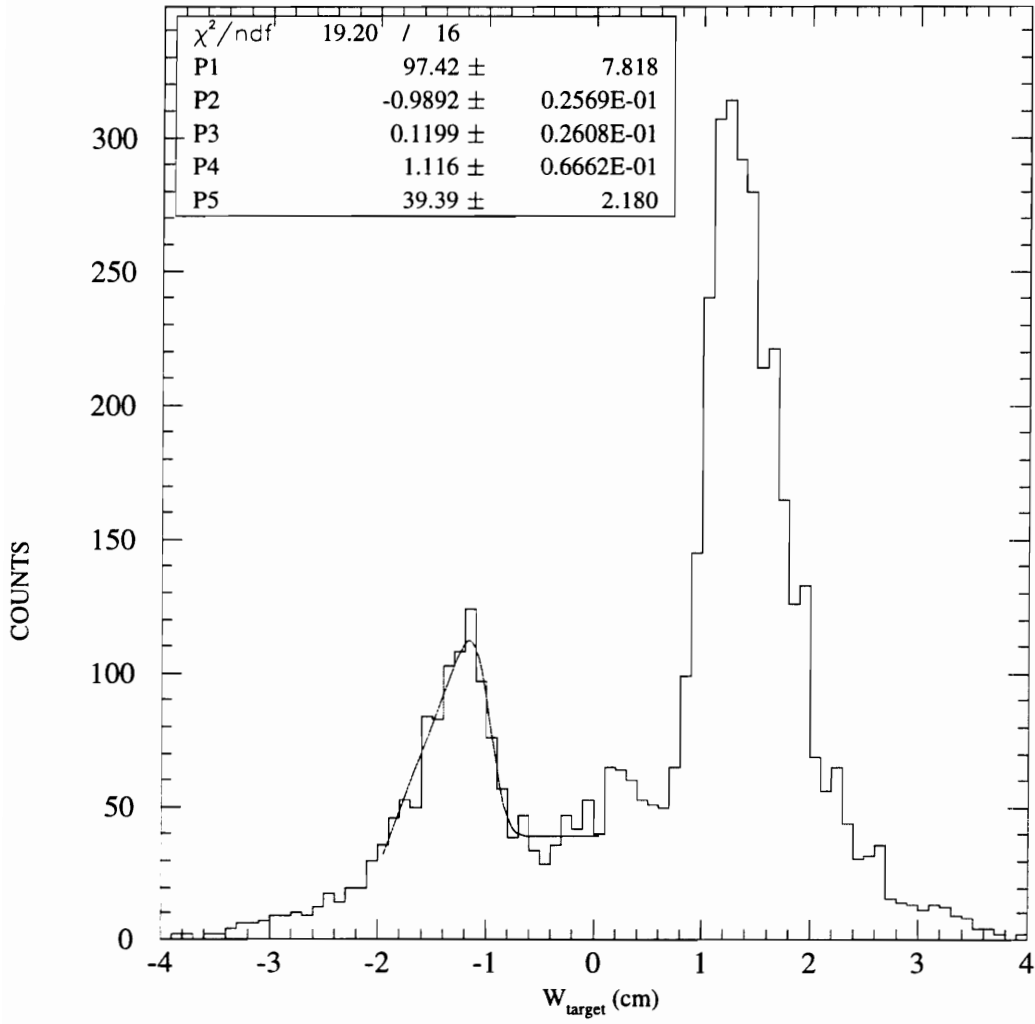
Figure 51: The projection of the μ decay points on w axis

Table 25: μ decay point resolution for Michel positrons

Location	Deviation σ	FWHM
The edge on the right	0.16 ± 0.02	0.37 ± 0.05
The edge on the left	0.12 ± 0.03	0.28 ± 0.07
Average	0.15 ± 0.02	0.35 ± 0.04

Table 26: μ decay point resolution from Monte Carlo simulation

Location	Deviation σ	FWHM
The edge on the right	0.12 ± 0.02	0.28 ± 0.05
The edge on the left	0.14 ± 0.02	0.34 ± 0.05
Average	0.13 ± 0.02	0.31 ± 0.05

have $v = 0$ by this definition. The scatter plot of u vs w for the reconstructed decay points is shown in Fig. 50. By slicing this histogram from -4 cm to 4 cm on the u axis and then projecting on to the w axis, we make a one dimensional histogram (Fig. 51) from which the decay point resolution can be derived. By fitting this histogram on both edges of the central hole, we obtain the results shown in Table 25. On average, the μ decay point resolution is 0.35 ± 0.04 cm (FWHM) for Michel positrons.

The μ decay point resolution was calculated also by using Monte Carlo simulations of Michel decays, using the practical detector performance and geometries of 1992. Analyzing these simulated events in the same way as the 1992 data, we obtain the Monte Carlo decay point resolution from Monte Carlo shown in Table 26. The scatterplot of the reconstructed decay points and the one dimensional projections for the simulated events are shown in Fig. 52—53.

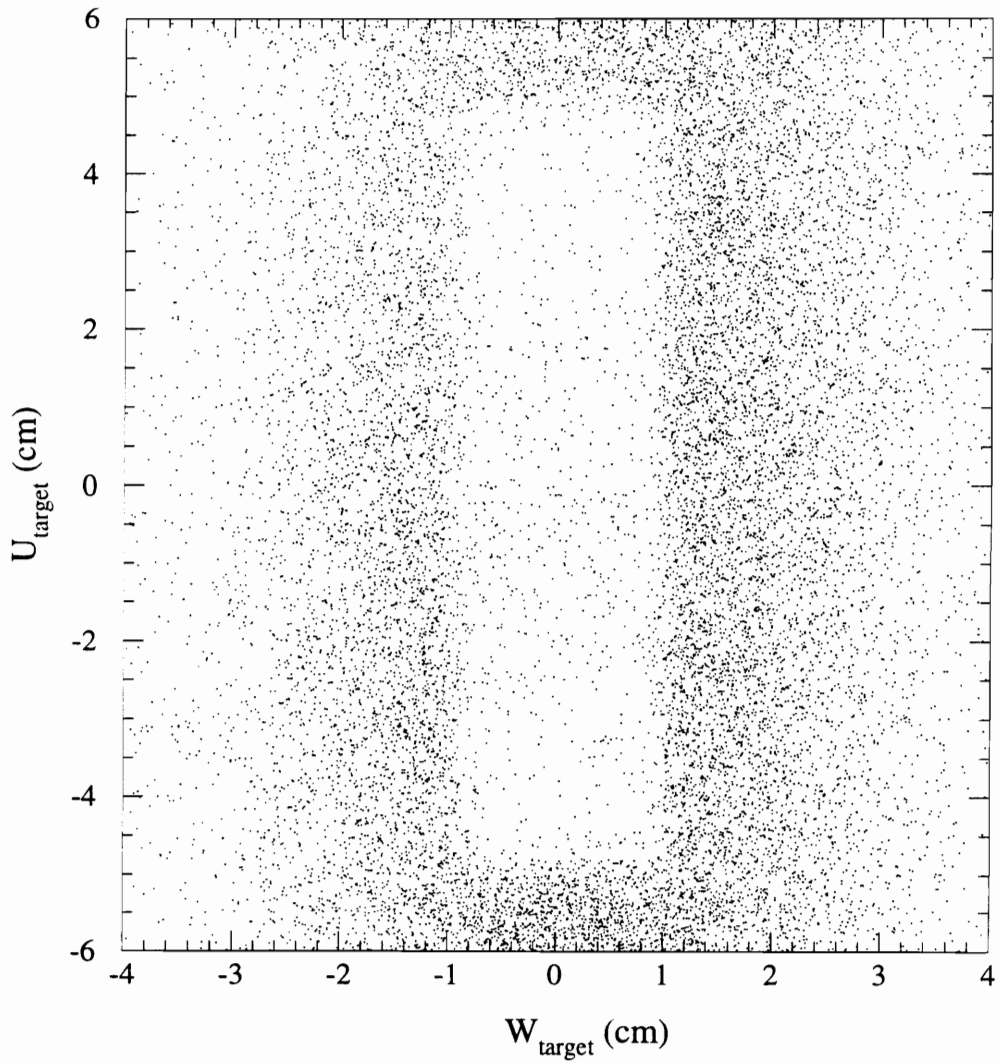


Figure 52: The μ reconstructed decay points on the target plane for simulated events.

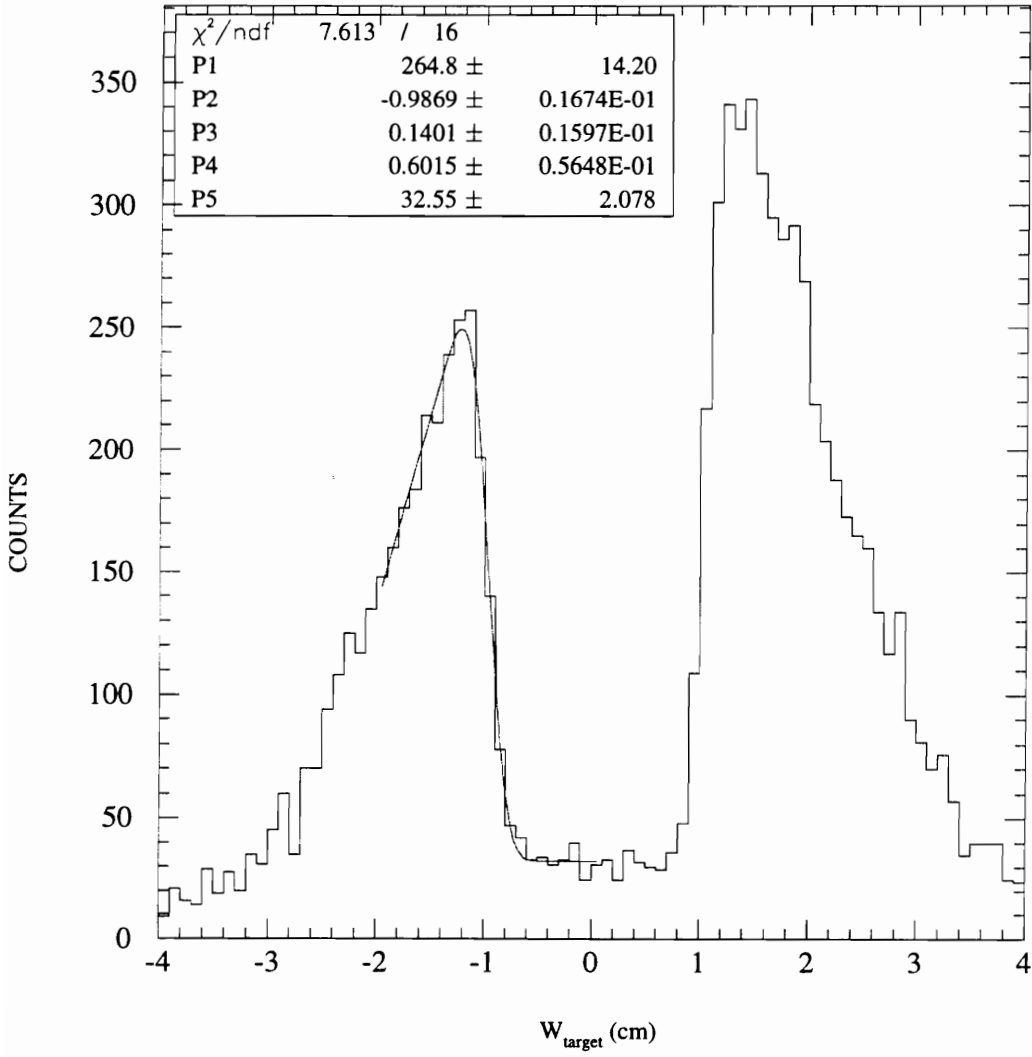


Figure 53: The w projected distribution for simulated events.

Comparing Monte Carlo simulation to the 1992 data, we find that 15% of the real events reconstruct into the target hole while less than 6% of the simulated events do so; and the position reconstruction at the hole edges are comparable. The events that reconstruct into the hole arise from misidentifying the decay point of the track due to inefficiencies of chamber wires or electronics noise.

The Monte Carlo used average, not wire-by-wire, efficiencies for the chambers, and did not incorporate chamber noise at all because of the lack of a reliable model for this noise.

It is apparent from comparing the profiles of Fig. 51 and Fig. 53 that the simulated muon beam's transverse profile was somewhat broader than data's and that the x and y centroids didn't match. These explain the difference in the fraction of decay points in the hole between simulated and real data.

4.4.2 Positron Initial Direction Resolution

A decay positron emitted from the μ decay vertex is subjected to multiple scattering and energy loss in the target, helium, and MWPCs before penetrating the scintillators into the lead annulus. The initial direction of the positron is determined by traceback of the reconstructed helix to the decay point on the target. Scattering, especially in the target and target bag, can lead to a difference between the true initial direction and the reconstructed direction. The purpose of this analysis is to estimate the distribution of these differences, since it directly affects the $e\gamma$ opening angle cut. The Monte Carlo simulation is employed in this analysis. The algorithm is as follows:

1. Generate a set of Monte Carlo Michel decay positron events tracked through the practical detector, incorporating the MWPC efficiencies, the dead and hot wire map etc, and all of the material in the apparatus.
2. Select a group of physical quantities that can be measured in the real data, and histogram these to compare the Monte Carlo simulation with the real data. If the results agree, then it gives us confidence that the Monte Carlo program can simulate the performance of the MEGA detector.

3. Generate a set of Monte Carlo mono-energetic positrons (52.8 MeV) with realistic detector performance inputs.
4. Histogram the difference of the positron's generated initial direction with the direction measured from the reconstructed helix, then fit this distribution to obtain the positron initial direction resolution.

The physical process simulated by Monte Carlo was the low rate Michel decay process in the standard MEGA target. The quantities histogrammed for comparing the real and simulated data fell into three classes: (1) the low-level detector performance (e.g., wire and scintillator hit frequencies) that were used to tune the detector efficiencies and dead and hot wire lists, (2) the reconstructed track parameters (e.g., number of loops between decay point and hit scintillator), and (3) physical quantities unique to polarized Michel decay (e.g., energy, positron initial direction). The MWPC anode/cathode hit frequencies and the dead wire map were checked by comparing the real and simulated data (see histograms in Fig. 55—56). From the general agreement between these histograms, we are confident that the Monte Carlo simulation gives a good description of the behavior of the MEGA detector. For the initial direction measurement, the opening angle η between the positron's initial direction and target normal vector is used both to compare the simulated and real data and also as a cut variable to improve the direction resolution. (Tracks that are nearly tangent to the target plane, i.e. with $|\eta| \simeq 90^\circ$, scatter much more since they pass through a lot of material before leaving the target and are very hard to extrapolate to the target—see the discussion on “skip” events below.) In terms of the reconstructed track parameters, the direction cosines of the positron's initial unit vector are:

$$n_x = \frac{y - y_c}{\sqrt{a^2 + R^2}} \quad (92)$$

$$n_y = -\frac{x - x_c}{\sqrt{a^2 + R^2}} \quad (93)$$

$$n_z = \frac{a}{\sqrt{a^2 + R^2}} \quad (94)$$

Table 27: η distribution

Location	Real Data	Monte Carlo Simulation
Front side	67%	70%
Back side	23%	25%
Skipping	10%	5%

The η distributions are shown in Fig. 54 for real and simulated data. By convention, the events in the range $0^\circ < \eta < 90^\circ$ have the track coming out from the front of the target, while events in the range $90^\circ < \eta < 180^\circ$ have the track going out from back of target. Events near $\eta = 90^\circ$ are apparently suppressed because the reconstructed tracks come near the target plane but fail to intersect. These so-called “skip” events are assigned a value of $\eta \equiv 90^\circ$, which accounts for the spikes in Fig. 54. The fraction of events in each range is summarized in Table 27.

The asymmetry of the distribution between the front and the back side is caused by the gross chamber inefficiencies in the 1992 run (dwarf 3 downstream cathodes, all of dwarf 7, and roughly half of dwarf 5 anodes off), coupled with the asymmetric polar angle distribution of the positrons from the decay of $\sim 100\%$ polarized muons.

Finally, 52.8 MeV mono-energetic positrons were simulated with the same detector configuration. The true initial unit vector of the positron track was obtained from the Monte Carlo event history and compared with the reconstructed unit vector. The histogram of the angle λ between these directions is shown in Fig. 57. The raw initial direction resolution of $1.56^\circ \pm 0.06^\circ$ (FWHM) can be derived by fitting this λ distribution.

A cut on the η distribution can be applied to improve the initial direction resolution, as is apparent from scatterplot of η vs λ shown in Fig. 58.

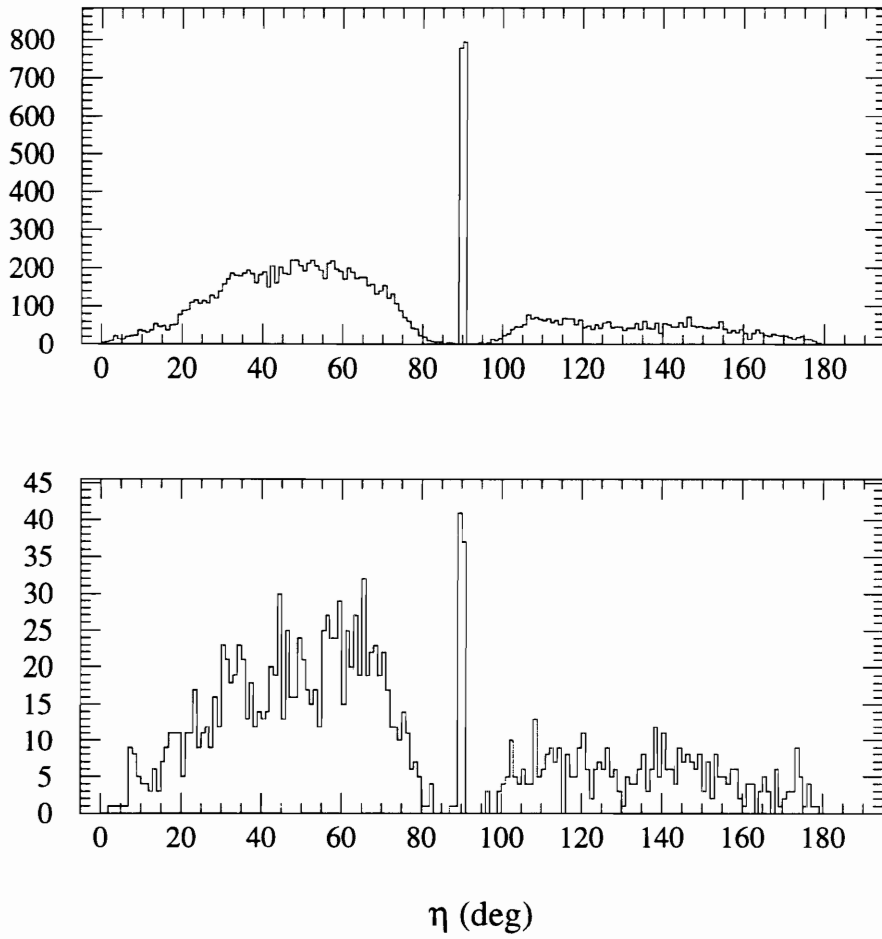


Figure 54: The η distribution for real data (top) and Monte Carlo simulation (bottom)

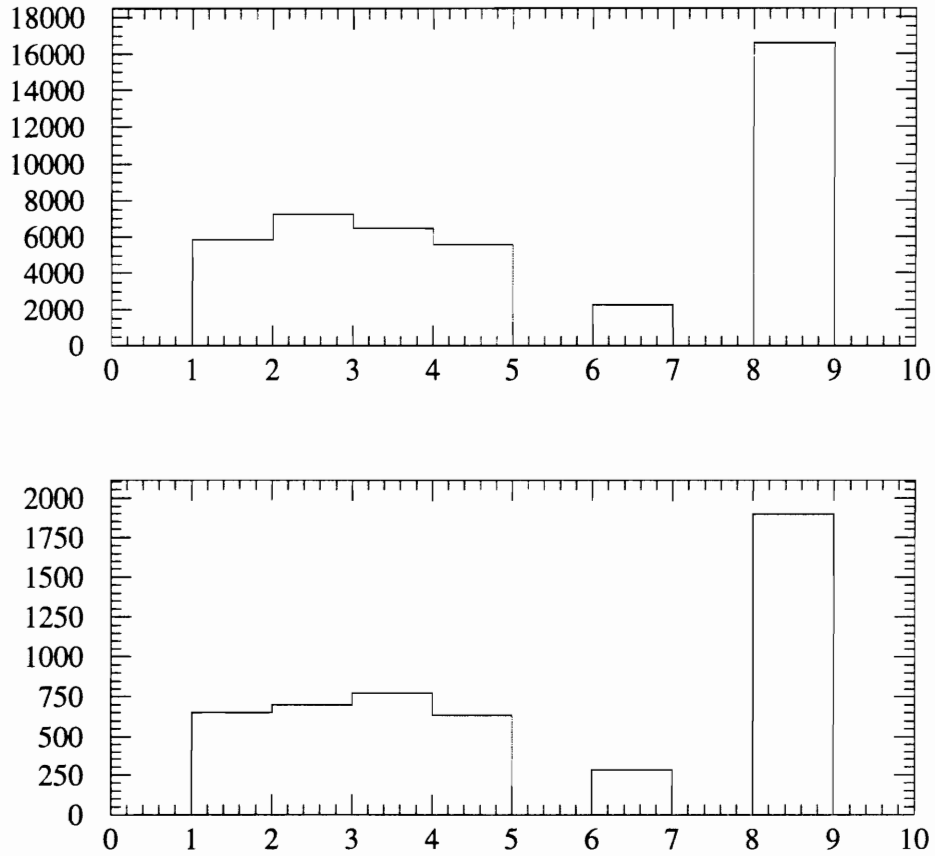


Figure 55: The positron MWPC usage frequency in the track reconstruction for the data (top) and simulation (bottom)

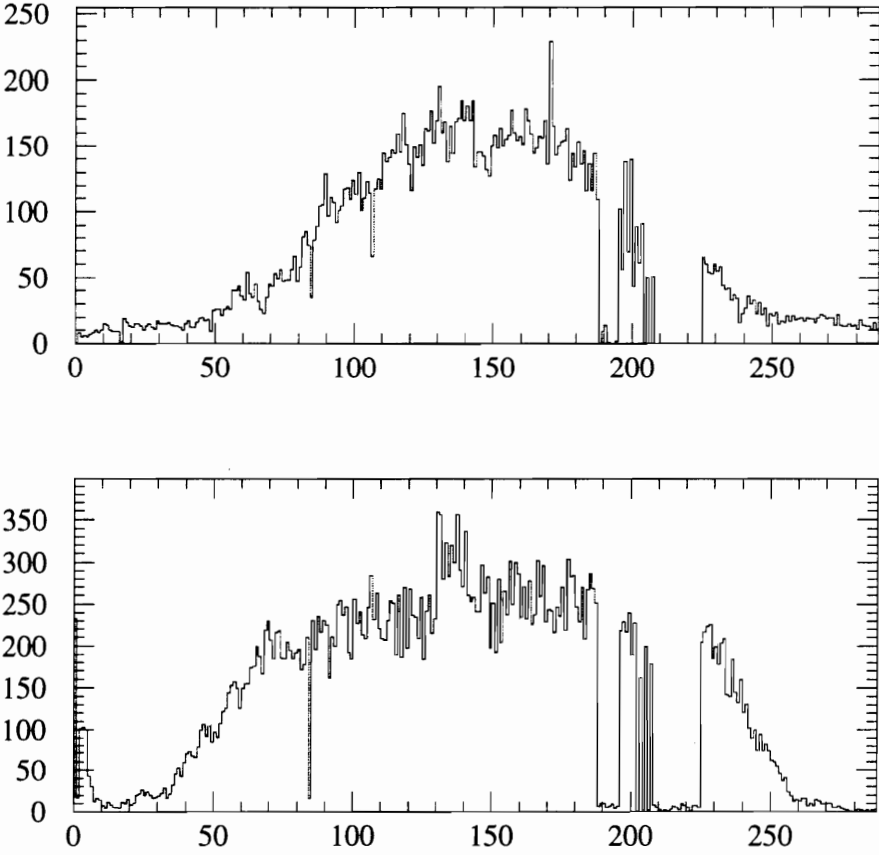


Figure 56: The Dwarf 1 anodes hit frequency for the data (top) and simulation (bottom)

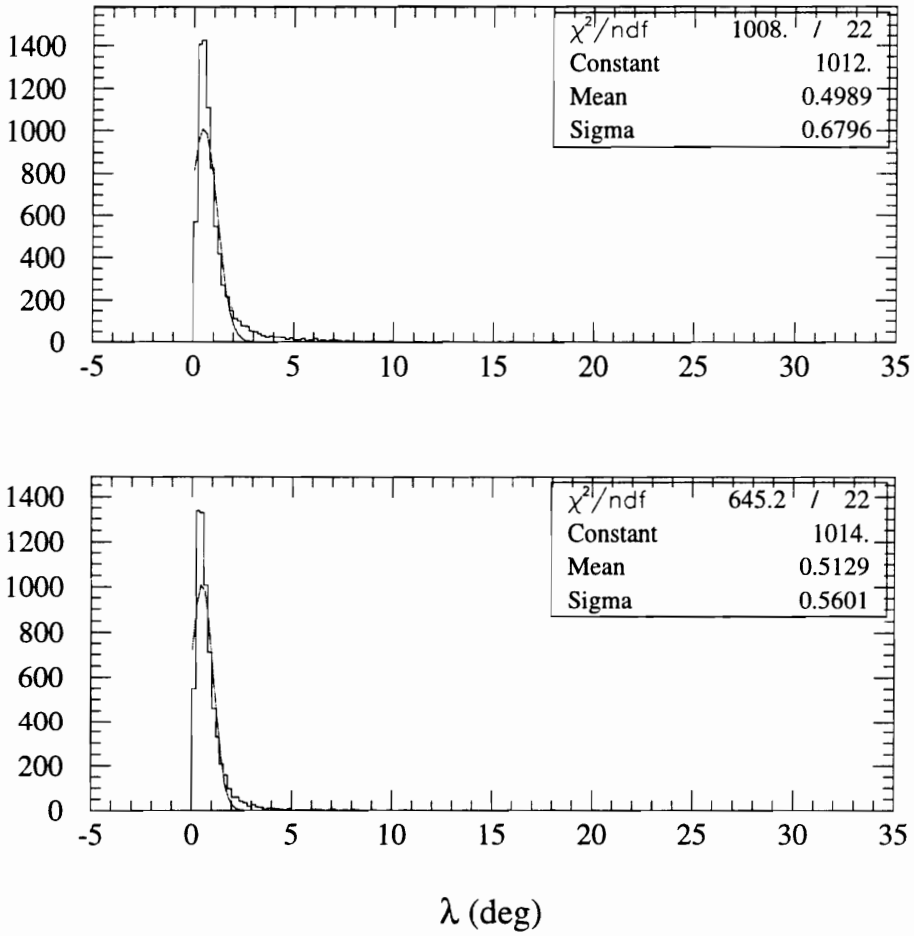


Figure 57: The λ distribution, before the cut on η (top) and after the cut (bottom).

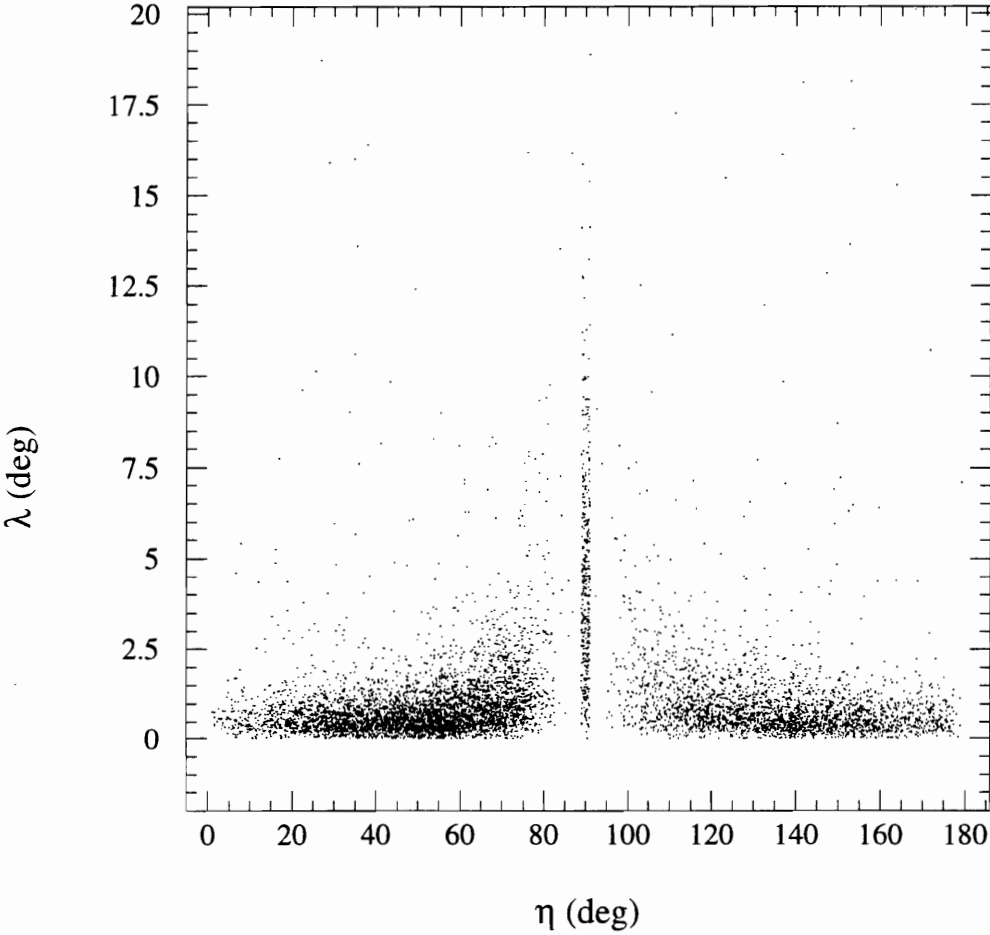


Figure 58: The η vs λ distribution

Keeping only those events with $\eta < 70^\circ$ or $\eta > 110^\circ$, the initial direction resolution is improved to $1.29^\circ \pm 0.04^\circ$. The λ distribution after the cut on η is shown in the bottom histogram of Fig. 57.

4.5 Timing

Fig. 59 shows the timing flow of a typical $\mu \rightarrow e\gamma$ event. By convention, the origin of time may be chosen to be the μ decay time; but in fact, we cannot measure directly this decay time nor any other time relative to this origin. All of our timing instruments—TDCs—measure only time intervals rather than absolute times.

The time intervals can be classified into either invariants or those that vary from event to event. In the latter category are the time from the μ decay to the earliest passage of the photon's e^+/e^- pair through the photon scintillator; the time from the μ decay to the positron's passage through the positron scintillator; and the propagation delay of light to the readout end of the positron scintillator. Among the invariants are the time delays in the phototubes, signal cables and readout electronics. By analyzing special timing data, we measured these “invariant intervals” for each scintillator channel and monitored their drifts with changes in the environment conditions such as ambient temperature and pressure.

The following section describes the timing calibration process.

4.5.1 Scintillator Timing Calibration

The scintillator timing constants were extracted from special runs taken using a pair of scintillator detectors called Ring Counters. These counters are located at the far ends of the upstream and downstream beam pipes and inside the positron scintillator barrels (see Fig. 60). Both upstream and downstream ring counters are instrumented to record the hit times at both ends of the ring (“high- ϕ ” and “low- ϕ ”). A small slot is cut through the lead beam pipes that allows some positrons emitted from μ decays on the vacuum window to hit the Ring Counter. Some of these positrons then radiate a photon. (The bremsstrahlung probability is enhanced by wrapping

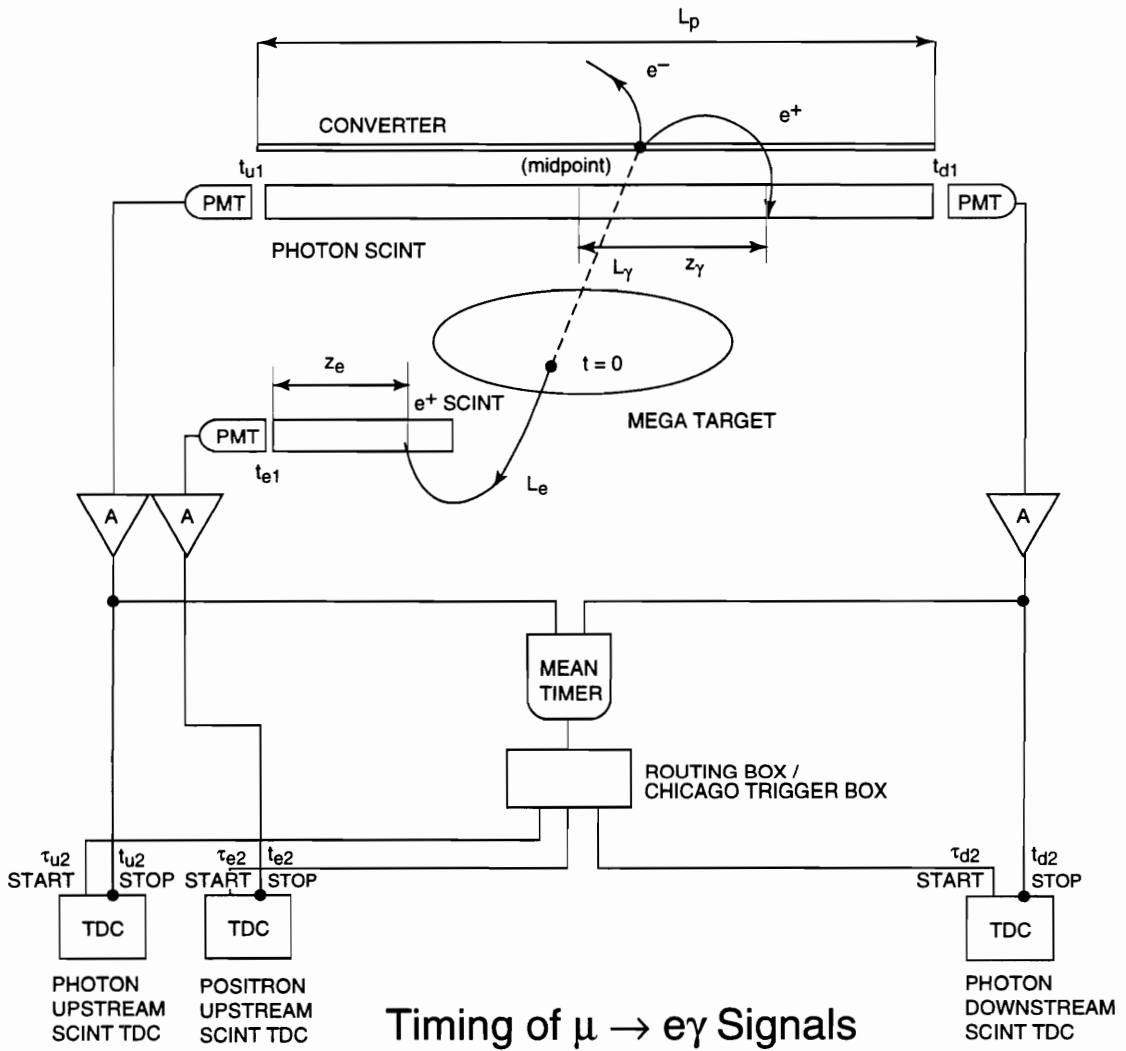


Figure 59: The timing flow chart of a typical $\mu \rightarrow e\gamma$ signal

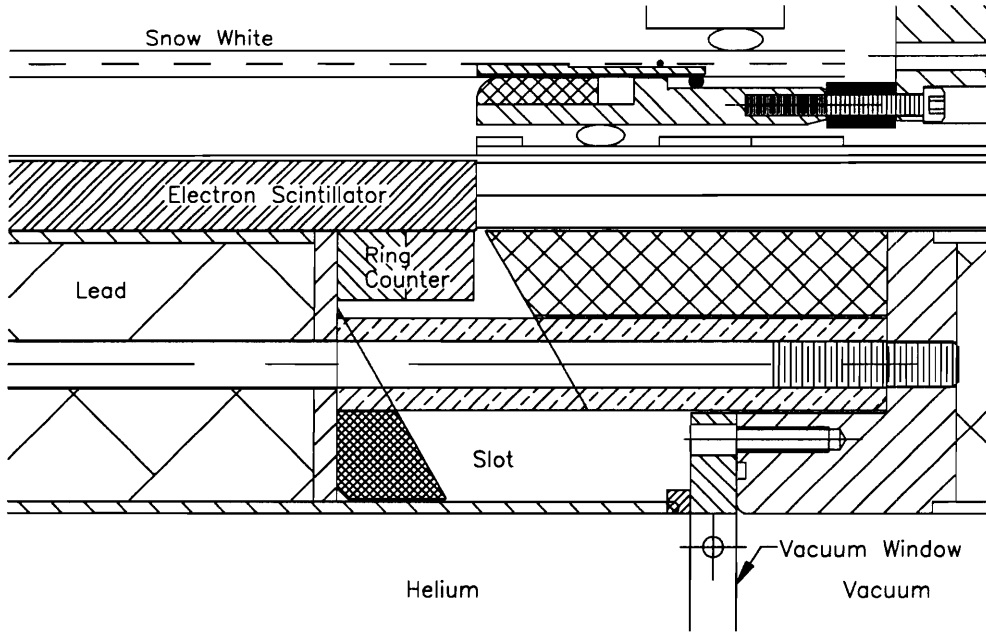


Figure 60: The location of the downstream Ring Counter.

the outside of each Ring Counter with lead tape.) The positron nearly always hits a positron scintillator. The radiated photon enters the MEGA detector roughly along the slot, hits the photon spectrometer, then converts into an e^+/e^- pair.

The scintillator timing calibration events are triggered by the coincidence of a Ring Counter and any photon scintillator. A large sample of such events allows us to measure the inter-channel variations of the timing invariants. Fig. 61 shows the timing flow of a typical timing calibration event. The times measured by the Ring Counter, photon scintillator, and positron scintillator TDCs, relative to the trigger time (which is determined by the Ring Counter, by design), are given by

$$t'_{RC} = \Delta T_{RC} - \Delta \tau_{RC} \quad (95)$$

$$t'_\gamma = \frac{1}{2} (t'_{\gamma u} + t'_{\gamma d}) = \left(\frac{L'_\gamma}{c} + \frac{L_p}{v_\gamma} \right) + \frac{1}{2} (\Delta T'_{\gamma u} + \Delta T'_{\gamma d}) - \frac{1}{2} (\Delta \tau'_{\gamma u} + \Delta \tau'_{\gamma d}) \quad (96)$$

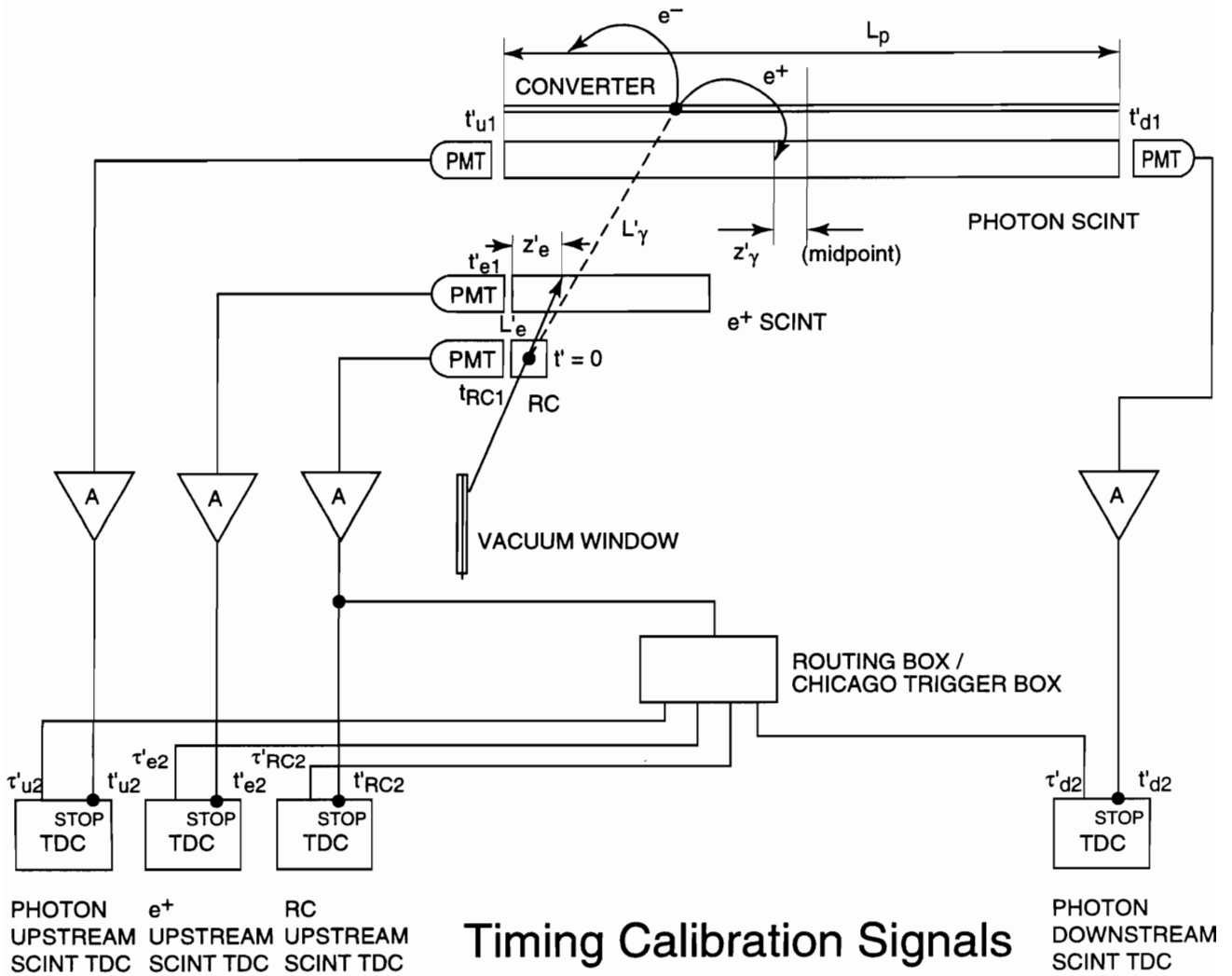


Figure 61: The timing flow chart of Ring Counter event. For simplicity, the photon scintillator meantimer input to Chicago trigger Box has been left out since it does not determine the trigger time.

$$t'_e = \left(\frac{L'_e}{c} + \frac{z'_e}{v_e} \right) + \Delta T_e \quad (97)$$

while the photon and positron times relative to the Ring Counter time are given by

$$t''_{\gamma} \equiv t'_{\gamma} - t'_{RC} = \left(\frac{L'_{\gamma}}{c} + \frac{L_p}{v_{\gamma}} \right) + \left[\frac{1}{2}(\Delta T'_{\gamma u} + \Delta T'_{\gamma d}) - \frac{1}{2}(\Delta \tau'_{\gamma u} + \Delta \tau'_{\gamma d}) - \Delta T'_{RC} + \Delta \tau'_{RC} \right] \quad (98)$$

$$t''_e \equiv t'_e - t_{RC} = \left(\frac{L'_e}{c} + \frac{z'_e}{v_e} \right) + [\Delta T'_e - \Delta \tau'_e - \Delta T'_{RC} + \Delta \tau'_{RC}] \quad (99)$$

Here, $v_{\gamma} = v_e = 0.5c$ is the average light propagation speed in the photon and positron scintillator bars; L_p , L'_{γ} and L'_e are shown in Fig. 61; and the invariant time intervals are defined in terms of the events times of Fig. 61 by

$$\Delta T'_{RC} = t'_{RC2} - t'_{RC} \quad (100)$$

$$\Delta \tau'_{RC} = \tau'_{RC2} - t'_{RC} \quad (101)$$

$$\Delta T'_{\gamma u} = t'_{u2} - t'_u \quad (102)$$

$$\Delta T'_{\gamma d} = t'_{d2} - t'_d \quad (103)$$

$$\Delta \tau'_{\gamma u} = \tau'_{u2} - t'_{RC} \quad (104)$$

$$\Delta \tau'_{\gamma d} = \tau'_{d2} - t'_{RC} \quad (105)$$

$$\Delta T'_e = t'_{e2} - t'_{e1} \quad (106)$$

$$\Delta \tau'_e = \tau'_{e2} - t'_{RC} \quad (107)$$

Note that the mean of the upstream-end and downstream-end TDC measurement has been used for the photon time, to avoid a dependence on z'_γ .

In this restricted geometry, the typical flight paths of the photon and positron, L'_γ and L'_e , are fixed on average, so that the centroids of the t''_γ and t''_e distributions (as well as the t'_γ and t'_e distributions) are constants for the struck scintillators. (The calculated values for L'_γ for layers 1, 2, and 3 were $c \cdot 0.9$ ns, $c \cdot 1.5$ ns, and $c \cdot 2.1$ ns, respectively.)

For convenience, we choose the reference point of the positron scintillator bar so that $z'_e \equiv 0$. Then, we eliminate the layer-by-layer dependence of the flight path L'_γ to the photon spectrometer and arrive at the following “equal-time-offsets” for each positron and photon scintillator:

$$t_e^\circ = t_e'' \quad (108)$$

$$t_\gamma^\circ = t_\gamma'' - \frac{L'_\gamma - L'_e}{c} \quad (109)$$

Note that separate constants must be stored for the even-event and odd-event readout TDCs on each positron scintillator. For 1992 data, the TDC readout of the high ϕ end of the upstream Ring Counter failed. For this data, the equal-time offsets were derived using t'_e and t'_γ instead of t''_e and t''_γ . These constants drift with changes in the environment; we account for these drifts by taking a set of calibration runs every 8 hours (once a shift) during the MEGA data taking stage.

Returning to the timing diagram for a typical $\mu \rightarrow e\gamma$ event (Fig. 59), the raw positron and photon times relative to the GHIGH trigger are:

$$t_e = \left(\frac{L_e}{c} + \frac{z_e}{v_e} + \Delta T_e \right) - \left[\frac{L_\gamma}{c} + \frac{L_p}{v_\gamma} + \Delta \tau_e \right] \quad (110)$$

$$t_\gamma = \left(\frac{L_\gamma}{c} + \frac{L_p}{v_\gamma} + \Delta T_\gamma \right) - \left[\frac{L_\gamma}{c} + \frac{L_p}{v_\gamma} + \Delta \tau_\gamma \right] \quad (111)$$

where the TDC start times in the second square brackets of both equations depend explicitly on when the photon generated the GHIGH trigger.

As for the timing calibration, the invariant time intervals in the above equations can be expressed in term of the times shown in Fig. 59 by:

$$\Delta T_\gamma = \frac{1}{2}(\Delta T_{\gamma u} + \Delta T_{\gamma d}) = \frac{1}{2}[(t_{u2} - t_{u1}) + (t_{d2} - t_{d1})] \quad (112)$$

$$\Delta \tau_\gamma = \frac{1}{2}(\Delta \tau_{\gamma u} + \Delta \tau_{\gamma d}) = \frac{1}{2}[(\tau_{u2} - t_{u1}) + (\tau_{d2} - t_{d1})] \quad (113)$$

$$\Delta T_e = t_{e2} - t_{e1} \quad (114)$$

$$\Delta \tau_e = \tau_{e2} - \frac{1}{2}(t_{u1} + t_{d1}) \quad (115)$$

If the raw times t_e and t_γ are corrected by the equal-time offsets t_e° and t_γ° and the event-specific propagation delays, the difference of these corrected times gives us the $e - \gamma$ relative time at the μ decay point:

$$\Delta t_{e\gamma} = \left[t_e - t_e^\circ - \left(\frac{L_e}{c} + \frac{z_e}{v_e} \right) \right] - \left[t_\gamma - t_\gamma^\circ - \frac{L_\gamma}{c} \right] \quad (116)$$

$$= (\Delta T_e - \Delta T'_e) - (\Delta T_\gamma - \Delta T'_\gamma) - (\Delta \tau_e - \Delta \tau'_e) + (\Delta \tau_\gamma - \Delta \tau'_\gamma) \quad (117)$$

Comparing the timing diagrams of Fig. 59 and Fig. 61, it is clear that the signal paths are common in both events, so that $\Delta T_e = \Delta T'_e$ and $\Delta T_\gamma = \Delta T'_\gamma$. (Actually, a systematic difference in pulse heights between calibration and physics data leads to a sub-ns difference between $\Delta T'_\gamma$ and ΔT_γ due to leading edge walk.) Although the trigger paths (and delays) are different, it should be apparent that these differences are common for both positron and photon TDC start signals, i.e., $\Delta \tau_e - \Delta \tau'_e = \Delta \tau_\gamma - \Delta \tau'_\gamma$. Therefore, for a true $\mu \rightarrow e\gamma$ coincidence, the time difference vanishes:

$$\Delta t_{e\gamma} = 0 \quad (118)$$

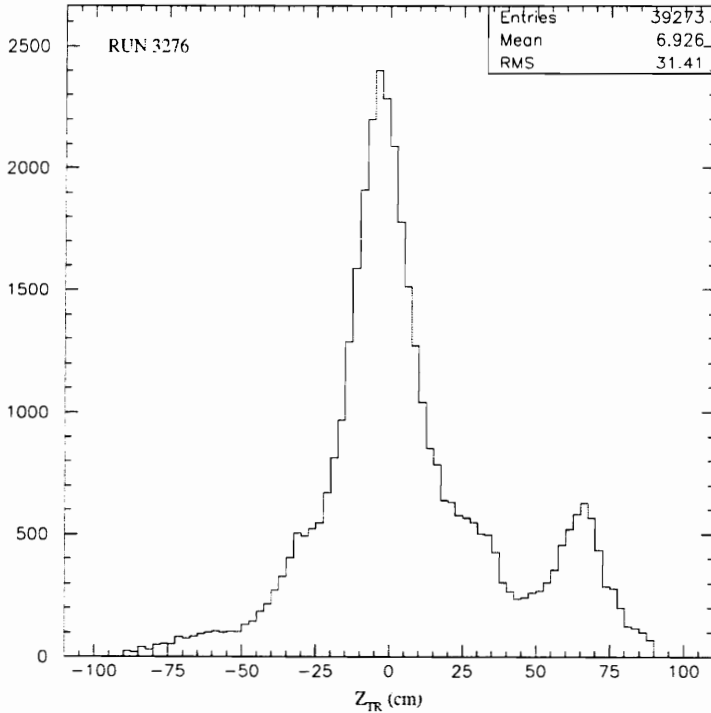


Figure 62: Photon traceback to the z -axis for a typical MEGA run.

4.5.2 Ring Counter Events in the MEGA data

The fidelity of the timing constants can be tested by seeking physical processes that have a positron-photon timing coincidence. For example, some Ring Counter events will appear in the MEGA production data on the rare occasion when the bremsstrahlung photon is energetic enough to fire the “GHIGH” trigger.

Fig. 62 shows the distribution of the z component of the photon when projected back to the z axis in a typical MEGA run. A peak is clearly visible centered on the downstream Ring Counter, resulting from the large fraction of muons passing through the target hole to the downstream vacuum window. We use these events to check the scintillator equal-time offsets.

Candidate Ring Counter events must have a reconstructed photon, one or two hits on the downstream Ring Counter, and at least one struck positron scintillator at the downstream end. Then we demand that the positron scintillator and Ring Counter

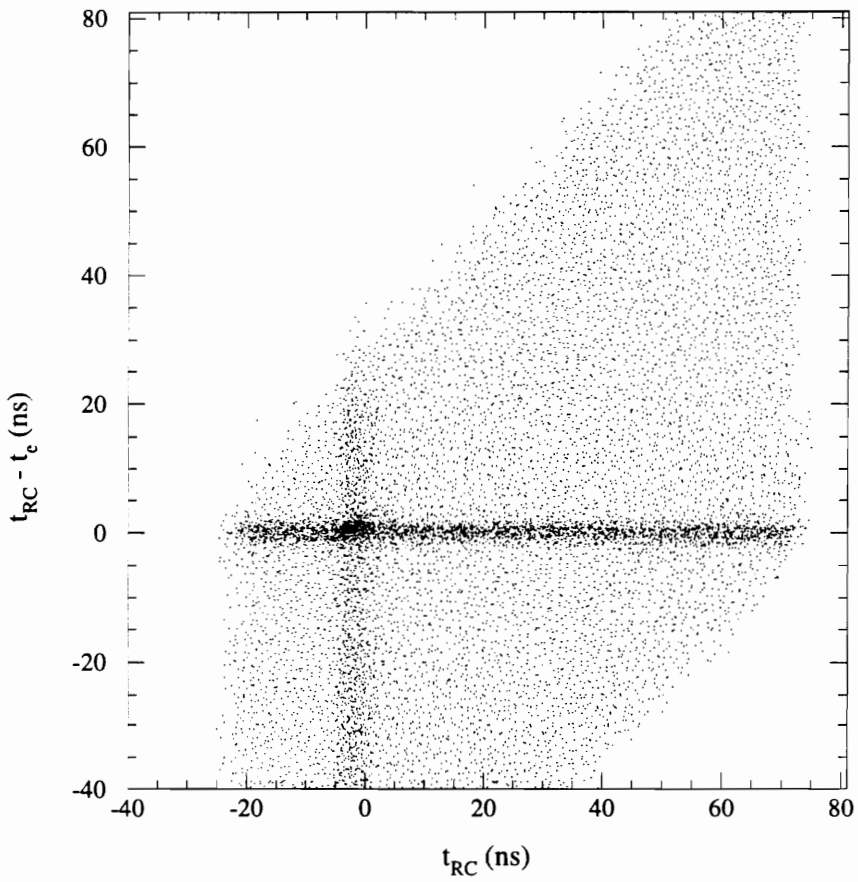


Figure 63: Difference of Ring Counter time with scintillator times vs Ring Counter time

hits be correlated in time. (Since the Ring Counter and positron scintillator are so near each other, we expect a very narrow width in the relative time distribution.) Fig. 63 is a scatterplot of the Ring Counter-positron scintillator time difference versus the Ring Counter time. The true coincidences are located at the overlap of the horizontal and vertical bands. The top histogram of Fig. 64 is the projection of the horizontal band onto the t_{RC} axis. (The location of the peak at $t_{RC} = -2$ ns is a reflection of the difference in the times of the GHIGH and RC-PSC trigger.) The bottom histogram of Fig. 64 shows the z distribution of the photons projected back to the z axis after requiring that $|t_{RC} - t_e| < 3.16$ ns and -3.76 ns $< t_{RC} < 0$ ns. An enhancement of the Ring Counter-photon coincidence signal is apparent.

The final cut to enhance to Ring Counter-photon coincidence requires that the photon project back to a location on the z axis that is within ± 8 cm of the downstream struck Ring Counter.

With coincident photon and positron scintillator in hand after applying the cuts, we evaluate the positron-photon relative time:

$$\Delta t_{e\gamma} = \left[t_e - t_e^\circ - \left(\frac{L_e}{c} + \frac{z_e}{v_e} \right) \right] - \left[t_\gamma - t_\gamma^\circ - \frac{L_\gamma}{c} \right] \quad (119)$$

where $t_e - t_e^\circ$ is the positron's measured time corrected by the equal-time offset, L_e/c is flight delay of the positron, $z'_e/v_e \equiv 0$ is the light propagation delay in the positron scintillator, $t_\gamma - t_\gamma^\circ$ is the photon's measured meantime corrected by the equal-time offset, and L_γ/c is the flight time of the photon. The net flight distance $L_\gamma - L_e$ is calculated as the distance from the time-coincident positron scintillator (with the hit at $z = z_{RC}$) to the reconstructed photon conversion point.

The time difference $\Delta t_{e\gamma}$ is histogrammed for the two photon layers and the even or odd scintillator TDCs. The timing coincidence spectra are shown in Fig. 66 and their sums are shown in Fig. 67. We observe that all of the peaks are shifted by a few hundred picoseconds from $\Delta t_{e\gamma} = 0$. This is most likely due to a systematic difference in the leading edge walk between the soft photon in the timing calibration runs and the hard triggering photons in the physics runs. No leading edge walk corrections were applied to the 1992 data.

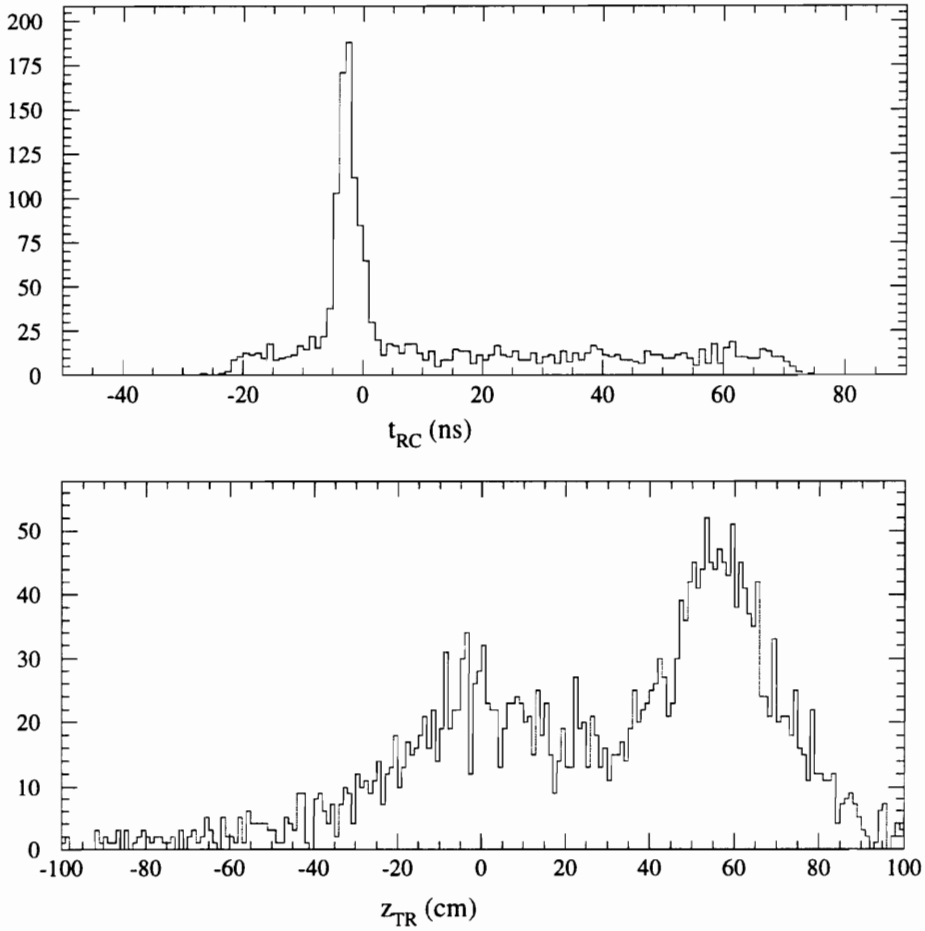


Figure 64: The Ring Counter time distribution for the horizontal band of Fig. 63 (top) and the photon traceback distribution after requiring Ring Counter-positron scintillator time coincidence (bottom).

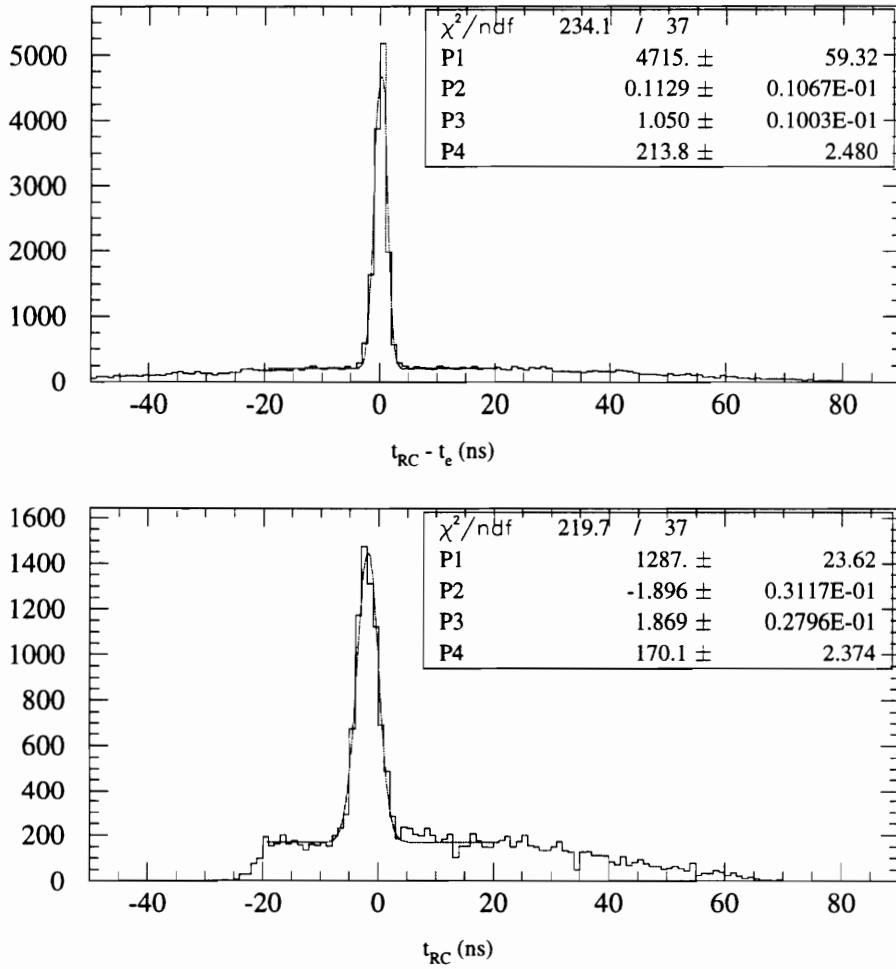


Figure 65: The projections of the horizontal band of Fig. 63 onto the horizontal axis (top), and of the vertical band onto the vertical axis (bottom). We apply cuts of $\pm 3\sigma$ about the peak centroid of the top graph, and $\pm 1\sigma$ about the peak centroid of the bottom graph.

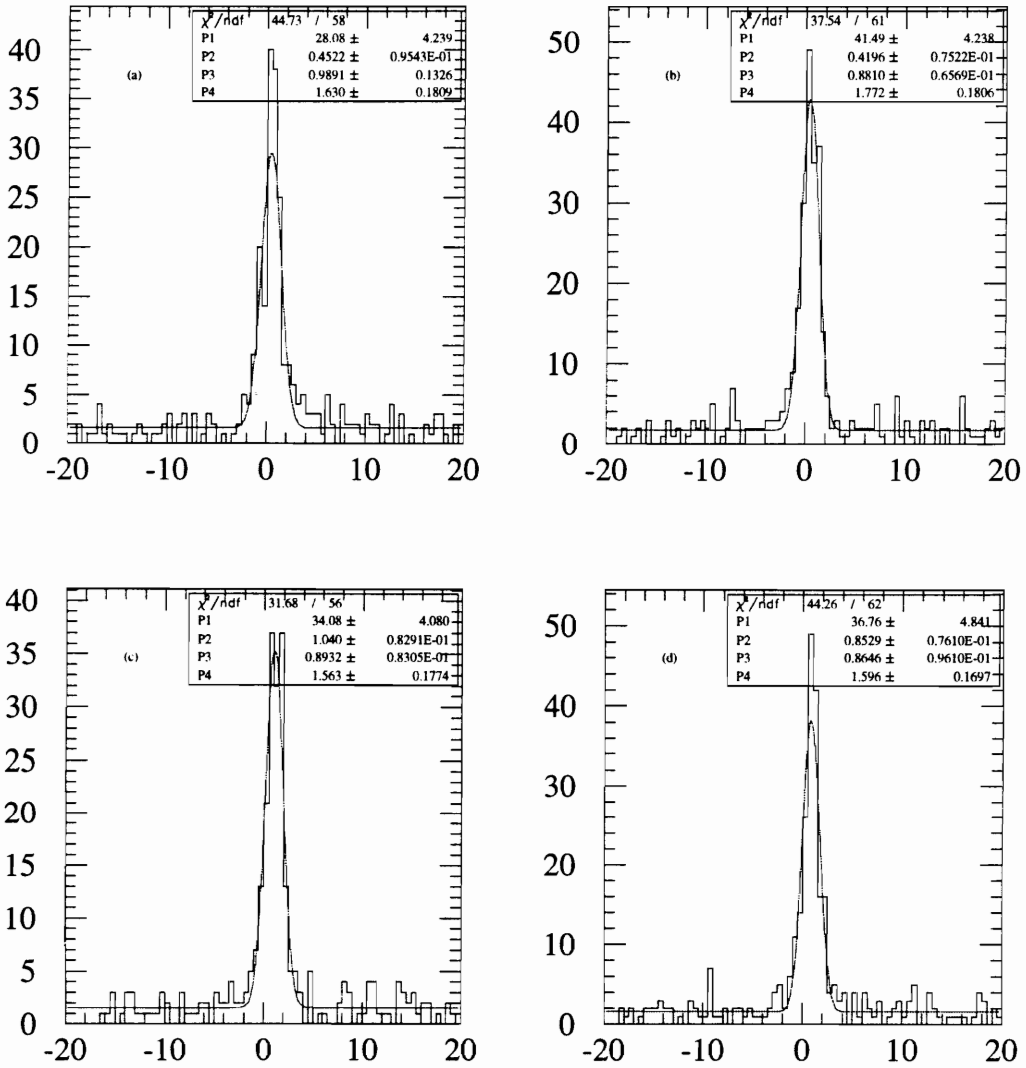


Figure 66: $\Delta t_{e\gamma}$ distribution of Ring Counters for (a) layer 1 photon and even-TDC positron, (b) layer 1 and odd-TDC, (c) layer 2 and even-TDC and (d) layer 2 and odd-TDC.

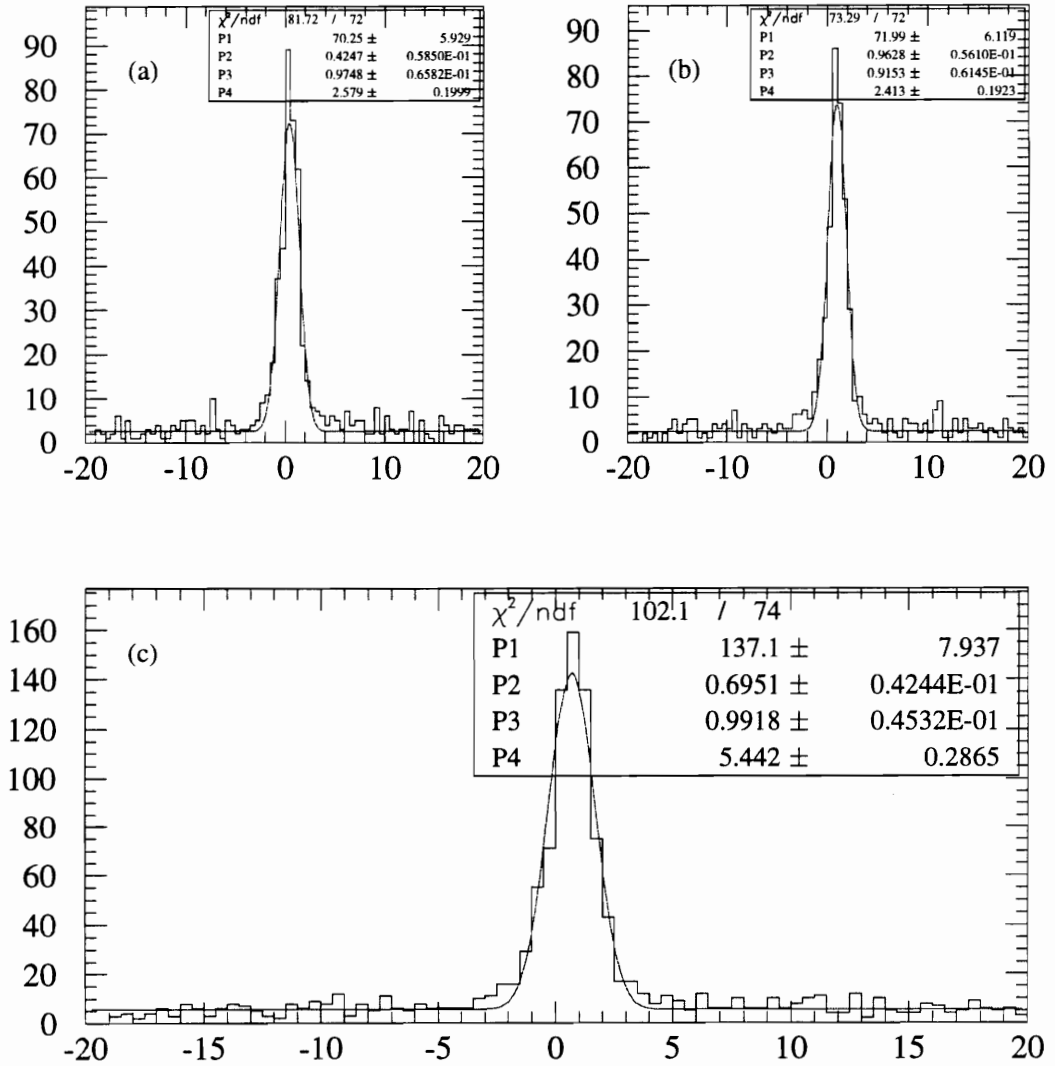


Figure 67: The sums of time spectra of Fig. 66. (a) Layer 1 photon with Even- and Odd-TDC positron; (b) layer 2 photon with Even- and Odd-TDC positron; (c) all events.

4.6 Muon Inner Bremsstrahlung

4.6.1 Inner Bremsstrahlung Data Analysis

For photon energies greater than 51.2 MeV, muon inner bremsstrahlung $\mu \rightarrow e\gamma\nu\bar{\nu}$ is of great concern and interest to us. It is one of the main sources of prompt background of the MEGA experiment. (It is also a source of energetic photons that appear in random coincidence with uncorrelated energetic positrons.) Inner Bremsstrahlung provides another set of data in which the photon and the positron have a true timing coincidence. Finally, this process lets us check the overall detector setup.

The Inner Bremsstrahlung data were taken using the GHIGH trigger as for the MEGA production data, but at a very low μ beam rate (typical one muon decay per trigger) to discriminate against random coincidences. The low rate also enhanced the ERC positron reconstruction efficiency.

In 1993 and beyond, the GHIGH trigger's energy threshold was effectively reduced to 32 MeV by lowering the magnetic field to 75% of its normal value. This also reduced the positron energy threshold to about 30 MeV. These lower thresholds increased the acceptance for $\mu \rightarrow e\gamma\nu\bar{\nu}$ by a factor of 550. Unfortunately, this enrichment mechanism was not exploited in 1992.

Photons were reconstructed by the PAIRS package and positrons by the ERC package, both within the framework of the REPLAY program. The reconstructed photon's origin was estimated by projecting it back to z axis; this projected origin had to be within the range of the μ stopping target ($|z| \leq 25$ cm). The reconstructed positron's helix was followed back to its intersections with the stopping target, and the μ decay point(s) was(were) selected from among these crossing points. In order to avoid ambiguity, we kept only those events whose positron track had a uniquely determined decay point. Also, we demanded that z components of this μ decay point and the traceback of the photon be within ± 8 cm of each other. (This window was determined by the photon traceback resolution.)

For the events that satisfied the above requirements, we examined the times of both particles. The photon meantime, $t_\gamma - t_\gamma^o$, was the average of the meantimes

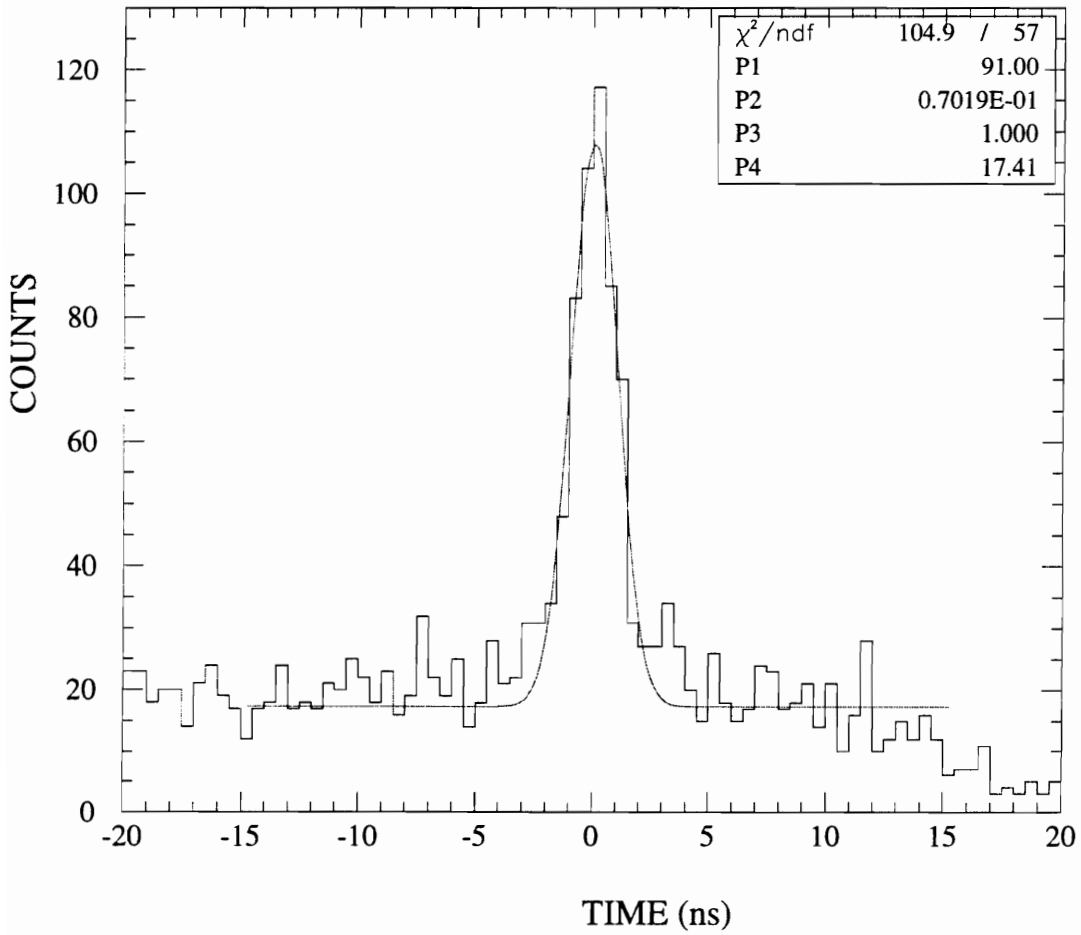


Figure 68: The positron-photon relative time distribution for muon Inner Bremsstrahlung ($\mu \rightarrow e\nu\bar{\nu}\gamma$) events in 1994.

(corrected by their equal-time offsets) of the two scintillators at the low- ϕ and high- ϕ edges of the photon's e^+e^- pair. The positron time, $t_e - t_e^\circ$ was also an average of the equal-time-offset corrected times for all struck scintillators in a 5 scintillator wide window around the intersection point of the positron track with the scintillator barrel (as long as the times of these scintillators were reasonably coincident.) The photon flight time, L_γ/c , was directly computed by the straight-line distance from the μ decay point to photon conversion point. (The flight time of the first half loop of the e^+e^- pair was properly accounted for by PAIRS in the quantity $t_\gamma - t_\gamma^\circ$.) The flight time of the positron, L_e/c , was calculated from the reconstructed helix. The light propagation delay in the positron scintillator was calculated from the distance separating the helix-scintillator intersection and the axial reference point at the Ring Counter location.

The positron-photon time difference was given by

$$\Delta t_{e\gamma} = (t_e - t_e^\circ - \frac{L_e}{c} - \frac{z_e}{v_e}) - (t_\gamma - t_\gamma^\circ - \frac{L_\gamma}{c}) \quad (120)$$

With good equal-time offsets, the inner bremsstrahlung events should have given a peak centered at $\Delta t_{e\gamma} = 0$.

As mentioned above, we ran at the full 15 kG magnetic field in the 1992 run instead of at the IB-enrichment field of 11.25kG, and recorded 400K events in the special low-rate IB runs. Only a few events were reconstructed, not enough to form a significant timing spectrum. Having learned the lessons from the 1992 data run, the MEGA collaboration ran at lower field in the following years, and succeeded in finding the Inner Bremsstrahlung signal. For example, Fig. 68 shows the Inner Bremsstrahlung $e\gamma$ timing spectrum from 1994.

4.6.2 Inner Bremsstrahlung signal in the MEGA data

Another method for finding Inner Bremsstrahlung events in 1992 was available—by looking in the $\mu \rightarrow e\gamma$ production data. Although the raw data were dominated by random coincidences, a straightforward calculation indicated that a sizeable IB signal should have been observable if the proper kinematic cuts were made (looser than for

Table 28: Summary of estimation of IB signal and background in MEGA data

Symbols	Factors	Values
N_μ	Average stopped muon per run	7.1×10^9
x_e	Low limit of positron energy	$0.75 \cdot m_\mu/2$
x_γ	Low limit of photon energy	$0.67 \cdot m_\mu/2$
$M(x_e, x_\gamma)$	Integrated probability of IB with x_e and x_γ	9.9×10^{-7}
ϵ_s	Scintillator efficiency	97.8%
f_s	Fraction of e^+ hit scint	48.2%
f_{ip}	Fraction of photon interact photon arm	24.9%
f_{stage1}	Fraction of photon pass first stage trigger	20.0%
f_{stage2}	Fraction of photon pass second stage trigger	77.3%
ϵ_γ	γ Recon efficiency	45.9%
ϵ_e	e^+ Recon efficiency	51.4%
ϵ_{ib}	Fraction of events passing IB cuts	37.4%
IB signal events /run		11.3/run
Total IB signal events		2949
Total Background events		1.305×10^5

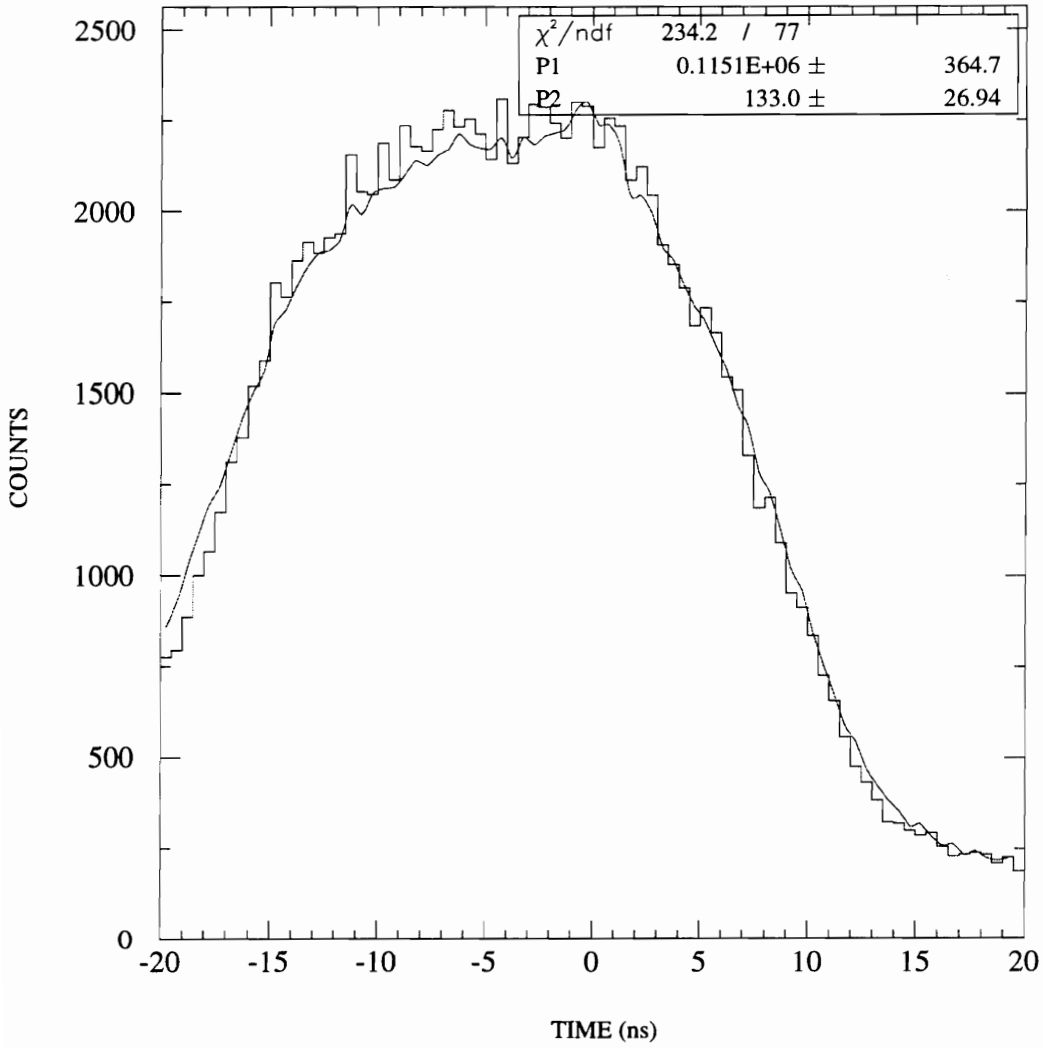


Figure 69: The $e - \gamma$ time spectrum from 1992 MEGA data with loose energy and opening angle cuts. The curve is sum of the the random background and the (small) prompt IB signal.

$\mu \rightarrow e\gamma$, of course.) These IB events could be used to check the scintillator timing calculations, and, importantly, to verify the overall performance of the detector for a prompt signal very much like $\mu \rightarrow e\gamma$.

A total of 261 runs were processed with the IB analysis code described in the previous section. In Fig. 69, a small prompt signal peak, containing 133 ± 27 events, was found by fitting the data to the best combination of the random distribution and a gaussian near $\Delta t_{e\gamma} = 0$. (The shape of the random timing distribution was obtained from the uncut data; this shape was invariant beyond $|\Delta t_{e\gamma}| > 5\text{ns}$ as successive cuts were applied.)

How did this compare with our IB signal expectation? The Monte Carlo simulation was used to generate IB events (with a 36 ns gate width on the MWPC latches) while the random background level was estimated from the 1992 data itself. Table 28 summarizes both the IB signal and random background estimates. The 97.8% positron scintillator efficiency came from the scintillator efficiency analysis performed on the 1992 RHO experiment data. In the 261 MEGA runs, we expected to see a total of 2949 IB signal events. *This number was about 22 times higher than observed.*

We now believe that this loss in sensitivity in the 1992 data came from using an overly short gate width on the FASTBUS latches that recorded the anode and cathode hits in the positron spectrometer MWPCs, and in mislocating this gate slightly relative to the “good” positron signals.

Fig. 70 shows results of a Monte Carlo study of the ERC reconstruction rate versus the chamber gate offset for two different gate widths: 34ns and 14ns. In 1992, the gate offset was set near the left edge of a corresponding experimentally measured efficiency curve (see Fig. 29). Later, the gate was narrowed from 34ns to 14ns without changing the gate offset. This oversight was not discovered until well after the end of the 1992 run. It made the positron spectrometer only 5% efficient for positrons that were truly coincident with the triggering photon. This is an efficiency that must be folded into the calculation if the $\mu \rightarrow e\gamma$ branching ratio sensitivity in the next and final chapter.

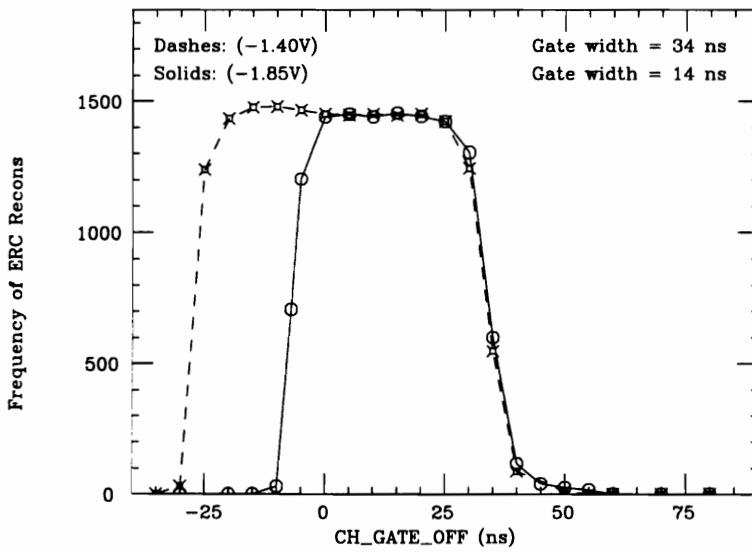


Figure 70: The ERC reconstruction rate vs chamber gate offset for simulated events.

Chapter 5

The $\mu \rightarrow e\gamma$ Search

5.1 Overview of Production Data Analysis

Recall that for the 1992 MEGA data taking stage from September 30 to October 11, the detector system consisted of two layers of photon pair spectrometers and the complete set of positron MWPCs and scintillators. Also, about 20% of the photon z readout delay lines were not instrumented due to a shortage of preamplifiers, and parts of the positron spectrometer MWPCs were not read out because of excess noise, preamplifiers oscillation or, in the case of dwarf 7, a broken anode wire. Only the first stage hardware trigger was available; the second stage trigger was simulated in the online workstation farm by the photon on-line software filter. Only four of the eight DECstations were installed in the workstation farm in 1992.

Due to unscheduled accelerator downtime, beam was available for MEGA about 200 hours in this period (see Table 29). The LAMPF accelerator operated with a proton current of between $100\mu\text{A}$ and $270\mu\text{A}$, with a duty factor of between 5.4% and 6.8% and a repetition rate of ~ 80 Hz.

Data taking was interrupted around run 3250 to diagnose and replace a bad TDC module in the photon spectrometer readout.

A total of 165.5M GHIGH-trigger events were taken in the 1992 run. Of these, 10.5M triggers were lost because two data tapes (runs 3188-3207) were found to be unreadable during the offline analysis. 0.9M triggers were taken with no online filter

Table 29: 1992 MEGA production Run

Run(s)	Dates (mm/dd)	Comments
2839-2839	09/29-09/29	MEGA test run
2840-2860	09/29-09/30	calibration
2861-2980	09/30-10/02	MEGA run
2981-3024	10/02-10/04	cosmic rays
3025-3049	10/04-10/04	MEGA run
3051-3098	10/04-10/05	cosmic rays
3099-3155	10/05-10/07	MEGA run
3156-3173	10/07-10/07	cosmic rays
3174-3207	10/07-10/08	MEGA run
3208-3326	10/08-10/11	MEGA run
2861-3326	09/29-10/11	

while optimizing the beam flux for the 1992 running conditions. The data acquisition system limited us to a muon stopping rate of 135MHz (instantaneous). 31M triggers were recorded with only the online photon filter imposed. Finally, 132M triggers were taken both with photon and positron filters imposed. In the last case, we wrote one unfiltered event to tape for every 200 filtered events in order to monitor the performance of the online filters.

The on line filters were described in detail in Chapter 3. In 1992, the photon z reconstruction was disabled, and only the first two cuts of the positron filter were enabled. By the action of these filters, about 1 in 10 triggers were stored on tape in 1992.

The offline data analysis proceeded in two stages named “Filter 1” and “Filter 3.” In Filter 1, each event had to have a crudely reconstructed photon (using the online PAIRS filter with tighter cuts) and a reconstructible positron (i.e., a set of positron chamber hits that satisfy the online ARC filter with the first 14 cuts applied; refer to Table 15 of Chapter 3). 87.4% of the taped events passed the Filter 1 photon filter; the failed events typically had no reconstructed vertex. The additional ARC cuts in Filter 1 reduced the data sample to 91.2K events (0.66% of the events that passed the PAIRS reconstruction). Most of the events from the runs before 3208 (when the ARC filter was first imposed in online filter) failed the first two ARC cuts now applied in the offline Filter 1. The remaining twelve ARC cuts of Filter 1 were responsible for removing the balance of the rejected events.

Filter 3 analyzed the 91.2K events that passed Filter 1. This analysis code use the offline-PAIRS package for photon reconstruction and the ERC package for positron reconstruction. Offline-PAIRS used a non-linear fitting program for the e^+e^- pair from the converted photon. (This procedure was described in more detail in Chapter 3.) The online-ARC information for each candidate positron from Filter 1 was regenerated again in Filter 3, then reformatted by a special interface code for ERC analysis. The interface code selected all anode hits in the ARC wire window predicted for a 52.8 MeV positron reasonably back-to-back with the reconstructed photon, then compiled a list of all of the struck cathodes that crossed these anodes. This restricted set of anodes and cathodes was used by ERC to reconstruct positron tracks. This

Table 30: The 1992 filter efficiencies

Filter stage	% Fraction of events passed
On-line filter	10.2
Filter 1 photon	87.4
Filter 1 positron	0.66
Filter 3 photon	82.4
Filter 3 positron	41.3
All	0.02

reduction in the numbers of anodes and cathodes seen by ERC reconstruction code made the combinational problem more manageable, but also resulted in the occasional reconstruction of a ghost track out of this partial hit list. These ghost helices were reduced from 20% to 5% by imposing quality cuts on the goodness of fit (χ^2 of the end and side view fits) of each track. Filter 3 reduced the sample from 91.2K to 31K. The reconstructed information for each track—but no longer the raw hit information—was stored in an “Ntuple” file for final processing by CERN’s Physics Analysis Workstation (PAW)[52]. The fraction of events passing each stage of the 1992 filter are summarized in Table 30.

Fig. 71 shows the performance of the offline-PAIRS and ERC package in Filter 3 for all of the 1992 MEGA data with four contiguous run numbers combined into one histogram bin. The holes in both histograms correspond to periods of scintillator timing calibration or unavailability of beam. (Diagnostic or cosmic ray runs were taken during the beam-off intervals.) The variations in the number of events per run reconstructed by PAIRS in Filter 3 reflects the changing number of triggers recorded per run (300K initially, 600K during the middle runs, and 1M during the later runs).

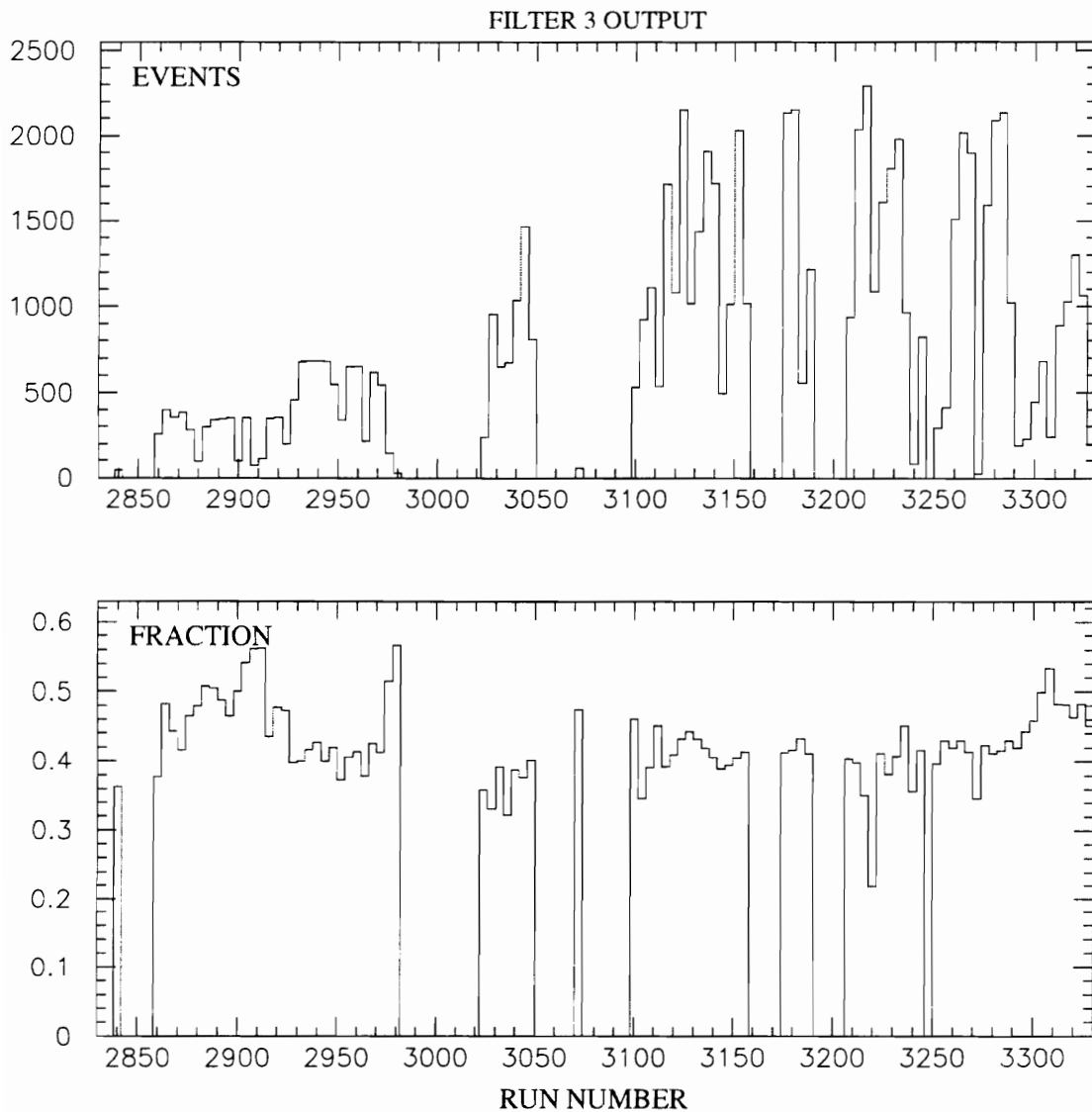


Figure 71: Number of events reconstructed by the photon arm section of Filter 3 photon analysis (top), and the fraction of events reconstructed by the electron arm analysis (bottom) as a function of run number.

The roughly constant 41% average yield of the ERC reconstruction shown in the bottom histogram of Fig. 71 demonstrates its insensitivity to the larger variations in the instantaneous muon stopping rate when reconstructing tracks from the restricted list of anode and cathode hits that lay within the ARC windows calculated for a 52.8 MeV positron.

5.2 Cut Analysis and $\mu \rightarrow e\gamma$ Search

The 31 K events from Filter 3 were processed by PAW to search for the $\mu \rightarrow e\gamma$ signal in the 1992 MEGA data. The Ntuple for each candidate event contained the analyzed information for exactly one photon and between one and three positron tracks. In selecting the final sample of candidate $\mu \rightarrow e\gamma$ events with PAW, we applied cuts on the following kinematic quantities:

1. positron energy
2. photon energy
3. positron-photon opening angle cut
4. Relative $e\gamma$ timing cut

Fig. 72 shows the distributions of these quantities for the 1992 data sample examined in PAW. Note in particular that the $\Delta t_{e\gamma}$ distribution is not flat because of a mistiming of the gates to the positron chamber anode and cathode latches. This flaw and its consequence for the $\mu \rightarrow e\gamma$ search is discussed in more detail at the conclusion of this chapter.

In the following sections, we describe how the cuts on these quantities were selected and evaluate the fraction of $\mu \rightarrow e\gamma$ events that would have passed these cuts. The final $\mu \rightarrow e\gamma$ signal search is given in the last section of this chapter.

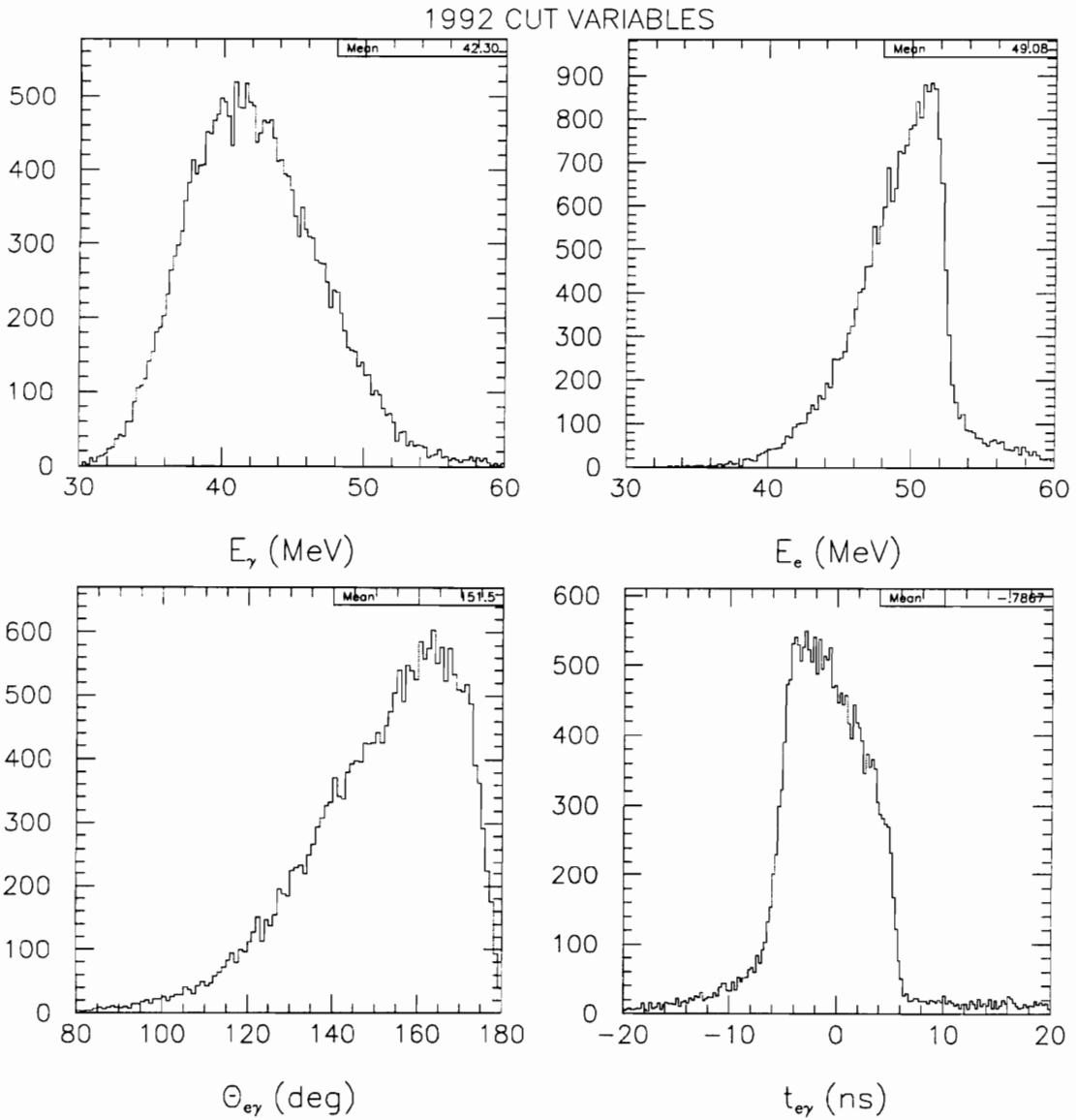


Figure 72: The photon and positron energy spectra, the $e\gamma$ opening angle spectrum, and the relative timing spectrum used in the final cut analysis.

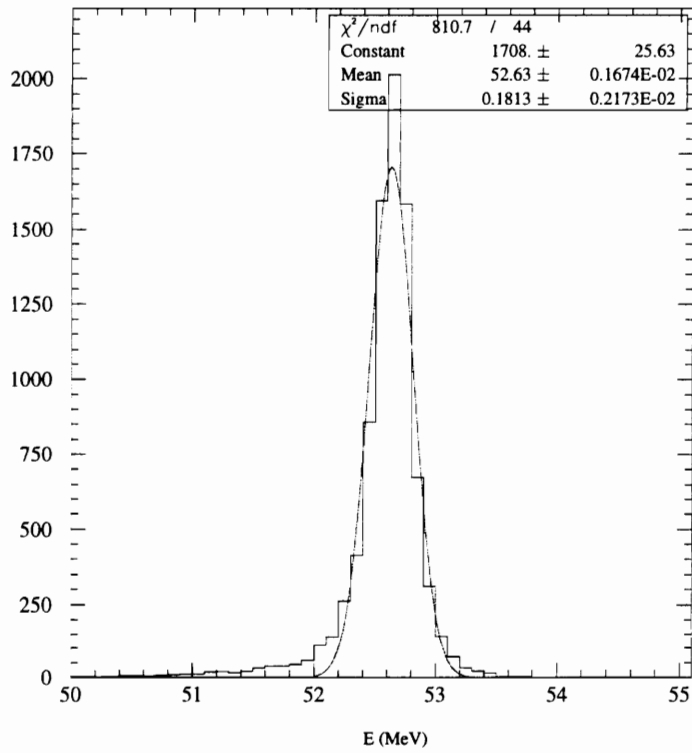


Figure 73: The simulated 52.8 MeV positron energy spectrum

5.2.1 The Positron Energy Cut

Fig. 73 shows the plot of the reconstructed energy for an isotropic distribution of simulated 52.8 MeV positrons. The most probable energy loss in the target and MWPCs is 170 keV. The “Landau tail” of the ionization energy loss distribution as well as bremsstrahlung give rise to the long tail on the low energy side of Fig. 73. Multiple scattering and ERC’s reconstruction resolution smears the distribution to low and high energies.

We compare the standard deviation σ of this spectrum to the “width” Δ near the endpoint of a simulated Michel decay spectrum to determine how to convert the Michel endpoint width to the standard deviation of the measured response to monoenergetic 52.8 MeV positron. The ratio σ/Δ for six categories of reconstructed tracks are shown in the last column of Table 31. Although there is a large scatter among these ratios, they are fairly consistent with each other within their errors. We used their weighted average $\langle\sigma/\Delta\rangle = 0.67\pm 0.05$ to scale the measured width at the endpoint of the Michel decay spectrum (again, for each track category) as shown earlier in Table 23 to the standard deviation for monoenergetic 52.8 MeV positron (see Table 32). Note that this scale factor is similar in motivation and value to the one used to convert from the pion-decay photon energy spread to the resolution for 52.8 MeV photons, as discussed in Chapter 4.

The effective standard deviation, weighted by the expected fraction of each category of tracks, is given by

$$\sigma = \sum_{\ell,k} f_{\ell k} \cdot \sigma_{\ell k} \quad (121)$$

where ℓ runs over the track loop number and k is the index for upstream and downstream.

A cut window from 51.6 MeV to 53.6 MeV was chosen for the positron energy, to enhance the fraction of signal events in this window while rejecting as much background as possible. The effective cut efficiency was 88.5% for 52.8 MeV.

Table 31: Energy resolutions of simulated positrons

	Loop Number	Michel decay endpoint		52.8 positron		σ/Δ
		Centroid (MeV)	Δ (MeV)	Centroid (MeV)	σ (MeV)	
Up-stream	0	52.69±0.04	0.41±0.04	52.72±0.01	0.23±0.01	0.57±0.09
	1	52.61±0.05	0.18±0.05	52.64±0.01	0.12±0.01	0.69±0.09
	2+	52.41±0.05	0.21±0.05	52.53±0.01	0.15±0.01	0.72±0.11
Down-stream	0	52.07±0.13	0.41±0.04	52.76±0.02	0.21±0.02	0.52±0.26
	1	52.55±0.06	0.25±0.06	52.63±0.01	0.15±0.01	0.58±0.12
	2+	52.42±0.08	0.27±0.07	52.52±0.01	0.25±0.01	0.92±0.14

Table 32: Calculated energy resolution for real 52.8 MeV positrons

	Loop number	Fraction of all events	Michel e^+ Δ (MeV)	52.8 MeV e^+ σ (MeV)	$f \cdot \sigma$
Up-stream	0	0.282	0.621	0.410	0.117
	1	0.284	0.237	0.156	0.045
	2+	0.131	0.289	0.191	0.025 0.187
Down-stream	0	0.189	0.819	0.541	0.103
	1	0.163	0.337	0.222	0.037
	2+	0.121	0.333	0.220	0.027 0.167
Effective Standard Deviation(MeV):					0.354
FWHM(MeV):					0.833

5.2.2 Photon Energy Cut

The simulated 52.8 MeV photon energy spectrum for conversions in either the inner or outer lead sheet of a given photon spectrometer are shown in Fig. 74. Conversions in the inner lead sheet have a broader energy spectrum because of the additional multiple scattering, energy loss straggling and bremsstrahlung of the e^+e^- pair when passing through the outer lead sheet. An asymmetric 2σ window from 50.3 MeV to 54.3 MeV is imposed on the outer-conversions energy spectrum, so the cut efficiency is about 71%. The cut window for the inner conversion energy spectrum extends from 49.3 MeV to 55.3 MeV, for which the signal efficiency is about 66%. These energy acceptance regions are shown as the cross-hatched region of in Fig. 74.

5.2.3 $e\gamma$ Opening Angle Cut

The $e\gamma$ opening angle cut takes advantage of the back-to-back directions of e and γ from $\mu \rightarrow e\gamma$ at rest. The reconstructed photon direction from the photon spectrometer information alone can not be used for the opening angle cut because of the poor angular resolution. Instead, the photon direction is calculated from the line joining the reconstructed photon conversion point $(x_\gamma, y_\gamma, z_\gamma)$ and the reconstructed muon decay point (x_o, y_o, z_o) obtained from the positron helix traceback. The direction cosines of the photon direction are given by:

$$n_{\gamma x} = \frac{x_\gamma - x_o}{r} \quad (122)$$

$$n_{\gamma y} = \frac{y_\gamma - y_o}{r} \quad (123)$$

$$n_{\gamma z} = \frac{z_\gamma - z_o}{r} \quad (124)$$

where

$$r = \sqrt{(x_\gamma - x_o)^2 + (y_\gamma - y_o)^2 + (z_\gamma - z_o)^2} \quad (125)$$

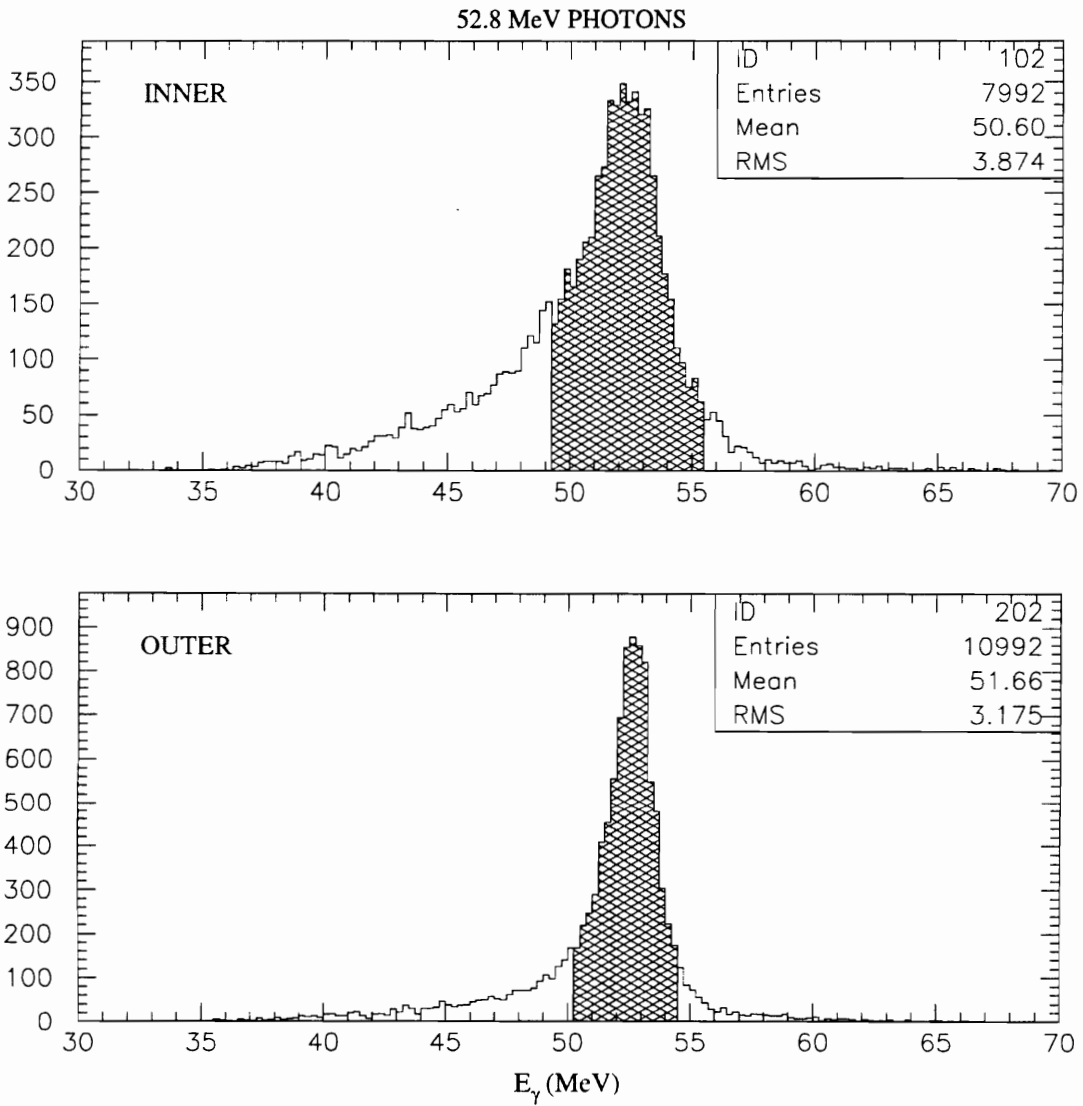


Figure 74: Reconstructed energy for 52.8 MeV photons. The shaded area represents the acceptance window.

is the distance from the muon decay point to the photon conversion point. The positron's direction cosines (n_{ex}, n_{ey}, n_{ez}) can be computed from the equations (92)-(94) of Chapter 4 with the substitution of x_o and y_o for x_c and y_c , respectively. The opening angle $\Theta_{e\gamma}$ is defined by:

$$\Theta_{e\gamma} = \cos^{-1}(\hat{n}_e \cdot \hat{n}_\gamma) \quad (126)$$

Since the positron initial direction resolution—and therefore the $\Theta_{e\gamma}$ resolution—is degraded for tracks moving nearly tangent to the target plane (i.e., with $\eta \simeq 90^\circ$), we discard such “skipping” tracks with a two dimensional cut on $\Theta_{e\gamma}$ vs η . The scatterplot at the top of Fig. 75 shows the $\Theta_{e\gamma}$ vs η distribution; all points below the curve are discarded. The efficiency of this cut for $\mu \rightarrow e\gamma$ events is 84.6%.

5.2.4 Relative $e\gamma$ Timing Cut

As described in chapter 4, the $e\gamma$ relative time $\Delta t_{e\gamma}$ should have a central value of 0 ns for a true $\mu \rightarrow e\gamma$ event after accounting for the flight path delays of the positron and photon, the first half-loop delay of the photon's e^+e^- pair, and the light propagation delay along the positron scintillator:

$$\Delta t_{e\gamma} = (t_e - t_e^o - \frac{L_e}{c} - \frac{z_e}{v_e}) - (t_\gamma - t_\gamma^o - \frac{L_\gamma}{c}) \quad (127)$$

The raw measured times are t_e and t_γ ; the calibrated equal-time offsets are t_e^o and t_γ^o ; and the remaining terms are the flight delays for the events. (For historical reasons, the photon's e^+e^- pair's half-loop-flight delays are incorporated into t_γ by the PAIRS reconstruction.)

From the analysis of Ring Counter events in the MEGA production data, we found that the centroid of $\Delta t_{e\gamma}$ was systematically shifted up by 0.7ns. For conservatism, the centroid of timing window was set at 0.5 ns and the window width at ± 2 ns, which retained 95.7% of the candidate events.

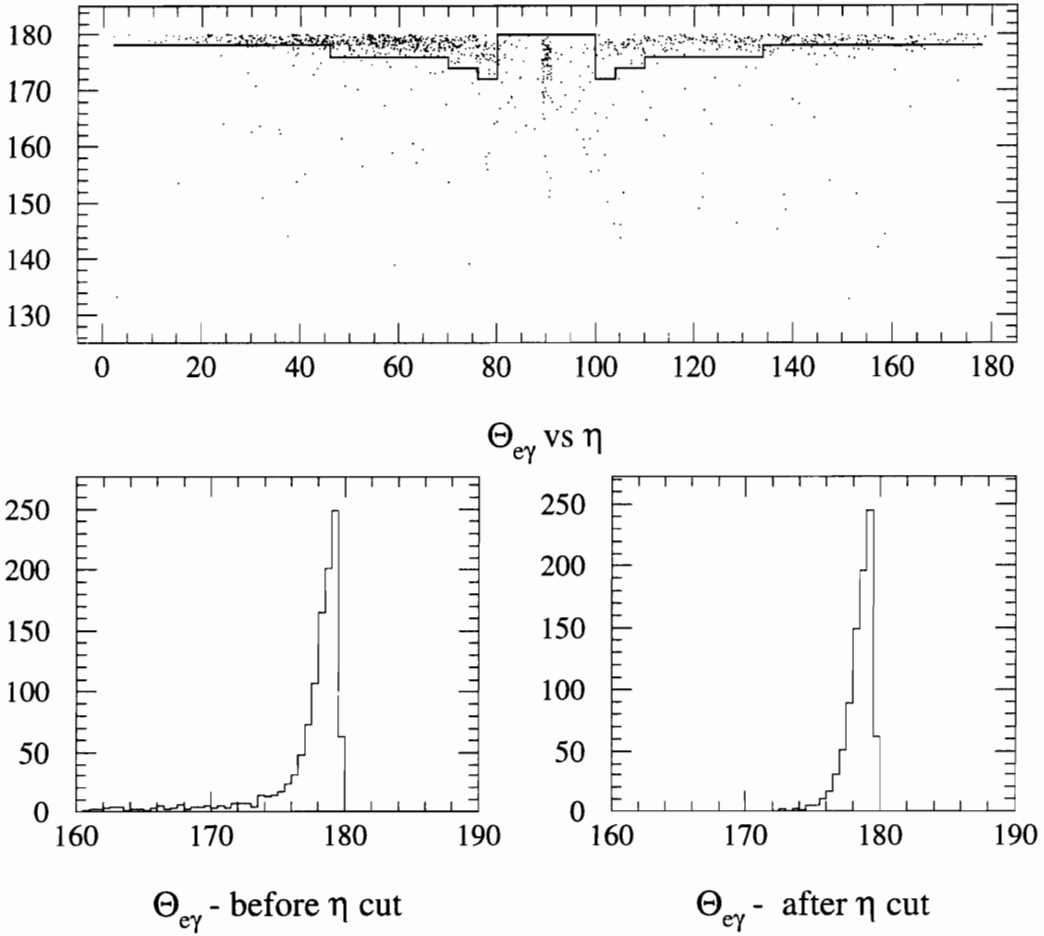


Figure 75: The distribution of positron-photon opening angle vs positron-target tangency angle for simulated $\mu \rightarrow e\gamma$ events (top), showing the two-dimensional cut; $\Theta_{e\gamma}$ distributions before and after imposition of this 2D cut (bottom).

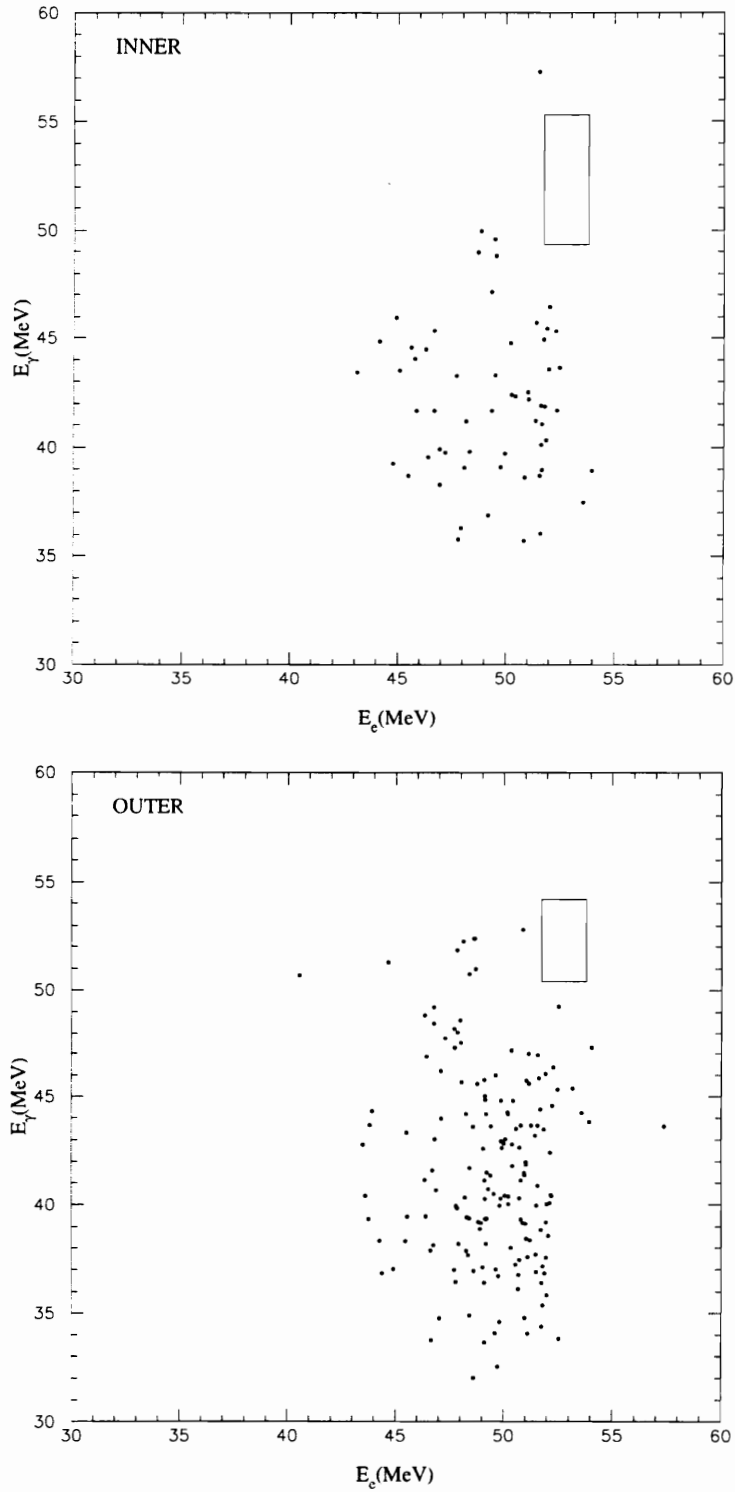


Figure 76: 1992 $\mu \rightarrow e\gamma$ signal search. Inner (top) and outer (bottom) lead conversion layers for the photon.

Table 33: Summary of cuts for the $\mu \rightarrow e\gamma$ search

Quantity	Limits	Efficiency
E_e	51.6 \rightarrow 53.6 MeV	0.88
E_γ (Outer)	50.3 \rightarrow 54.3 MeV	0.73
E_γ (Inner)	49.3 \rightarrow 55.3 MeV	0.66
$\Delta t_{e\gamma}$	-1.5 \rightarrow 2.5 ns	0.95
$\Delta\Theta_{e\gamma}$	$\Theta_{e\gamma}^{min}(\eta) \rightarrow 180^\circ$	0.85
		0.51

5.2.5 $\mu \rightarrow e\gamma$ Search

The cuts imposed with PAW on the data from Filter 3 for the $\mu \rightarrow e\gamma$ search and their efficiencies for $\mu \rightarrow e\gamma$ events are summarized in Table 33. The net efficiency for these cuts was 50.5%. After applying the timing and opening angle cuts, the remaining candidate events were classified according to whether the reconstructed photon converted to an e^+e^- -pair in the inner or outer lead sheet of its identifying pair spectrometer. The scatterplots of E_γ and E_e for these two classes are shown in Fig. 76, along with the cuts on E_γ and E_e . No candidate events were found within our acceptance limits—the search yielded a null result.

5.3 Normalization

Before converting this null result into an upper limit on the $\mu \rightarrow e\gamma$ branching rate, the number of useful muon decays must be evaluated for the 1992 data. This is given

by

$$N_\mu = N_{stop} \times f_{live} \times \frac{\Omega_{e\gamma}}{4\pi} \times \eta_{ip} \times \eta_{trig} \times \eta_\gamma \times \eta_e \times \eta_{cut} \times \eta_{on} \quad (128)$$

In the following paragraphs, we discuss each of these terms in more detail.

The raw number of muons stopped on the central target, N_{stop} , was determined from a scaler that integrated the (trigger-independent) hits in four upstream electron scintillators during the course of each run. These scintillators sampled the positrons from $\mu \rightarrow e\nu\bar{\nu}$ decays for muons that stopped in the central target, while being shadowed from the Michel decay positrons produced elsewhere, e.g., at the downstream vacuum window. A Monte Carlo simulation was used to determine the scale factor of 288 by which we multiplied this scaler count to arrive at the number of raw muon decays. In 1992, we had 266 physics runs, for which the total number of muon stopped on the target was 2.35×10^{12} .

The live time fraction, f_{live} , was calculated from the ratio of two scaler outputs—GHIGH*READY, which counted the number of GHIGH triggers that appeared when the data acquisition system was READY to accept another events, and GHIGH_UNGATED, which counted all of the GHIGH triggers. These scaler outputs were recorded for each run. The live time fraction averaged over the entire 1992 data sample was 80%.

The overlap solid angle between photon and positron, $\Omega_{e\gamma}$, was calculated by analyzing 78K Monte Carlo $\mu \rightarrow e\gamma$ events that were thrown into 4π steradians. We included the loss of acceptance due to missing (parts of) chambers in this term. By convention, an event was defined to be within the experiment's acceptance if the positron had at least one dwarf hit, one scintillator hit, and a Snow White hit ($\Omega_e = 0.43 \times 4\pi$, including a 26% reduction due to the missing positron spectrometer channels), and if the photon was within the fully instrumented portions of the photon pair spectrometer ($\Omega_{e\gamma} = 0.91 \times \Omega_e = 0.39$, including a 9% reduction due to the uninstrumented delay lines in layer 2).

The probability of a 52.8 MeV photon interacting with a pair spectrometer η_{ip} is computed from the Monte Carlo simulation. The analysis indicates this probability for the two pair spectrometer layers available in 1992 was about 0.189. Of these

interactions, 86.7% were pair production and the remainder were hard Compton scattering.

If the 52.8 MeV photon produced an e^+e^- pair, the probability that this pair would pass the first level high energy hardware trigger (GHIGH), was estimated by a trigger simulation to be 0.572; an additional 16.1% of these pairs were rejected by the second level trigger. The overall trigger efficiency for both trigger stages was 0.479.

The PAIRS reconstruction efficiency for 52.8 MeV photons, η_γ , was estimated by the fraction of a sample of simulated photons passing the χ^2 cut and vertex cut, 0.211, divided by the fraction of the same sample passing the hardware trigger, 0.428, both in fully instrumented photon spectrometers. This ideal efficiency was 0.482. When the effects of spectrometer inefficiencies and missing readout channels were included, this dropped to 0.405.

The positron reconstruction efficiency, η_e , is the product of the ERC reconstruction efficiency for simulated low-rate 52.8 MeV positrons in a fully operational positron spectrometer ($\eta_e^L = 0.91$) and the probability that the reconstructed tracks, when overlapped with background events from the 1992 data set, satisfy the high rate filter quality cut on χ^2 ($\eta_e^H = 0.49$). The net efficiency of positron reconstruction efficiency, η_e , is then computed to be 0.45. Note that η_e^H includes a factor of 0.77 for the probability that the track satisfies the ARC package's requirements in Filter 1. The inefficiency here is dominated by the loss of the Snow White triple crossing near the struck positron scintillator due to the average anode and cathode efficiencies of 0.90 and 0.86, respectively. This Filter 1 efficiency of 0.77 was previously reported as 0.59 in Dzemedzic's thesis[49] because it mistakenly counted the loss of acceptance due to dead wires and chambers; but this 24% acceptance loss is already tallied in the detector acceptance $\Omega_{e\gamma}$.

The cut efficiency, $\eta_{cut} = 0.51$, is the product of the cut efficiencies of the four kinematic variables from Table 33.

The on-line filter efficiency, η_{on} , includes two terms: the effect of the software second stage trigger veto and the discarding of photons by the online PAIRS filter that would have passed the offline PAIRS filter. For 1992 data, this term was estimated to be 85%.

Table 34: The summary of the number of useful stopped muons in 1992

Quantity	Value	Definition
$N_{stop} \times f_{live}$	1.88×10^{12}	Number of stop muon processed
$\Omega_{e\gamma}$	0.39	Overlap solid angle
η_{ip}	0.19	Prob. of photon interaction
η_{trig}	0.48	Trigger efficiency
η_{γ}	0.41	Photon recon. efficiency
η_e	0.45	Positron recon. efficiency
η_{cut}	0.51	Cut efficiency
η_{on}	0.85	On line filter efficiency
N_{μ}	5.35×10^9	Number of useful stop muon

Table 34 summarizes all of terms in the equation (128). Taking their product, the number of useful stopped muon was 5.35×10^9 .

5.4 Branching Ratio

For our null result, the 90% confidence level upper limit is estimated using 2.3 candidate events[55]. To account for the uncertainty in the denominator N_{μ} , we use a numerator of 2.6 instead of 2.3 to get the upper limit on the $\mu \rightarrow e\gamma$ branching ratio of

$$\frac{\Gamma(\mu^+ \rightarrow e^+\gamma)}{\Gamma(\mu^+ \rightarrow e^+\nu_e\bar{\nu}_{\mu})} < \frac{2.6}{N_{\mu}} = 4.9 \times 10^{-10} \text{ (90\% C.L.)} \quad (129)$$

This result is one order of magnitude worse than the Crystal Box upper limit.

Table 35 compares the design parameters and the values we achieved from the analysis of the 1992 data. The factor of 1.36 loss of acceptance was caused by the

Table 35: Summary of the solid angle and the efficiency comparison between analysis and design

Quantity	Design	1992 analysis	Degradation
$\Omega_{e\gamma}$	0.51	0.39	1.36
$\eta_{ip} \times \eta_{trig}$	0.09	0.09	1.00
η_{γ}	0.60	0.41	1.46
η_e	0.95	0.45	2.11
η_{cut}	0.40	0.51	0.78
η_{on}	1.00	0.85	1.18
			—
			3.86

loss of Dwarf seven, the downstream cathodes of Dwarf 3, half the anodes of Dwarf 5, and several other missing channels. The cut efficiency was better than expected primarily because the photon cuts on energy and opening angle were loosened. The estimates of the reconstruction efficiency for both photons and positrons appear to have been too optimistic in the design.

Even if we had achieved all of the design efficiencies and acceptance goals, we would have obtained only four times more useful muon stops from the 1992 data—giving a branching ratio upper limit a factor of 2.5 worse than the Crystal Box limit.

Finally, we must take into account the experiment's actual sensitivity to a $\mu \rightarrow e\gamma$ signal. Recall from the end of Chapter 4 that a search for the allowed process $\mu \rightarrow e\nu\bar{\nu}$ (with energetic positron and photon) in the MEGA data turned up no more than 4.8% of the expected number of such events. We concluded there that a global loss in sensitivity had resulted from the unfortunate adjustment in the gate width of the positron spectrometer's MWPC latches without a corresponding retuning of the gate offset. This sensitivity loss is not accounted for in any of the preceding analysis of the $\mu \rightarrow e\gamma$ branching ratio sensitivity. If we factor it in, the upper limit on the $\mu \rightarrow e\gamma$

branching ratio from the 1992 data could have been no better than

$$B.R.(\mu \rightarrow e\gamma) < \frac{2.6}{0.048 \cdot N_\mu} = 1.0 \times 10^{-8} \text{ (90\% C.L.)} \quad (130)$$

Importantly, the deficiencies identified in the 1992 run were corrected for the MEGA production runs of 1993 and beyond: the acceptance was improved by adding the third layer of photon spectrometer and by repairing the problems in the positron spectrometer MWPCs; both stages of hardware trigger were installed; eight more powerful workstations were used in the online farm; the online event filtering code, having performed robustly in the offline Filter 1 analysis in 1992, was set to cut harder on the triggered data so that a “pure” $\mu \rightarrow e\gamma$ candidate events sample was written to tape; the peak muon stop rate was roughly doubled from 135 MHz to 250 MHz (instantaneous); and the positron spectrometer latch gates were widened and positioned to ensure that the experiment would be sensitive to a $\mu \rightarrow e\gamma$ signal. The total number of muon stops taken in 1993–1995 is about $2. \times 10^{14}$ (including November 1995 running), which should give a $\mu \rightarrow e\gamma$ branching ratio sensitivity of 7×10^{-13} (90% C.L.).

Bibliography

- [1] C. Bouchiat and L. Michel, Phys.Rev. **106**, 170 (1957).
- [2] Crittenden et al., Phys. Rev. **121**, 1823 (1961).
- [3] Bertl et al., Phys. Lett. **140B**, 299 (1984).
- [4] R.D. Bolton et al., Phys Rev. Lett. **56**, 2461 (1986).
- [5] Bellgardt et al., Nucl. Phys. **D299**, 1 (1988).
- [6] A. Lagarrigue and C. Peyron et al., C. R. Acad. Sci. **234**, 1873 (1952).
- [7] G. Danby et al., Phys. Rev. Lett. **9**, 36 (1962).
- [8] W. Sullivan, New York Times, page A24, (Feb 9, 1977).
- [9] H.P. Povel, Phys. Lett. **B72**, 183 (1977).
- [10] J.D. Bowman et al., Phys. Rev. Lett. **45**, 556 (1979).
- [11] R.D. Bolton et al., Phys Rev. Lett. **53**, 1415 (1984).
- [12] S. Ahmad et al., Phy. Rev. **D38**, 2102 (1988).
- [13] Dohman et al., Phy. Lett. **B317**, 361 (1993). An even better limit for $\mu^+ \rightarrow e^+$ conversion of 7.3×10^{-13} has been reported in the PSI (formerly SIN) Annual Report, CH-5232 (February 1995), p. 16.
- [14] M.D. Cooper et al., MEGA: Search for the Rare Decay $\mu^+ \rightarrow e^+\gamma$. LAMPF Proposal No. 969, (1985).

- [15] Ernest S. Abers and Benjamin W. Lee, Phys. Rept, **C9**, 1 (1973).
- [16] V.D. Barger and R.J.N. Phillips, Collider Physics, Addison-Wesley (1987).
- [17] Weihermer et al, Phys. Lett. **B300**, 210 (1993).
- [18] R. Abela et al, Phys. Lett., **146B**,431, (1984)
- [19] H. Albrecht et al, Phys. Lett., **202B**, 149, (1988).
- [20] A.M. Cnops et al, Phys. Rev. Lett., **40**, 144, (1978).
- [21] T.P. Cheng and Ling-fong Li, Phys. Rev. Lett., **38**, 381, (1977).
- [22] P. Herczeg et al, Phys. Rev., **D34**, 3449 (1986).
- [23] M.A.B. Beg and R.V. Bundy, Phys. Rev. Lett., **38**, 1252 (1977).
- [24] H. Georgi and S. Glashow, Phys. Rev. Lett. **32**, 438 (1974).
- [25] B.A. Campbell, Phys. Rev., **D28**, 209 (1983).
- [26] M.J.S. Levine, private communication.
- [27] L.F. Lee, Gauge Theory of Elementary Particle Physics, Page 420, Oxford Univ. Press 1984.
- [28] R.D. Bolton et al, Phys. Rev. Lett., **53**, 1418 (1984).
- [29] R.D. Bolton et al, Nucl. Instrum. Methods, **A241**, 52 (1985).
- [30] IEEE Standard FASTBUS Modular High-speed Data Acquisition and Control System. IEEE, New York (1985).
- [31] Phillips Scientific, 305 Island Road, Mahwah, NJ 07430, USA.
- [32] Particle Data Group Review of Particle Properties, Phys. Rev. **D3**, 1173 (1994).
- [33] see §17.5.4 of Particle Data Group, Review of Particle Properties, Phys. Rev. **D3**, 1173 (1994).

- [34] GEANT, Detector Description and Simulation Tool, Application Software Group Computing and Networks Division, CERN, Geneva (1992).
- [35] D. Aston et al, The LASS Spectrometer. Technical Report 0298, SLAC (1987).
- [36] Bicron Corporation, 12345 Kinsman Road, Newbury, OH 44065 USA.
- [37] Hamamatsu Coporation, 2444 Moorpark Ave. Suite 312, San Jose, CA 95128 USA.
- [38] V. Armijo et al, Nucl. Instrum. Methods, A303, 298 (1991).
- [39] Creative Electronics System S.A., Case Postale 122, 1213 Petit Lancy, Geneva, Switzerland.
- [40] Motorola Semiconductor Products Inc., P.O.Box 20912, Phoenix AZ 85036 USA.
- [41] Digital Equipment Corporation, 146 Main Street, Maryland, MA 01754, USA.
- [42] LAMPF Q Data Acquisition System.
- [43] Template Graphics Software, Inc., San Diego, CA, 92121, USA
- [44] Gary Hogan, Electron Reconstruction Program, Documentation for ERC.
- [45] Leo. E. Piilonen, MEGASIM, Documentation for MEGASIM.
- [46] W.R. Nelson and Hideo Hirayama, SLAC-Report-265 (1985).
- [47] R.E. Mischke and R.A. Williams, Energy Loss and Multipls Scattering Algorithms for Monte Carlo Application. Technical Report 82-1952, Los Alamos National Laboratory, (1982).
- [48] Leo van Ausdeln, A Photon Detector System for the Search for the Rare Muon Decay $\mu \rightarrow e\gamma$, Ph.D thesis of Texas A&M University (1993); Los Alamos National Laboratory Report LA-12635-T (1993).
- [49] Mario Dzmidzic, MEGA - A Search for Lepton Number Violation in the Decay $\mu \rightarrow e\gamma$, Ph.D thesis of Houston University (1995).

- [50] M.D. Cooper, R.E. Mischke and L.E. Pillonen et al, A proposal to measure the Michel parameter ρ with MEGA positron spectrometer. LAMPF Proposal No. 1240 (1991).
- [51] Fan Liu, Measurement of the Michel Parameter ρ with the MEGA Positron Spectrometer, Ph.D thesis of Texas A&M University (1994).
- [52] PAW, Physics Analysis Workstation, Version 2.03, CERN, Geneva (1993).
- [53] MINUIT, Function Minimization and Error Analysis, Version 92.1, CERN, Geneva (1992).
- [54] COMIS, Compilation and Interpretation System, Version 2, CERN, Geneva (1993).
- [55] W.R. Leo, Techniques for Nuclear and Particle Physics Experiment, Springer-Verlag.
- [56] Charles Jui, Test Results from the MEGA Experiment: A search for the Rare Decay of the Muon to an Electron and Gamma Ray, Los Alamos Report LA-12324-T (1992).

CURRICULUM VITAE

Yiding Zhang

Department of Physics

Virginia Polytechnic Institute and State University
Blacksburg, VA 24061

Date of birth: December 19, 1956
Citizenship: China (US Permanent Resident)
Telephone: Office - (540)231-5417
FAX - (540)231-7511
E-mail: yiding@amy.phys.vt.edu

Leo Nilonen
for
Y.Z.
(thesis advisor)

SUMMARY

Over 5 years working experience on an experiment (MEGA) at LAMPF, from MWPC construction, electronics test and debugging, detector set up, data taking and analyzing, to final results.

EDUCATION

Ph.D., Physics, Virginia Polytechnic Institute and State University
Dissertation of Ph.D.: "Search for the Rare Decay of the Muon into a Positron and a Photon"

M.S., Physics, 1985, Institute of High Physics, Academia Sinica, China
Dissertation of M.S.: "The Symmetric Structure of Excited States of $^{13}_{\Lambda}C$ and Investigation of Angular Distribution of $^{13}C(K^-; \pi^-)^{13}_{\Lambda}C$ "

B.S., Physics, 1982, Hangzhou University, Zhejiang, China
Dissertation of B.S.: "Multi-Channel Analysis of Sonic Frequency"

SKILLS

Hardware:

- MWPC construction and associated gas system.
- Chamber electronics testing, setup and debugging (preamplifiers, discriminator and FASTBUS).
- Scintillators and associate electronics setup.
- Various online testing and analysis.

Software:

- Familiar with various computer platforms (UNIX, VAX, PC).
- Techniques for data analysis (including use of PAW and other CERN packages), and programming in FORTRAN, C and C++).
- Particle Physics Monte Carlo simulations (EGS4, GEANT).

System Manager:

- VAX(VMS)

PUBLICATIONS

The Symmetric Structure of Excited States of $^{13}_{\Lambda}C$ and Investigation of Angular Distribution of $^{13}C(K^-; \pi^-)^{13}_{\Lambda}C$. *Comm. Theo. Phys.* 10(1988) 425-426.

Current Results for $\mu \rightarrow e\gamma$ decay search with MEGA experiment,
Y. Zhang *et al.*, Joint Meeting of The APS and AAPT, Washington DC, April 1993.

A search for $\mu \rightarrow e\gamma$ at level of 10^{-13} , R.E. Mischke *et al.*, submitted to 27th International Conference on High Energy Physics, Glasgow, Scotland, July 1994.

A Measurement of Michel Parameter ρ in Muon decay, R.E. Mischke *et al.*, submitted to 27th International Conference on High Energy Physics, Glasgow, Scotland, July 1994.